IRM de diffusion du Q-space : Acquisition et pré-traitements

Emmanuel Caruyer

PhD THESIS

prepared at
Inria Sophia Antipolis - Méditerranée

and presented at the
University of Nice-Sophia Antipolis
Graduate School of Information and Communication Sciences

A dissertation submitted in partial fulfillment
of the requirements for the degree of

DOCTOR OF SCIENCE
Specialized in Control, Signal and Image Processing

Q-space Diffusion MRI: Acquisition and Signal Processing

Emmanuel CARUYER

Advisor	Dr. Rachid Deriche	Inria Sophia Antipolis - Méditerranée, France
Reviewers	Pr. Nikos Paragios	École Centrale de Paris, France
	Pr. Jean-Philippe Thiran	École Polytechnique Fédérale de Lausanne, Switzerland
Examiners	Pr Daniel Alexander	University College London, UK
	Dr Habib Benali	Université Pierre et Marie Curie, Paris, France
	Pr Jean-Philippe Ranjeva	Faculté de Médecine, Marseille, France

UNIVERSITÉ NICE-SOPHIA ANTIPOLIS - UFR Sciences

École Doctorale STIC
(Sciences et Technologies de l'Information et de la Communication)

THÈSE

pour obtenir le titre de

DOCTEUR EN SCIENCES

de l'UNIVERSITÉ de Nice-Sophia Antipolis

Discipline: Automatique, Traitement du Signal et des Images

présentée et soutenue par

Emmanuel CARUYER

IRM de Diffusion du Q-space : Acquisition et pré-traitements.

Thèse dirigée par Rachid DERICHE

Sountenue le Mercredi 18 Juillet 2012

Composition du jury:

Rapporteurs	Pr. Nikos Paragios	École Centrale de Paris, France
	Pr. Jean-Philippe Thiran	École Polytechnique Fédérale de Lausanne Suisse
Examinateurs	Pr Daniel Alexander	University College London, UK
	Dr Habib Benali	Université Pierre et Marie Curie, Paris, France
	Pr Jean-Philippe Ranjeva	Faculté de Médecine, Marseille, France

Abstract

The overall goal of this thesis is to develop novel methods for the acquisition and the processing of diffusion magnetic resonance images (MRI), to provide new insights into the structure and anatomy of the brain white matter *in vivo*. Diffusion MRI is a non-invasive technique that measures locally the diffusion of water molecules. The latter are hindered by tissue structure, and therefore the characterization of water molecules displacement gives information on the nature, orientation, microstructure of the underlying tissue. Because of the strong anisotropy observed in white matter fiber tracts, this tool is most popular for the analysis of brain connectivity. One of the modality of acquisition and reconstruction, called diffusion tensor imaging, is now an established tool in research and clinical applications, for the detection of neural diseases and for pre-operative planning. Being model-based, the diffusion tensor cannot describe complex intra-voxel configurations, with multiple populations of fibers crossing. Since then, for a finer description of water molecules displacement, model-free approaches have recently been proposed, aiming at overcome the limitations of the diffusion tensor. Most of these techniques are still extremely demanding in acquisition time, and involve challenging reconstruction problems.

The first part of this thesis proceeds from a description of the tissue microstructure, and a physical explanation of the origin of acquired diffusion signal. We give a review of the reconstruction methods and corresponding acquisition techniques in diffusion MRI. Several reconstruction methods are presented, and are categorized into model-based and model-free techniques. The first contribution of this thesis is related to the parametric reconstruction of the diffusion signal in a continuous basis of functions. We develop on a previous proposed method called Spherical Polar Fourier basis, and propose a continuous basis with a significant reduction of the dimension for the same power of description. We also derive the expression of the Laplace regularization operator in this basis, for a better robustness to noise. The second contribution is also related to the reconstruction of the diffusion signal, and the orientation distribution function, with a special focus on clinical setting. We propose a real-time reconstruction algorithm based on the Kalman filter to reconstruct the ODF in constant solid angle. We develop on top of the Kalman filter a motion detection algorithm, based on a monitoring and statistical analysis of the Kalman filter residuals. We are able to give a precise and sensitive motion detection, at no additional cost on the on-line acquisition system, as compared to systems based on camera and computer vision. The two last contributions are related to the acquisition methods in diffusion MRI, in particular for single and multiple q-shell experiments. We first describe a geometric approach to generate angular uniform

schemes, that offer optimal angular coverage per shell and as a whole. Then we investigate on the link between the choice of a parametric basis of functions, and the design of sampling protocols. We give explicit methods to generate sampling schemes with minimal condition number, for the reconstruction in spherical harmonics (in q-ball imaging) and the reconstruction in the modified spherical polar Fourier basis, proposed in this thesis. The conclusion of this approach is that the sampling method should be driven by the physical constraints of the scanner, and at the same time by the choice of a specific basis to represent the diffusion signal, and with an overall uniform coverage of the space of sampling directions, for a good rotational invariance. The new sampling schemes generated with this technique are available for download from my web page.

Keywords diffusion MRI; acquisition sequence; q-space sampling; q-ball imaging; regularized reconstruction; Laplace regularization; Kalman filtering; motion detection.

Résumé (en français)

Le but général de cette thèse est de proposer de nouvelles méthodes d'acquisition et de traitement du signal en imagerie par résonance magnétique (IRM) de diffusion, dans le but d'ouvrir de nouvelles perspectives dans la reconstruction de la structure de la matière blanche *in vivo*. L'IRM de diffusion est une technique d'imagerie non invasive qui mesure localement, en chaque voxel, la diffusion des molécules d'eau. Le déplacement de ces dernières étant contraint par la présence de tissus, le fait de pouvoir caractériser la diffusion des molécules d'eau apporte des informations sur la nature, l'orientation, la microstructure des tissus biologiques sous-jacents. La forte anisotropie observée dans la matière blanche fait de l'IRM de diffusion un outil privilégié pour l'étude de la connectivité cérébrale. Une des premières techniques d'acquisition et de reconstruction, appelée IRM du tenseur de diffusion, est maintenant utilisée de manière routinière en clinique, pour le diagnostique de certaines maladies neurologiques, ou encore en planification préopératoire. L'IRM du tenseur de diffusion repose sur un modèle de diffusion gaussien cependant, qui est limité quand il s'agit de décrire des configurations de tissus complexes à l'intérieur d'un voxel, par exemple quand plusieurs faisceaux de fibres se croisent. Dès lors, on a cherché ces dernières années à développer des techniques qui ne reposent pas sur un modèle a priori, afin de décrire de manière plus précise le déplacement des molécules d'eau, et dépasser les limitations du modèle tensoriel. La plupart de ces techniques, dites à haute résolution angulaire, sollicitent un temps d'acquisition généralement long, et mettent en jeu des problèmes de reconstruction non triviaux.

Dans la première partie de cette thèse, nous décrivons la structure microscopique des tissus de la matière blanche du cerveau, et présentons la physique de formation des images en IRM de diffusion. Nous faisons un état de l'art des méthodes de reconstruction, et des techniques d'acquisition proposées à ce jour. En ce qui concerne les méthodes de reconstruction, nous faisons la distinction suivant qu'elles soient basées sur un modèle ou non. La première contribution de cette thèse est liée à la reconstruction paramétrique du signal de diffusion dans une base de fonctions continues. Cette contribution fait suite à une méthode proposée récemment, appelée transformée de Fourier sphérique, et y apporte une modification pour une reconstruction continue. Nous réduisons de façon significative la dimension de la base, tout en décrivant aussi bien le signal de diffusion. Nous donnons également l'expression de l'opérateur de régularisation de Laplace en fonction des coefficients dans cette base, afin de limiter l'impact du bruit sur la reconstruction. La seconde contribution est également liée à la reconstruction du signal de diffusion, et à la fonction de distribution d'orientation, dans un contexte d'application clinique. Nous proposons une méthode de reconstruction en temps réel basée sur le filtre de Kalman pour la

probabilité marginale de diffusion angulaire. Nous développons un algorithme pour détecter les mouvements du patient, de façon précise et avec une grande sensibilité, et ce sans surcoût, comparé aux systèmes utilisant une camera et des algorithmes de vision robotique. Les deux dernières contributions présentées dans cette thèse sont liées aux techniques d'acquisition en IRM de diffusion, en particulier pour l'élaboration de schémas d'acquisition sur une ou plusieurs sphères dans l'espace de Fourier. Nous présentons d'abord une méthode géométrique pour placer des points dans l'espace de Fourier sur plusieurs sphères, en optimisant la couverture angulaire sur chacune des sphères, mais également de façon globale. Puis nous cherchons à établir un lien entre le schéma d'acquisition et la base de fonctions utilisée pour la reconstruction, et nous proposons en particulier une méthode pour élaborer un protocole d'acquisition qui permette de minimiser le nombre de conditionnement, pour la reconstruction dans la base des harmoniques sphériques, et dans la base de Fourier sphérique modifiée, proposée dans cette thèse. En conclusion de cette étude sur l'acquisition, nous pensons que l'élaboration du schéma d'échantillonnage doit être motivée à la fois pour répondre aux contraintes physiques du scanner, et par le choix de la base dans laquelle le signal sera reconstruit. Ces nouveaux schémas d'échantillonnage sont disponibles au téléchargement sur mon site internet.

Keywords IRM de diffusion; séquence d'acquisition; échantillonnage dans l'espace de Fourier; acquisition sphérique; reconstruction sous contrainte de régularité; régularisation de Laplace; filtre de Kalman; détection de mouvement.

Contents

Acknowledgements

I would like to express my deepest thanks to Rachid Deriche for his careful and infinitely helpful tutorship during this time I was a PhD candidate. I experienced how the progression in research is a matter of rhythm: *adagio* when developing new ideas, *presto* to meet a conference deadline, *allegro* when preparing a publication for a journal, and Rachid has been an excellent conductor in the Odyssée and then the Athena project-teams, helping me to keep the right tempo at all time. Rachid has shared his experience in research with me, and I would like to thank him for his sympathy, his enthusiasm and his scientific attention throughout my stay at Inria. I would also like to thank Olivier Faugeras for welcoming me in the Odyssée project-team, at the very beginning of PhD thesis. I also want to warmly thank Marie-Cécile Lafont and Claire Senica for their help in finding solutions to administrative puzzles and everyday issues. More generally, I would like to thank all the people at Inria that help in making the working environment ideal for scientific research. I want to acknowledge in particular the Inria associate team program, which partly funded my PhD, in particular the collaboration with our partners at University of Minnesota, through the Computational Diffusion MRI associate team.

I have had the opportunity during my PhD to work with Christophe Lenglet and Guillermo Sapiro, and I am very grateful to them for having welcomed me at the University of Minnesota, Center for Magnetic Resonance Research, and Electrical and Computer Engineering department. This collaboration has been very rich and fruitful, and I really appreciated being involved in this Associate Team program.

I also want to thank Nikos Paragios and Jean-Philippe Thiran for their careful and constructive review and their encouragements. I am also very grateful to Daniel Alexander, Habib Benal and Jean-Philippe Ranjeva who honoured me with their participation in my jury.

Many people supported me during this thesis, and contributed in many different manners to this work. Thanks Alex Gramfort and Demian Wassermann for sharing their passion for the Python programming language, this has really saved me a lot of time in my implementations! Thanks to Iman Aganj, for his irreplaceable proofreading, and for the crazy four hands piano sessions on the Campus at UofM! Thanks Auro for the discussions about linear algebra and higher order tensors, and for the memorable via ferrata and hiking sessions! Thanks Émilien Tlapale for his unlimited knowledge of smart and open-source software solutions, and his interest in almost everything, ranging from photography to stick insects! Thanks Sylvain Merlet for his willingness to create, implement and test novel ideas, and for the good climbing sessions at *Les ressauts, Saint-Jeannet*! Thanks to the deep water solo climbing team: Vivien Robinet, Emmanuel Olivi, Joan Fruitet, Jaime Garcia

Guevara, and to all the members in Odyssée and Athena groups! I would also like to thank Bruno Cessac and Maureen Clerc for the cool jazz sessions at Inria before lunch, and on stage for the *fête des lucioles*.

I have also been weekly supported by my music friends during these three years; I will never forget the Thursday evening sessions with Pascal, Magali, Nico and Nadine, handcrafting together the soul of Penboc'h! I leave the French Rivera with our record packed in my suitcases, and beyond this, I will keep an unforgettable memory of these great moments!

I have been studying for a while now, and I owe an infinite debt to my parents, and my family, who have always supported me all along this way to the PhD thesis.

Finally, I would like to thank my wife, Thanh, for her everyday support and her patience during these three years. Especially for her understanding in the last part of my PhD. I want to dedicate this manuscript to her.

Emmanuel Caruyer.

Part I

Introduction

Chapter 1

Introduction

Diffusion magnetic resonance imaging (diffusion MRI) was proposed in the mid 80's [Le Bihan and Breton, 1985, Merboldt et al., 1985, Taylor and Bushell, 1985], for the early diagnosis of certain neurological disorders. During the last thirty years, diffusion MRI has gained maturity from methodological research contributions and technical advance, and is now an established tool to characterize fine tissue structure, especially useful in the analysis of brain white matter [Johansen-Berg and Behrens, 2009, Jones, 2010b]. At the same time, the quantity of data collected during a diffusion MR acquisition for a fine description of water diffusion, the nature of the signal, render the design of diffusion MR sequence and the reconstruction of diffusion characteristics extremely challenging, to cope with practical limitations in a clinical environment.

Technically, diffusion MRI is based on a physical property of the MR signal to be sensitive to the translational motion of water molecules. More precisely, a pair of pulsed magnetic field gradients applied during the acquisition sequence attenuates the spin echo signal [Stejskal and Tanner, 1965]. By acquiring several attenuated, diffusion images weighted by different gradient orientations and strengths, one has access to a fine characterization of water molecules motion. The rational behind this study of water molecules motion, is that the displacement of particles is constrained by the obstacles in their way. Thus characterizing the diffusion of water molecules give valuable information on the tissue microstructure, at a much finer resolution than conventional MRI.

The diffusion can be described by the probability of water molecules displacement during a given observation time. In a free medium, a glass of water for instance, this probability has an isotropic Gaussian distribution. One of the modality of acquisition and reconstruction in diffusion MRI, called diffusion tensor imaging (DTI) [Basser et al., 1994a,b], is based on an extension to this physical model of diffusion in a free medium. It is indeed a multivariate Gaussian model, and the diffusion tensor is proportional to the covariance matrix of this distribution. DTI is now an established tool in research and clinical applications, for the detection of neural diseases and for pre-operative planning. Describing the anisotropic diffusion by a covariance matrix however, the diffusion tensor model cannot describe complex intra-voxel configurations, with multiple populations of fibers crossing. This has limited the application of fiber tractography, these algorithms that trace the structural connectivity in brain white matter using the information from diffusion MRI.

Since then, for a finer description of water molecules displacement, model-free approaches have been proposed [Tuch et al., 2002, Tuch, 2004a], to overcome the limitations of the diffusion tensor. These high angular resolution diffusion imaging (HARDI) techniques can describe and discriminate several populations of fibers

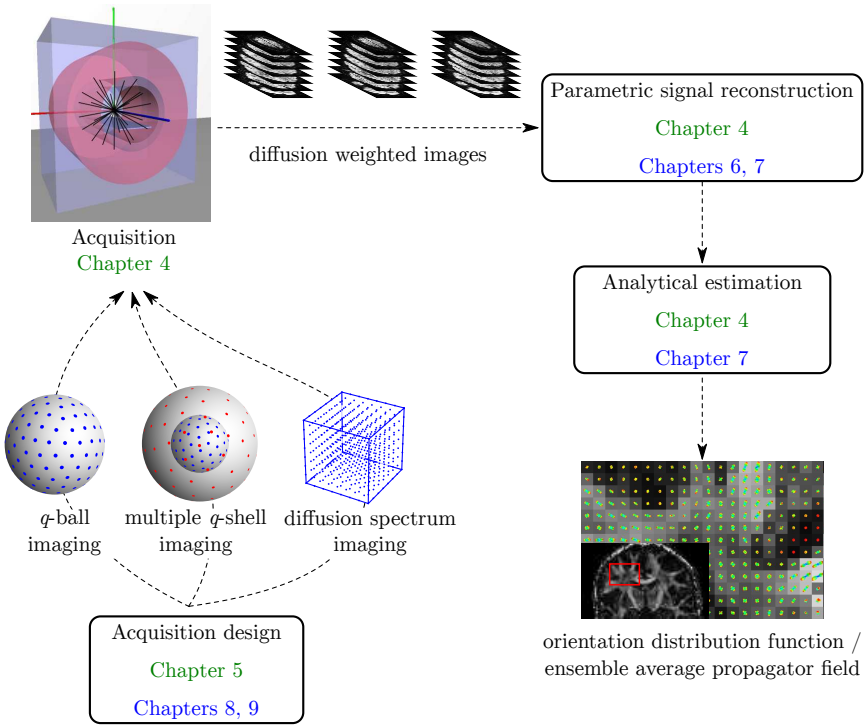

Figure 1.1: The general pipeline in diffusion MRI, from acquisition design to the reconstruction of local diffusion information. The corresponding chapters are indicated; chapters in green present a review or state-of-the-art, while chapters in blue present contributions.

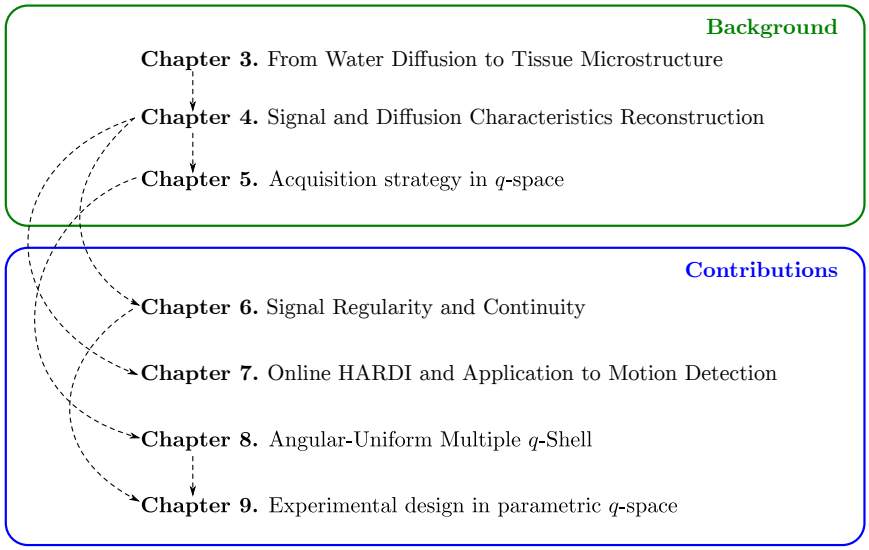

Figure 1.2: Sketch of the chapters in this thesis.

within a voxel, and have provided a great tool to further develop fiber tractography [Fillard et al., 2011]. Nonetheless, HARDI techniques restrict the information gathered from diffusion MRI to the sole angular structure of diffusion. Naturally, some research groups have investigated the interest of reconstructing the complete probability of water molecules displacement, to exploit both radial and angular information [Wedeen et al., 2005, Assaf et al., 2008]. Most of these techniques are still extremely demanding in acquisition time however, and involve complex reconstruction problems. This thesis addresses the challenges in both acquisition and reconstruction raised by these new trends in the diffusion MRI community. We proceed to give the outline of this thesis, providing a brief summary of each chapter. The general pipeline of acquisition and local diffusion model estimation is sketched on Fig. 1.1, on which we refer to the Chapters focusing on on part or another in the pipeline. We give a sketch of the progression to guide the reader through the chapters on Fig. 1.2.

Chapter 3 introduces the main object of study in diffusion MRI. We give a brief description of brain anatomy, with a special focus on brain white matter. Based on an example of restricting geometric that mimics a pack of axonal fibers, we show on a simulation how the motion of water molecules is affected by the impermeable walls of the structure. This introduces the relation between water diffusion and tissue microstructure, at the heart of diffusion MRI motivations in neurology. We also introduce the main mathematical objects to describe the diffusion process, namely the ensemble average propagator (EAP), and the orientation distribution function (ODF).

Chapter 4 presents the physics underlying the formation of diffusion weighted images, and provides a state-of-the-art tour of reconstruction techniques. In particular, the pulse-gradient spin echo (PGSE) sequence is introduced, as well as the related concept of q-space. The reconstruction techniques from the signal to the diffusion characteristics are categorized into model-based techniques, and methods independent of a model. Within the latter family, we present the spherical polar Fourier transform, for which we propose an important modification in Chapter 6.

Chapter 5 presents different approaches to the design of acquisition sequences in q-space, for the reconstruction of the diffusion tensor, the EAP or the ODF. We distinguish acquisitions restricted on a sphere, called q-ball imaging, from other approaches such as Cartesian sampling, called diffusion spectrum imaging, or intermediate sampling on few separate spheres, called multiple q-shell imaging. We show how the different methods on sampling design are either purely geometrical, either purely driven by the needs of a specific reconstruction algorithm.

Chapter 6 describes the first contribution of this thesis, on the parametric estimation of the diffusion signal in q-space. We exhibit a major pitfall in the spherical polar Fourier (SPF) basis originally introduced in Assemlal et al. [2009b], about the continuity of the estimated signal. We show that the space of continuous functions reconstructed in the SPF basis has a substantially reduced dimension, and we give a basis for this subspace. In order to increase robustness to noise, we also derive a Laplace regularization operator, expressed as a quadratic form in the coefficients of the modified SPF basis. This results in a robust and fast parametric reconstruction method of the signal in the q-space.

Chapter 7 is also dealing with signal reconstruction, with a particular focus in clinical applications. We derive a real-time algorithm based on Kalman filter for the estimation of the ODF calculated in constant solid angle. On top of the Kalman filter, we design a motion detection algorithm, based on the monitoring of Kalman filter residuals. We show on real and synthetic data that this method give a sensitive and selective motion detection technique at no additional cost, when compared to hardware device based on in-scanner camera and computer vision algorithms.

Chapter 8 presents a method to design angular uniform point sets on several spheres in the q-space. By extending the electrostatic repulsion energy, originally proposed to construct antipodally symmetric, uniform point sets on the sphere [Jones et al., 1999a, Jansons and Alexander, 2003], we are able to construct point sets that have optimal angular coverage when considered as a whole. At the same time, the point sets also have optimal angular coverage on each sphere. We show on Monte-Carlo simulation that the use of these point sets as sampling protocols

in q-space significantly increases the angular resolution to reconstruct single fiber orientation, and fiber crossing angle.

Chapter 9 answers the question of the optimal design of experiments in q-space imaging, for the parametric reconstruction of the signal. We present a general method to find sampling schemes leading to minimal condition number, and possibly to exact estimation and reconstruction methods. This is applied to the reconstruction in the spherical harmonic basis in q-ball imaging, as well as in the modified SPF basis, in multiple q-shell imaging. As the sole constraint of minimal condition number leads to possibly many optimal configurations, we also impose that the sampling scheme have optimal angular coverage, based on the findings of Chapter 8.

Chapter 10 gives a general conclusion of this thesis, and put the contributions presented in this manuscript related to signal acquisition and reconstruction into perspective. We also present the kind of future work we consider, from applications of our contributions to a better understanding of tissue microstructure, to clinical research and clinical applications.

Chapter 2

Introduction (en français)

L'imagerie par résonance magnétique de diffusion (IRM de diffusion) est une technique inventée dans les années 1980 [Le Bihan and Breton, 1985, Merboldt et al., 1985, Taylor and Bushell, 1985], qui a rapidement montré un grand potentiel pour la détection précoce de certaines neuropathologies. Au cours des trente dernières années, une communauté grandissante de chercheurs s'est formée autour de cette modalité, en proposant de nombreuses innovations méthodologiques et technologiques. L'IRM de diffusion est maintenant un outil largement utilisé en clinique et en recherche pour caractériser de manière très fine la structure des tissus biologiques, et en particulier pour l'étude de la matière blanche du cerveau [Johansen-Berg and Behrens, 2009, Jones, 2010b]. Pour autant, la quantité d'information collectée à l'occasion d'une acquisition en IRM de diffusion est à la mesure de la complexité des tissus biologiques dans la matière blanche que l'on souhaite caractériser. Lorsqu'il s'agit de mesurer finement la structure des tissus, la préparation des protocoles d'acquisition et la reconstruction des caractéristiques propres à la diffusion posent des problèmes non triviaux, si l'on tient compte des limitations en pratique, dans un environnement clinique.

Le principe de l'IRM de diffusion repose sur une propriété physique du signal de résonance magnétique d'être modifié lorsque les particules sont en mouvement. Plus précisément, lorsque des gradients de champ magnétiques sont appliqués pendant de courts instants, et à un moment précis de la séquence d'acquisition, le signal d'écho mesuré est atténué [Stejskal and Tanner, 1965]. En répétant ce type d'acquisition, pour plusieurs gradients dans différentes directions et de différentes amplitudes, on acquière des images dites pondérées en diffusion, à partir desquelles on peut décrire très précisément le mouvement des molécules d'eau. La motivation principale de l'étude de la diffusion moléculaire, est que le déplacement des molécules d'eau a sein des tissus biologiques est contraint par les obstacles rencontrés. Ainsi, une analyse quantitative de la diffusion des molécules d'eau renseigne sur la microstructure des tissus sous-jacents, et ce à une résolution bien plus fine que ce que l'on observe en IRM conventionnelle.

On peut décrire la diffusion grâce à la densité de probabilité de déplacement des molécules d'eau, pendant une durée d'observation donnée. Dans un milieu libre, un verre d'eau par exemple, cette probabilité a une densité gaussienne, isotrope. Une des méthodes d'acquisition et de reconstruction en IRM de diffusion, que l'on appelle l'IRM du tenseur de diffusion [Basser et al., 1994a,b], se base sur une généralisation de ce modèle de diffusion gaussien dans un milieu libre. Le modèle probabiliste est un modèle gaussien multivarié, et le tenseur de diffusion est proportionnel à la matrice de covariance de cette distribution. L'IRM du tenseur de diffusion s'est imposée comme une technique incontournable, aussi bien en recherche que pour les applications cliniques, pour la détection de maladies neurologiques et pour la

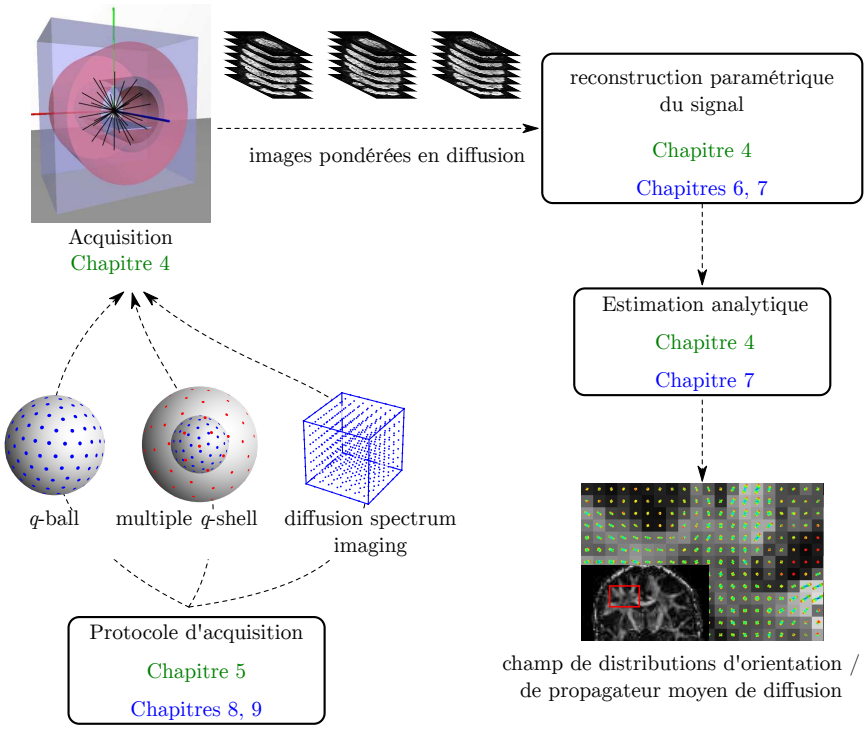

Figure 2.1: Schéma des différentes étapes en IRM de diffusion, depuis la préparation de la séquence d'acquisition à la reconstruction des informations locales de diffusion. Les chapitres qui traitent plus particulièrement chacune de ces étapes sont indiqués ; en vert, les chapitres d'état de l'art, et en bleu, les contributions.

planification pré-opératoire en neurochirurgie. Cependant, le fait de représenter l'anisotropie de la diffusion par une matrice de covariance empêche de décrire des configurations complexes, où plusieurs populations de fibres se croisent à l'intérieur d'un voxel. Cela a longtemps limité l'application à la trajectographie des fibres de la matière blanche, cette famille de méthodes qui reconstruit la connectivité structurelle dans la matière blanche du cerveau, à l'aide des informations de diffusion locales.

Étant donné ces limitations, plusieurs approches non basées sur un model on été proposées [Tuch et al., 2002, Tuch, 2004a], afin de décrire plus précisément le déplacement des molécules d'eau. Les méthodes dites à haute résolution angulaire permettent de décrire la diffusion et de discriminer plusieurs populations de fibres nerveuses au sein d'un même voxel. Elle ont permis d'améliorer considérablement la qualité des trajectographies de la matière blanche [Fillard et al., 2011]. Et pourtant, ces méthodes se limitent à une information strictement angulaire sur le phénomène de diffusion, et donc en quelque sorte sous-exploitent l'information donnée par les mesures pondérées en diffusion. C'est donc naturellement que plusieurs groupes de

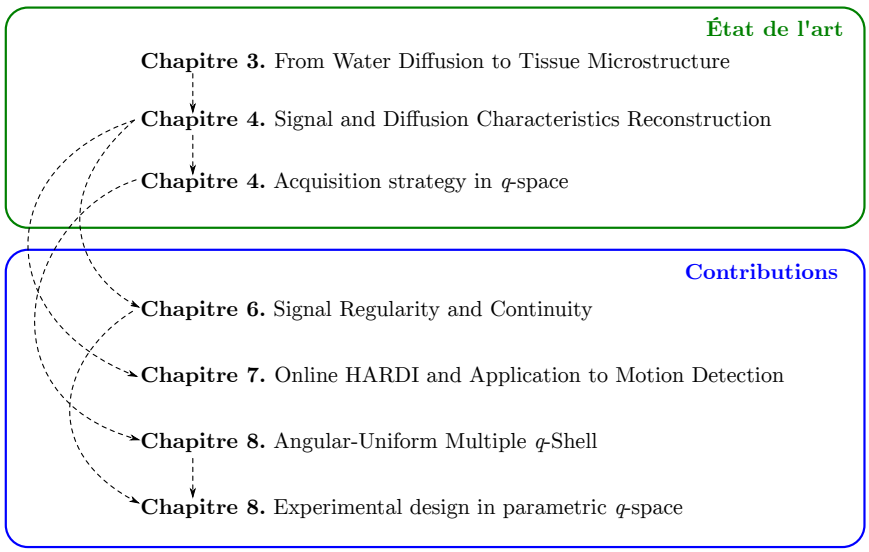

Figure 2.2: Schéma de lecture de la thèse.

recherche se sont penchés sur la reconstruction de la probabilité de déplacement des molécules d'eau, afin d'exploiter à la fois l'information radiale et l'information angulaire [Wedeen et al., 2005, Assaf et al., 2008]. Malheureusement, la plupart de ces techniques sont très couteuses en temps d'acquisition, et impliquent des schémas de reconstruction complexes. Cette thèse s'intéresse aux problèmes posés à la fois par l'acquisition et la reconstruction, soulevés par cette nouvelle tendance dans la communauté de l'IRM de diffusion. Nous poursuivons cette introduction en détaillant le plan suivi dans le manuscrit. Les étapes dans le processus classique d'acquisition sont représentées sur la Fig. 2.1, où l'on a fait référence aux chapitres correspondants dans cette thèse. Nous présentons également un schéma de lecture des différents chapitres sur la Fig. 2.2.

Chapitre 3 présente l'objet d'étude en IRM de diffusion : nous présentons brièvement l'anatomie du cerveau, et tout particulièrement la matière blanche. Puis, à partir d'un exemple virtuel de géométrie de fibres, qui modélise un faisceau de fibres dans la matière blanche, nous montrons grâce à une simulation comment le mouvement des molécules d'eau est affecté par les obstacles que représentent ces fibres. Cela montre la relation étroite entre la microstructure des tissus, et la diffusion des molécules d'eau, qui est au cœur de la motivation de l'IRM de diffusion en neurologie. Enfin nous présentons les outils mathématiques pour décrire le processus de diffusion, à savoir le propagateur moyen, et la fonction de distribution d'orientation.

Chapitre 4 présente les principe physiques qui expliquent la formation des images de diffusion, et donne un état de l'art des méthodes de reconstruction. En particulier, on présente la séquence à écho de spin et impulsion de gradients, ainsi que la notion d'espace de Fourier en IRM de diffusion (*q-space*). Les méthodes de reconstruction sont présentées et classées en deux catégories, suivant qu'elles se basent sur un modèle ou non. Parmi les méthodes qui ne dépendent pas d'un modèle particulier, nous présentons la transformation de Fourier sphérique, pour laquelle nous proposons une modification importante dans le Chapitre 6.

Chapitre 5 présente différentes approches pour l'élaboration de séquences d'acquisition dans l'espace de Fourier, pour reconstruire le tenseur de diffusion, le propagateur moyen ou la fonction de distribution d'orientation. Nous faisons la distinction entre acquisition sur une sphère (*q-ball*), des autres approches telles que l'acquisition sur une grille cartésienne (*diffusion spectrum imaging*), ou encore une approche intermédiaire, où l'échantillonnage se fait sur quelques sphères concentriques (*multiple q-shell*). Ces méthodes permettant de générer des schémas d'acquisition sont soit purement géométrique, soit liées à un algorithme de reconstruction particulier.

Chapitre 6 présente la première contribution de cette thèse, sur l'estimation paramétrique du signal dans l'espace de Fourier. Une base de fonctions a récemment été proposée [Assemlal et al., 2009b], permettant de modéliser le signal dans l'espace $\mathbb{R}^3$ entier. Cependant, nous montrons que les fonctions de cette base ne sont pas continues en zéro. Plus précisément, le sous-espace de fonctions représentées dans cette base qui sont continues a une dimension significativement inférieure à l'espace de départ. Nous proposons de caractériser ce sous-espace, et en proposons une base. De plus, pour améliorer le comportement de l'estimation en présence de bruit, nous proposons un opérateur de régularisation de Laplace. L'expression de cet opérateur est calculée, et on montre qu'il s'écrit comme une forme quadratique des coefficients dans la nouvelle base. Le problème d'estimation sous contrainte de régularité a donc une solution analytique, ce qui rend la méthode rapide et efficace.

Chapitre 7 est également une contribution sur la reconstruction, avec un point de vue plus orienté vers l'application clinique. Nous présentons un algorithme en temps réel basé sur le filtre de Kalman, pour l'estimation de la densité marginale de distribution d'orientation. Basé sur le filtre de Kalman, nous développons un algorithme de détection de mouvement, qui repose sur une analyse des résidus du filtre de Kalman. Nous montrons dans une partie expérimentale, sur des données réelles et des données synthétiques, que cette méthode donne une technique de détection du mouvement à la fois sensible et sélective, sans surcoût, comparé aux méthodes basées sur une caméra et des algorithmes de vision par ordinateur.

Chapitre 8 présente une méthode pour générer des ensembles de points sur plusieurs sphères, pour l'acquisition dans l'espace de Fourier. En proposant une extension de l'analogie électrostatique utilisée en *q-ball* [Jones et al., 1999a, Jansons and Alexander, 2003], nous proposons une énergie faisant en sorte de privilégier des configurations uniformes sur chacune des sphères, mais également offrant une couverture angulaire optimale, globalement. Grâce à des simulations de Monte-Carlo, nous montrons que cette approche de l'échantillonnage dans l'espace de Fourier permet de bien améliorer la résolution angulaire, qu'il s'agisse de reconstruire une fibre ou plusieurs fibres dans un voxel.

Chapitre 9 s'intéresse à la question de l'échantillonnage optimal dans l'espace de Fourier, pour l'estimation paramétrique du signal. Nous présentons une méthode générale pour trouver des schémas d'échantillonnage qui ont un nombre de conditionnement minimal, et qui permettent un reconstruction exacte dans une base donnée. On applique cela à la base des harmoniques sphériques en *q-ball*, ainsi que dans la base Fourier sphérique nouvellement proposée pour l'élaboration de protocoles sur plusieurs sphères. Étant donné qu'il existe généralement une infinités de protocoles d'acquisition ayant un nombre de conditionnement minimal, on s'intéresse à celui qui a en plus la couverture angulaire optimale, grâce à l'approche présentée dans le Chapitre 8.

Chapitre 11 présente une conclusion générale de la thèse, et replace les contributions liées à l'acquisition et à la reconstruction en perspective. Nous présentons également les thèmes de recherche futurs que nous aimerions aborder, de l'application de nos contributions à une meilleure compréhension de la microstructure des tissus, aux applications en clinique et en recherche clinique.

Part II

Background

Chapter 3

From Water Diffusion to Tissue Microstructure

Contents

Overview

What kind of information does diffusion MRI bring for the discovery of brain white matter structures? How does the observation of water molecules displacement provide information on tissue microstructure, at a microscopic scale, several orders of magnitude beyond conventional MRI resolution? What are the mathematical tools developed to describe the diffusion process?

This introductory section first provides a quick overview of the anatomy of the central nervous system, with a special focus on brain white matter, the gold application of diffusion MRI. Then we present the close relation between microstructure and water diffusion. In particular, we show on an illustrating example how the observation of a population of water molecules displacement within a restricted medium informs on the configuration of the underlying geometry. Finally, we present the mathematical and computational tools for a quantitative description and analysis of the diffusion process.

Keywords brain anatomy; water diffusion; ensemble average propagator; orientation distribution function.

3.1 Introduction

At a temperature above the absolute zero, water molecules undergo a random motion due to thermal energy. Using special acquisition sequence, it is possible to get information from this microscopic motion in MRI. The technique, known as Diffusion MRI, originates in the mid 80's [Le Bihan and Breton, 1985, Merboldt et al., 1985, Taylor and Bushell, 1985]. Before describing the physical aspects of diffusion MRI in the next chapter, we introduce here the close relation between water molecules displacement and tissue microstructure.

We first briefly present some notions of brain anatomy, with a special focus on white matter. Then we show how tissue geometry constrains the water diffusion, and we present a synthetic example of fiber bundle. We introduce the main mathematical concepts to quantify the diffusion process in diffusion MRI, namely the Ensemble Average Propagator (EAP), the Orientation Distribution Function (ODF) and some derived characteristics. Finally, we show some applications in the study of brain structural connectivity mapping.

3.2 Anatomy of the central nervous system

The central nervous system (CNS) is constituted of the brain, protected by the skull, and the spinal cord, protected by the vertebral column (see Fig. 3.1).

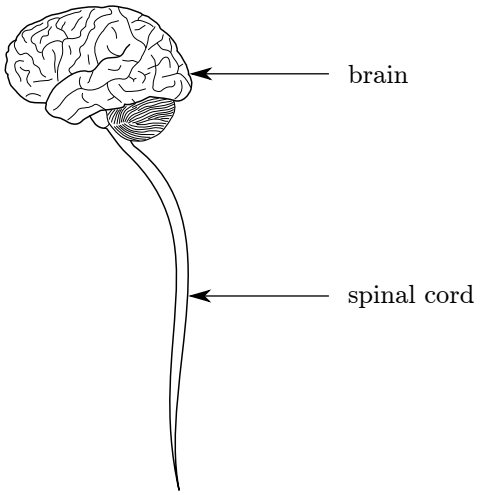

Figure 3.1: The central nervous system.

The brain is divided into two hemispheres. The superficial part of the brain is called the cortex, and has several grooves on its surface called the sulci. The most important sulci are the fissure of Rolando, the fissure of Sylvius and the parieto-occipital sulcus. They divide each hemisphere into the frontal lobe, the parietal lobe, the occipital lobe and the temporal lobe (see Fig. 3.2).

At a microscopic scale, the brain is made of hundreds of billions of cells called the neurons. The bodies of neuronal cells form the grey matter. The myelinated axons, which are connecting neurons together (see Fig. 3.3), are grouped into bundles, and form the white matter. As visible on Fig. 3.4, the white matter occupies most of the subcortical volume, and therefore plays an essential role in the brain function.

The function of white matter tracts is to route the messages from one population of neurons to another. Therefore, being able to map the structure of brain white matter has long been a key issue in the development of neurology. The first detailed study of white matter was carried out in the nineteenth century [Golgi et al., 2001, Ramon y Cajal, 1892]. It was made possible by the technological advance in microscopy and staining. For a detailed history of brain anatomy, the interested reader might take a look at the excellent related chapter in Wassermann [2010].

Since then, the development of diffusion tensor MRI [Basser et al., 1994a,b] and recent developments in diffusion MRI have provided a unique tool for the non-invasive, *in vivo* analysis of brain connectivity. Making the magnetic resonance signal sensitive to the translational motion of water molecules, diffusion tensor MRI infers the underlying tissue structure. In the next section, we show how the study of water molecules displacement is related to the microstructure, and how it can be characterized quantitatively to finally map the connections in the brain.

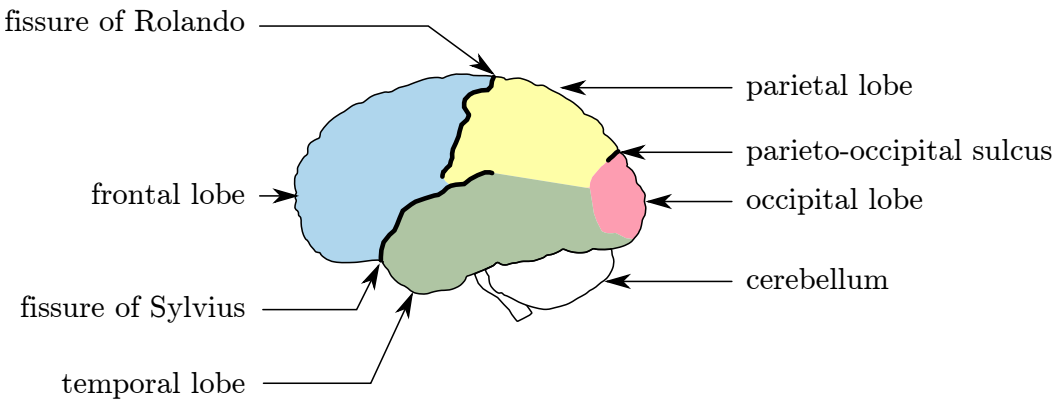

Figure 3.2: The lobes and main sulci of the brain cortex. Adapted from Gray [1918]

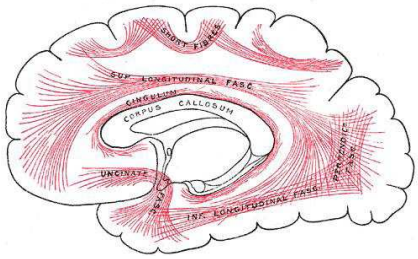

Figure 3.3: Some important commissural fiber tracts, sagittal section. Reproduced from Gray [1918]

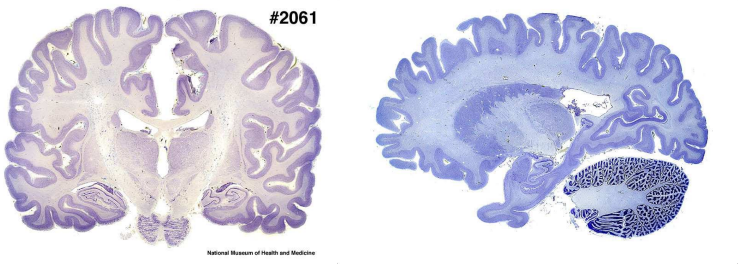

Figure 3.4: (left) Coronal section and (right) sagittal section of a human brain, with cell stain. Due to the cell stain, grey matter (cortex and basal ganglia) appears dark, while the white matter appears clear. Reproduced from Welker et al..

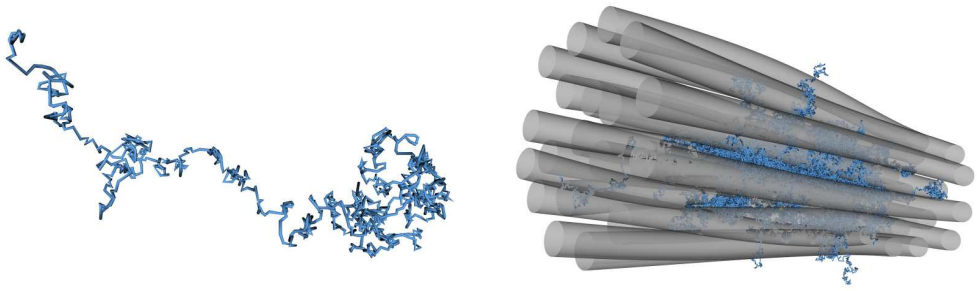

Figure 3.5: (left) Free Brownian motion of a water molecules. (right) A bundle of white matter fibers, and water molecules trajectory within. We simulated here a bundle of 19 fibers, each fiber has a 5 µm radius, and we observe the trajectory of 100 water molecules, over 60 ms.

3.3 Structure and restricted diffusion

As seen in the previous section, the structure of white matter is essentially fibrous. Due to the myeline sheath around the axons, the displacement of water molecules is hindered by the fibers. Diffusion MRI is based on the hope that the study of water molecules motion within the tissue could provide insights into the organization of the fibers.

3.3.1 Free diffusion and restricted diffusion

In a free medium, the molecules undergo a Brownian motion, first described quantitatively in Einstein [1956]. In particular, the average square displacement during the time interval τ is related to the diffusion coefficient D_0

$$\overline{\mathbf{R}^2} = 6D_0\tau. \tag{3.1}$$

An example of Brownian motion in a free and a constrained medium is shown on Fig. 3.5.

3.3.2 An example of geometry

In diffusion MRI, we observe a population of water molecules rather than a single molecule. To show this, we consider again the example of extra-axonal diffusion, on the synthetic fiber bundle presented on Fig. 3.5. We generated a population of 100000 water molecules, and simulated their Brownian motion within the sample. The collision with fibers wall is considered. For a comparison, we also generated the same population of particles, diffusing in an unconstrained medium. Results of the simulation are depicted on Fig. 3.6.

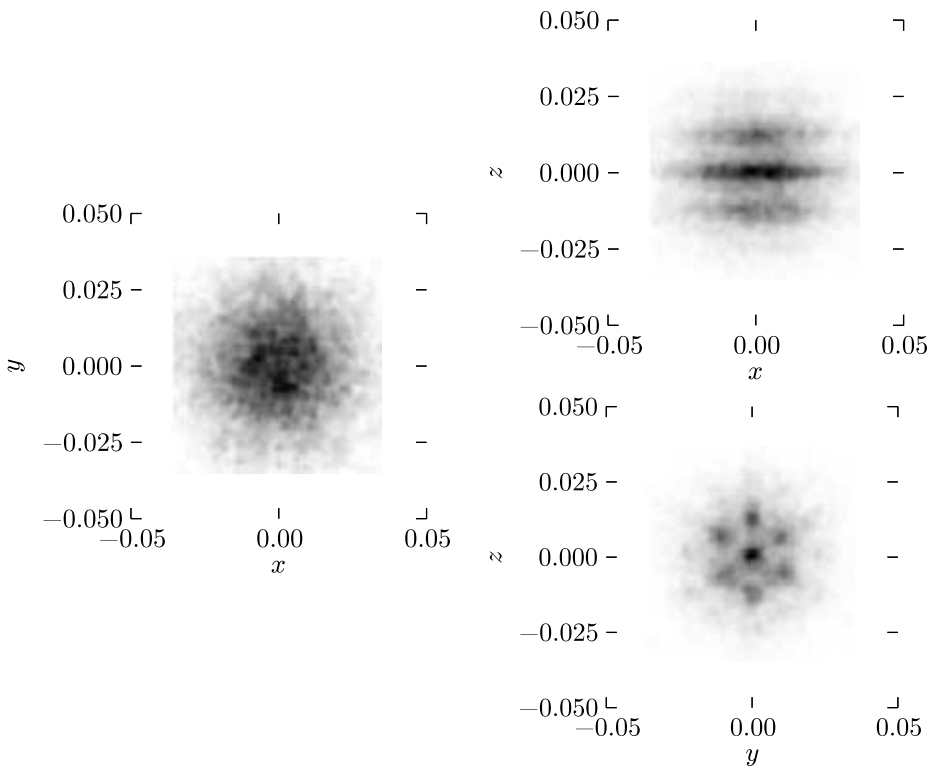

Figure 3.6: Displacement of 10000 water molecules over the diffusion time $t = 60$ ms. (left) unrestricted medium, and (right) within the population of fibers presented on Fig. 3.5. The fibers axis is parallel to the x-axis.

This model is not intended to be realistic, and beyond this model used for illustration, we can cite here more realistic simulators [Yeh, 2011, Wang et al., 2012], and in the context of diffusion MRI, the well-known Camino Toolkit Cook et al. [2006]. Anyway this experience reveals remarkable differences between the probability of water molecules displacement in a constrained and an unconstrained medium (see Fig. 3.6).

Slower diffusion We first notice that the molecules diffuse faster in an unconstrained medium than within a bundle of fibers. By quantifying the diffusivity, we could be able to characterize the density of the underlying tissue structure.

Anisotropic diffusion Besides, the diffusion of water molecules is preferred in the direction of the fibers. Then by analyzing the anisotropy of water molecules, and the principal directions of diffusion, it should be possible to infer the main directions of the underlying structure in case of a fiber bundle.

Structure Last, in the plane perpendicular to the fibers, we clearly observe a pattern, which could be related to the geometry of the fiber packing, and then to the diameter of the fibers and the dimension of the extra-axonal space [Assaf et al., 2008].

This simple experience illustrates the great potential of diffusion water molecules reconstruction in the characterization of tissue microstructure. In the next section, we present mathematical tools to quantify and analyse these observations.

3.4 Quantitative description of diffusion characteristics

In this section, statistical tools are presented to describe the diffusion characteristics, at the scale of a voxel.

3.4.1 Ensemble Average Propagator

In diffusion NMR and diffusion MRI, we measure the diffusion of a whole population of water molecules within a sample or within a voxel, respectively. Formally, the diffusion is a random process, and is characterized by the so-called Ensemble Average Propagator (EAP), denoted by P throughout this manuscript. It is defined as

$$P(\mathbf{r};\tau) = \int_{\mathcal{V}} p(\mathbf{r}_0 + \mathbf{r}; \mathbf{r}_0, \tau) \mathrm{d}\mathbf{r}_0, \tag{3.2}$$

where $p(\mathbf{r}_0+\mathbf{r};\mathbf{r}_0,\tau)$ is the probability that a molecule initially at $\mathbf{r}_0$ moves to $\mathbf{r}_0+\mathbf{r}$ over the diffusion time τ, and $\mathcal{V}$ is the volume of the voxel (or the volume of the

sample in NRM). In a free medium, the EAP is simple and is given by the Gaussian probability density function [Einstein, 1956, Callaghan, 1991b]

$$P(\mathbf{r};\tau) = (4\pi D_0 \tau)^{-3/2} \exp\left(-\frac{||\mathbf{r}||^2}{4D_0\tau}\right). \tag{3.3}$$

The self-diffusion coefficient of water D_0 is approximately $2.2 \cdot 10^{-3}$ mm^2 s^{-1} under normal conditions of temperature and pressure.

When the diffusion is hindered by an underlying structure, the diffusion is more complex, as shown on the example Fig. 3.6. The EAP is then closely related to the structure. In the remaining of this thesis, the diffusion time τ is omitted for the sake of clarity, and the notation $P(\mathbf{r})$ is retained.

The Gaussian assumption

The EAP in a free medium is an isotropic multivariate Gaussian, with covariance given by Eq. 3.1. A natural generalization when one wants to capture anisotropy is to extend this to anisotropic multivariate Gaussian. This is the model underlying the Diffusion Tensor imaging [Basser et al., 1994a,b]. The diffusion EAP is given by

$$P(\mathbf{r}) = \frac{1}{\sqrt{(4\pi\tau)^3|\mathbf{D}|}} \exp\left(-\frac{\mathbf{r}^{\mathrm{T}}\mathbf{D}^{-1}\mathbf{r}}{4\tau}\right). \tag{3.4}$$

The 3×3 positive matrix $\mathbf{D}$ is the so-called diffusion tensor.

Visualization

The EAP is a function from $\mathbb{R}^3$ to $\mathbb{R}^+$, and therefore cannot be represented on the 2D surface of this manuscript. Depending on the application, we shall represent 2D slices of this function as grey-scale images. Alternatively, the angular profile $P(r \cdot \mathbf{u})$ for a given radius r can be rendered as a 3D surface. An example of both visualizations is shown on Fig. 3.7, for the anisotropic Gaussian EAP.

In the case of diffusion tensor imaging, the diffusion tensor can be represented as an ellipsoid, whose major axes correspond to the principal eigenvectors of the tensor. An example of the image obtained from diffusion tensor imaging is reproduced on Fig. 3.8.

3.4.2 Orientation Distribution Function

In the study of brain white matter connectivity, the angular aspect of the diffusion probability is of utmost importance, as it reveals the directions of the underlying bundles of axon. This information is captured by a spherical function, known as the Orientation Distribution Function (ODF). This angular function was initially

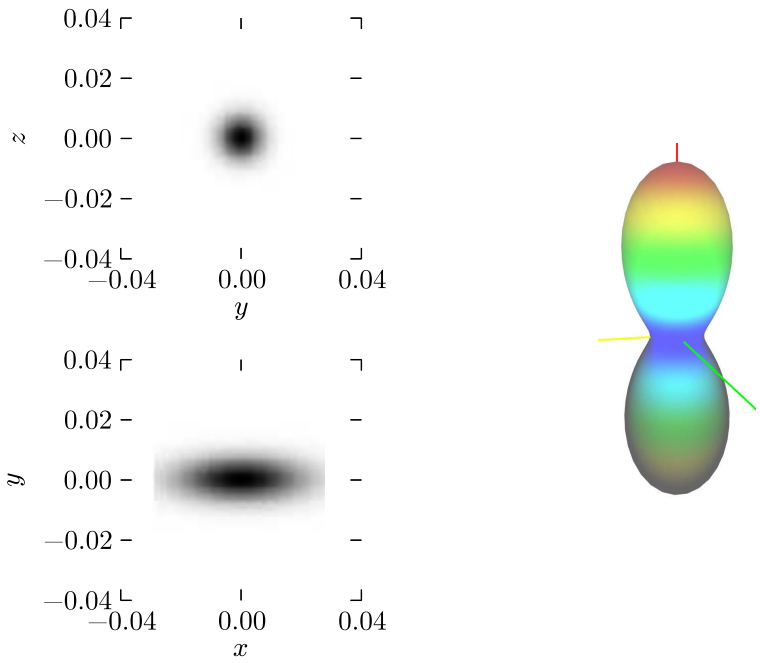

Figure 3.7: Gaussian EAP visualization, major axis is x-axis. (left) 2D slices, on (top left) yz-plane and (bottom left) xy-plane. (right) angular profile, $r_0 = 15$ µm.

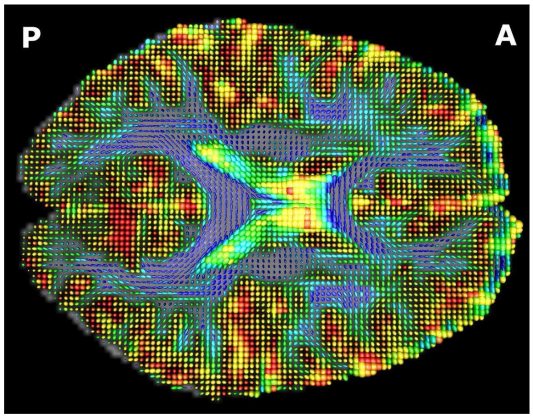

Figure 3.8: Diffusion tensors represented as ellipsoids, axial slice. The color codes the fractional anisotropy (red: low anisotropy, blue: high anisotropy). Courtesy of Lenglet [2006].

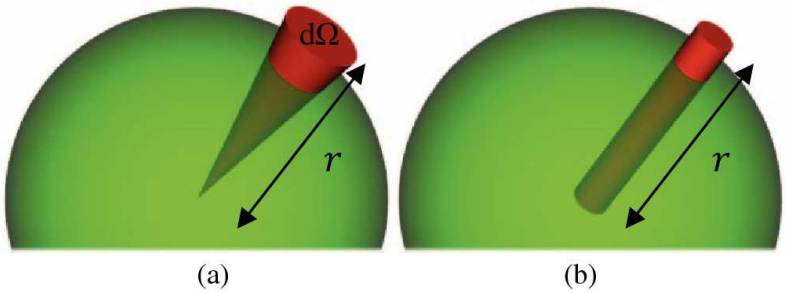

Figure 3.9: Illustration of the radial integration leading to (a) the ODF calculated in constant solid angle [Tristán-Vega et al., 2009, Aganj et al., 2010a], and to (b) the original ODF, ψ_{T}, defined in Tuch [2004a], Reproduced from Aganj et al. [2010a].

defined [Tuch, 2004a] as the radial integration of the EAP, as

$$\psi_{\mathrm{T}}(\mathbf{u}) = \frac{1}{Z}\int_0^\infty P(r\cdot\mathbf{u})\mathrm{d}r. \tag{3.5}$$

Z is a normalization constant, so that ψ_{T} integrates to 1 on the unit sphere. More recently, the definition of the ODF was corrected to match the marginal angular probability of diffusion [Tristán-Vega et al., 2009, Aganj et al., 2010a]. The definition of this ODF, ψ, is

$$\psi(\mathbf{u}) = \int_0^\infty P(r\cdot\mathbf{u})r^2\mathrm{d}r. \tag{3.6}$$

ψ is also referred to as the ODF calculated in constant solid angle, as the factor r^2 in the integration accounts for the Jacobian of the parameterization $\mathbf{r} = r\cdot\mathbf{u}$. This is illustrated on Fig. 3.9. In this thesis, unless explicitly stated, we use preferentially the latter ODF, as it is a probability density function and needs not be normalized. Moreover, it has intrinsically sharper peaks, which is important to detect the fiber directions in brain white matter.

3.4.3 Scalar measurements

In order to present an information as concise as possible, it is important to develop scalar measurements from the EAP and the ODF. This is an active field of research, directed towards the search of new biomarkers, for the early detection of neurological diseases. We present here three model-free quantities: the Mean Square Displacement (MSD), the return-to-origin probability (RTO), and the Generalized Fractional Anisotropy (GFA). We also present two popular scalar measurements in the context of Gaussian diffusion assumption: the Fractional Anisotropy and Mean Diffusivity.

Figure 3.10: Diffusion tensors, represented as ellipsoids, for FA ranging from 0.0 to 0.6. The Mean Diffusivity is constant across the tensors.

Mean Square Displacement This is the mean square value of the ensemble average propagator. It is defined by

$$\mathrm{MSD} = \int_{\mathbb{R}^3} P(\mathbf{r})||\mathbf{r}||^2 \mathrm{d}\mathbf{r}. \tag{3.7}$$

Return-to-Origin probability The Return-to-Origin (RTO) probability [Hürlimann et al., 1995, Mitra et al., 1995] is the probability for a molecule to come back to its starting position, once the diffusion time τ is elapsed. It is defined as

$$\mathrm{RTO}(\tau) = P(\mathbf{0}; \tau). \tag{3.8}$$

The RTO is to be compared to the same quantity in free diffusion, which is $\mathrm{RTO}_0 = (4\pi D_0 \tau)^{-3/2}$. The RTO quantifies, in general, how restricted the molecules are in their motion.

Generalized Fractional Anisotropy The Generalized Fractional Anisotropy (GFA) is defined as the normalized standard deviation of the orientation distribution function [Tuch, 2004a]:

$$\mathrm{GFA} = \left(\frac{\int_{\mathcal{S}^2} (\psi(\mathbf{u}) - 1)^2 \mathrm{d}\Omega}{\int_{\mathcal{S}^2} \psi(\mathbf{u})^2 \mathrm{d}\Omega} \right)^{1/2}. \tag{3.9}$$

This index lies in the interval $[0, 1]$, and measures how different the ODF is from a uniform, isotropic diffusion (constant ODF on the sphere).

In the case of Gaussian diffusion assumption, the diffusion tensor can be written as

$$\mathbf{D} = \mathbf{R}^{\mathrm{T}} \begin{pmatrix} \lambda_1 & 0 & 0 \\ 0 & \lambda_2 & 0 \\ 0 & 0 & \lambda_3 \end{pmatrix} \mathbf{R}, \tag{3.10}$$

where $\mathbf{R}$ is a rotation matrix, and λ_i are the eigenvalues of the diffusion tensor. From this decomposition, several rotational-invariant quantities of interest are defined [Westin et al., 2002].

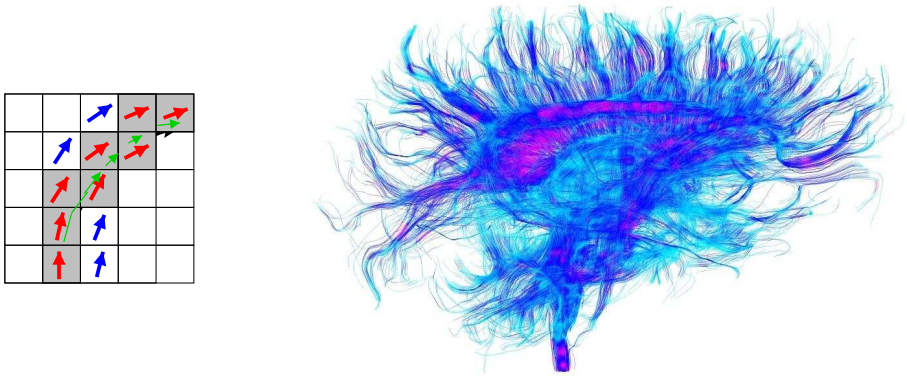

Figure 3.11: (left) description of streamline tractography algorithm: from the principal eigenvector of the diffusion tensor, we reconstruct the trajectory of white matter fibers. Reproduced from Poupon [1999]. (right) An example of fiber tracking on the whole brain. Courtesy of Lenglet [2006].

Mean Diffusivity The Mean Diffusivity (MD) is defined as the average of the eigenvalues of the diffusion tensor $\mathbf{D}$:

$$\mathrm{MD} = \frac{1}{3}\sum_{i=1}^{3}\lambda_i. \tag{3.11}$$

The MD is linearly related to the MSD, through the generalization of Eq. 3.1 to isotropic Gaussian diffusion: MSD = 2 MD τ.

Fractional Anisotropy The Fractional Anisotropy (FA) is another useful quantity defined as the normalized standard deviation of the eigenvalues of the diffusion tensor [Pierpaoli and Basser, 1999]. Formally,

$$\mathrm{FA} = \left(\frac{3\sum_{i=1}^{3}(\lambda_i - \mathrm{MD})^2}{2\sum_{i=1}^{3}\lambda_i^2} \right)^{1/2}. \tag{3.12}$$

The FA ranges from 0 to 1, and characterized the anisotropy of the diffusion tensor. The value 1.0 corresponds to a degenerate tensor, with at least one vanishing eigenvalue. Various tensors, represented as ellipsoids, are depicted on Fig. 3.10, for FA ranging from 0.0 to 0.6.

3.4.4 Application to the study of brain connectivity

Diffusion MRI maps the local anisotropy of water molecules diffusion. By integrating the principal directions of diffusion over the whole white matter, one can

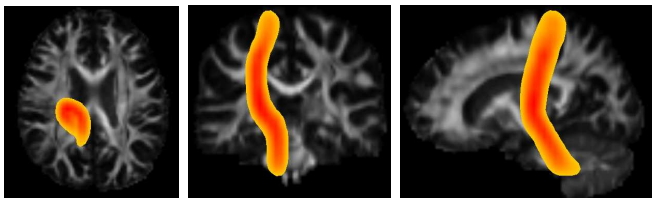

Figure 3.12: Clustering of the cortico-spinal tract, using the Gaussian framework in Wassermann et al. [2010]. Courtesy of D. Wassermann.

tract the connecting paths from one region of the brain to another. This process is known as fiber tractography [Poupon, 1999, Mori et al., 1999, Basser et al., 2000]. A sketch of the streamline tractography method [Mori et al., 1999] and a result of tractography are shown on Fig. 3.11.

Studying the results of fiber tractography requires appropriate treatment however. As shown on Fig. 3.11, the tractography algorithms on the whole brain usually return a large population of fibers. Among this population, some fibers are more relevant than others on an anatomical point of view. Since then, statistical tools for the analysis of these large populations have been developed. An active field of research is dedicated to the clustering of fibers on bundles, to recover the main tracts in the brain white matter O'Donnell and Westin [2007], Wassermann et al. [2010].

3.5 Conclusion

In this chapter, we have presented the main motivations for the observation of water diffusion for its application to the study of brain anatomical connectivity. We have seen how the presence of tissue boundary affects the motion of water. By observing the motion of a population of water molecules within a tissue, it is possible to infer the structure of the underlying structure.

In the next chapter, we present the physics of diffusion MRI. We show how the MR signal is affected in the presence of spin motion. We introduce the main challenges in acquisition, signal processing and reconstruction from the MR signal measurement to the estimation of diffusion characteristics (EAP, ODF, and derived quantitites) from the measurement of the MR signal.

Chapter 4

Physics of Diffusion MRI: Reconstruction of Diffusion Characteristics

Contents

Overview

What are the main principles of nuclear magnetic resonance measurements, and magnetic resonance images reconstruction? How can we measure water diffusion through MRI? In this chapter, we present the basic principles of NMR, MRI and diffusion MRI. Then we introduce state-of-the-art methods for the reconstruction of diffusion characteristics presented in the previous chapter, from diffusion signal measurements.

Keywords pulse gradient spin echo; diffusion gradient; orthogonal bases; q-ball imaging; q-space sampling.

4.1 Physics of NMR, MRI and diffusion MRI

We first briefly present the physics underlying nuclear magnetic resonance (NMR) and the construction of images in MRI. Then we introduce the pulsed-gradient spin echo sequence (PGSE), and the resulting signal attenuation in presence of spin displacement.

4.1.1 Magnetic spin and Larmor frequency

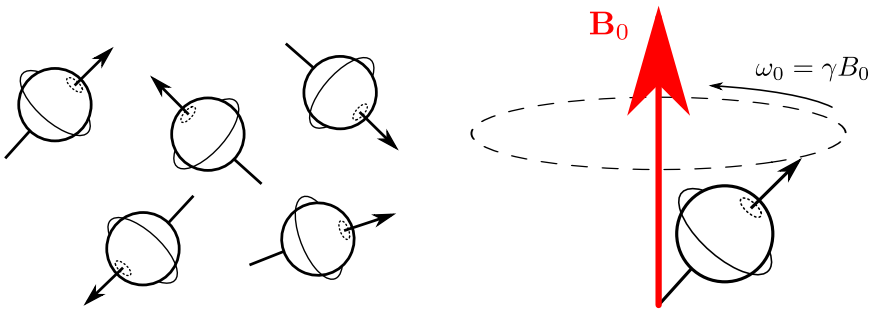

Figure 4.1: Magnetic spin: (left) random orientation, (right) precession around the magnetic field $\mathbf{B}_0$ at the Larmor frequency ω_0.

The principles of NRM were originally described in Bloch [1946], Purcell et al. [1946], who both received the Nobel prize in 1952 for their major discovery. NMR uses the property of magnetic spins immersed in a strong magnetic field $\mathbf{B}_0$ to align their moment with the magnetic field. More precisely, the spins rotate about this field at a speed called the Larmor frequency, ω_0, proportional to the strength of the magnetic field $\omega_0 = \gamma||\mathbf{B}_0||$ (see Fig. 4.1), where γ is the gyromagnetic ratio. The protons in water molecules do have a magnetic spin, and precisely, 80 percent of the human body is made up of water. This explains why NMR principles has been applied to the study of biological shortly after its discovery. The associated

gyromagnetic ratio is $42.6\,\mathrm{MHz}\cdot\mathrm{T}^{-1}$, and therefore for a clinical 3 T scanner, the Larmor frequency is 127.6 MHz.

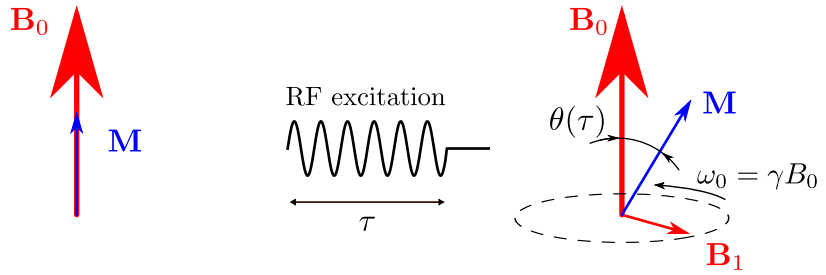

(a) At rest (b) Under a RF excitation

Figure 4.2: Net magnetization in presence of a strong magnetic field.

At resting state, the spins do not rotate in phase, and the transverse contributions of spins tends to cancel each other. The resulting magnetization, also known as the net magnetization, $\mathbf{M}$, is aligned with the magnetic field $\mathbf{B}_0$ (see Fig. 4.2). However, when excited by a radio signal tuned at the Larmor frequency, materialized by a transverse magnetic field $\mathbf{B}_1$, they begin to rotate in phase. As a result, the net magnetization rotates at the same frequency, and begins to precess away from the $\mathbf{B}_0$ axis (see Fig. 4.2). The angle of rotation θ is known as the flip angle, and depends on the duration and the shape of the radio frequency pulse.

4.1.2 From NMR to MRI

As already stated, the Larmor frequency ω_0 depends on the strength of the magnetic field. Hence by applying a magnetic field gradient, it is possible to encode the spatial position of spins. Therefore, the position of the excited tissue from which the signal originated can be deduced from the frequency. By changing the orientation of the gradient, as in the simplified acquisition sequence sketched on Fig. 4.3, it is possible to reconstruct a 3D image of the brain. This technique was first proposed in 1950 for one dimensional MRI [Carr, 2004], and has been extended later on to produce 3D images Lauterbur [1973].

4.1.3 Signal attenuation in presence of spin motion

As seen in Chapter 3, water molecules undergo a spontaneous motion due to thermal energy. It is possible to quantify the spin motion using magnetic field gradients. The first acquisition sequence dedicated to the measurement of spin motion is due to Stejskal and Tanner [1965], sketched on Fig. 4.4.

The application of a magnetic field gradient before the 180° RF pulse introduces a phase shift to the spins. If the spins had remained still during the time interval Δ,

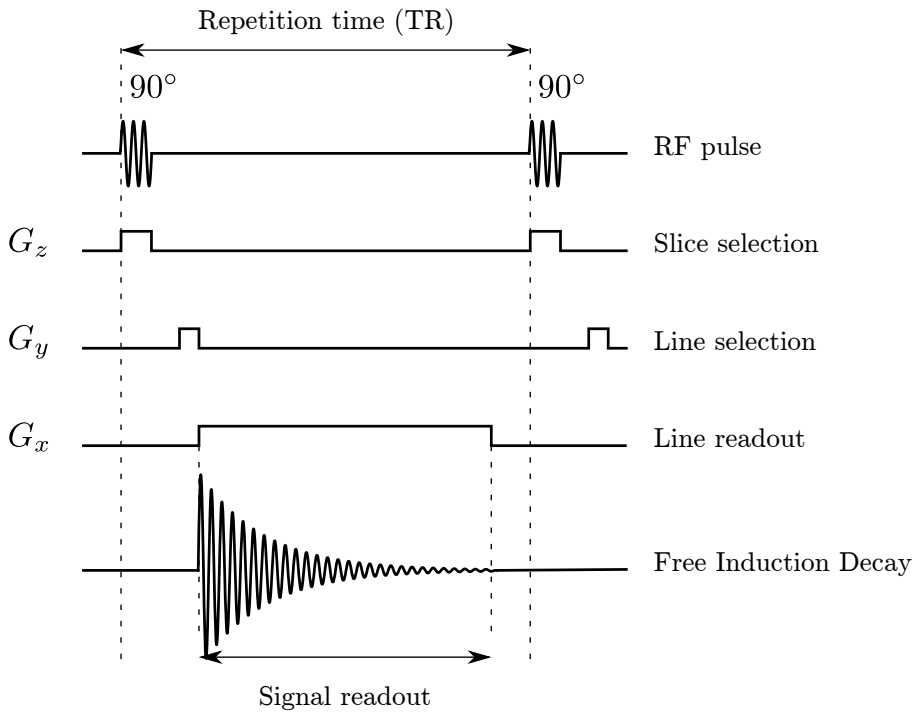

Figure 4.3: A simplified MRI acquisition sequence. G_x, G_y and G_z denote the linear magnetic field gradients applied to encode spatial position of spins.

therefore the application of the exact same gradient after the 180° RF pulse would cancel the phase shift. However, due to diffusion, the spins that have moved in the same direction as the gradient to not come exactly in phase, and the resulting measured echo signal is attenuated.

In the general case, this attenuation depends on the shape and the duration of the diffusion gradient pulse, and is difficult to express [Callaghan, 1991a]. Indeed, water molecules also diffuse during the time interval δ, corresponding to the application of the diffusion gradient. However it is generally possible to use a first assumption about the gradient pulse, called the narrow-pulse assumption:

$$\delta \ll \Delta. \tag{4.1}$$

Under this assumption, we introduce the wavevector $\mathbf{q}$:

$$\mathbf{q} = \frac{\gamma}{2\pi} \int_0^\delta \mathbf{g}(t) \mathrm{d}t, \tag{4.2}$$

where $\mathbf{g}(t)$ is the time-dependent magnetic field gradient applied during the time interval δ. When the gradient pulse has a rectangular profile, the gradient $\mathbf{g}$ is constant during the pulse, and this rewrites simply as $\mathbf{q} = (2\pi)^{-1}\gamma\delta\mathbf{g}$.

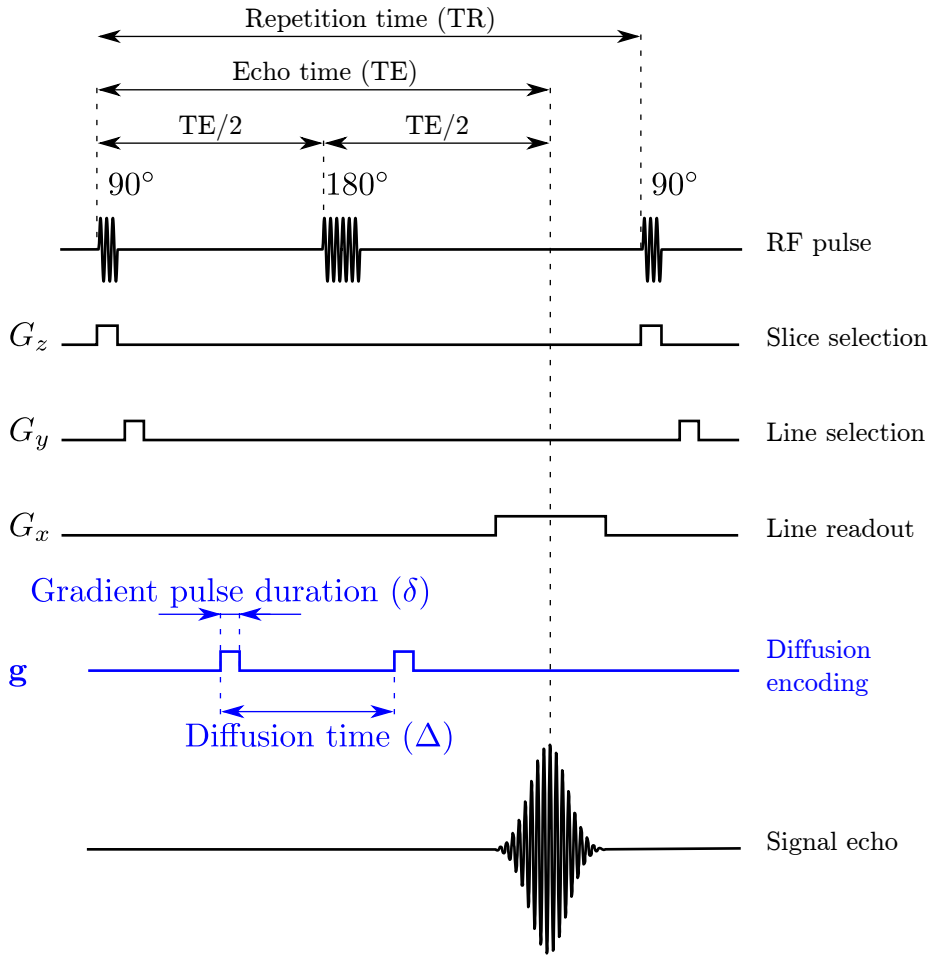

Figure 4.4: The Stejskal and Tanner acquisition sequence in MRI. Diffusion-specific elements are depicted in blue. In particular, note the pair of so-called diffusion gradient pulses, before and after the 180° RF pulse, separated by the diffusion time Δ.

The signal attenuation $E(\mathbf{q})$, defined as the ratio $S(\mathbf{q})/S(\mathbf{0})$, is related to the ensemble average propagator (EAP) through a Fourier transform

$$E(\mathbf{q}) = \int_{\mathbb{R}^3} P(\mathbf{r}; \Delta) e^{-2\imath\pi \mathbf{q}\cdot\mathbf{r}} \mathrm{d}\mathbf{q}. \tag{4.3}$$

The wavevector $\mathbf{q}$ defines the reciprocal space, referred to as the q-space. By repeating the acquisition sketched on Fig. 4.4, for different direction and strength of the diffusion gradient $\mathbf{g}$, and possibly different gradient pulse duration δ, we acquire different 3D images of the same object. Such images are called diffusion weighted images. From a series of diffusion weighted images, which correspond to samples in the q-space, we can reconstruct the ensemble average propagator, and its derived characteristics introduced in Chapter 3. The next two sections give an overview of reconstruction and acquisition methods, from q-space to water diffusion.

4.2 From MR signal attenuation to water diffusion

In this section, we show several methods exploiting the relation between the diffusion signal attenuation and the ensemble average propagator (EAP) to reconstruct diffusion characteristics. We present the discrete Fourier sampling and reconstruction (known as diffusion spectrum imaging), several model-based reconstruction methods (in particular diffusion tensor imaging). Finally, we present some continuous representations in orthonormal bases, in q-ball imaging and q-space imaging.

4.2.1 Diffusion Spectrum Imaging

Water diffusion and MR signal attenuation are linked through a Fourier transform (see Eq. 4.3). The technique known as diffusion spectrum imaging (DSI) [Wedeen et al., 2005] implements the reconstruction of the EAP from a dense sampling of the q-space on a regular lattice, and discrete inverse Fourier transform (see Fig. 4.5). The propagator P is therefore reconstructed on a discrete dual grid, and can be interpolated to evaluate characteristics such as the orientation distribution function (ODF), the mean square displacement (MSD) or the return to origin probability (RTO) (see Section 3.4). This method was applied successfully in brain imaging, for the reconstruction of complex configurations of fibers, including fiber crossing [Wedeen et al., 2005].

Under the apparent simplicity of the DSI technique, several drawbacks restrict its application in a clinical context. First, in order to satisfy the Shannon-Nyquist conditions, the sampling volume in q-space must be sufficiently large. More precisely, to reconstruct the propagator on a grid of spacing Δr_0, the maximum vector length, q_0, in reciprocal space should be proportional to $2/\Delta r_0$. The resolution of reconstructed EAP is therefore directly limited by hardware, as the limiting parameter for q is the magnitude of the magnetic field gradient. Typical values in clinical

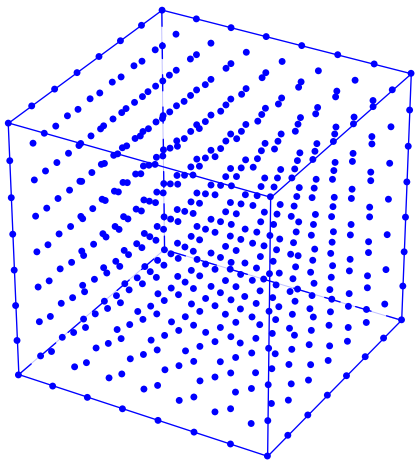

Figure 4.5: q-space sampling in diffusion spectrum imaging (DSI), on a regular $8 \times 8 \times 8$ Cartesian lattice.

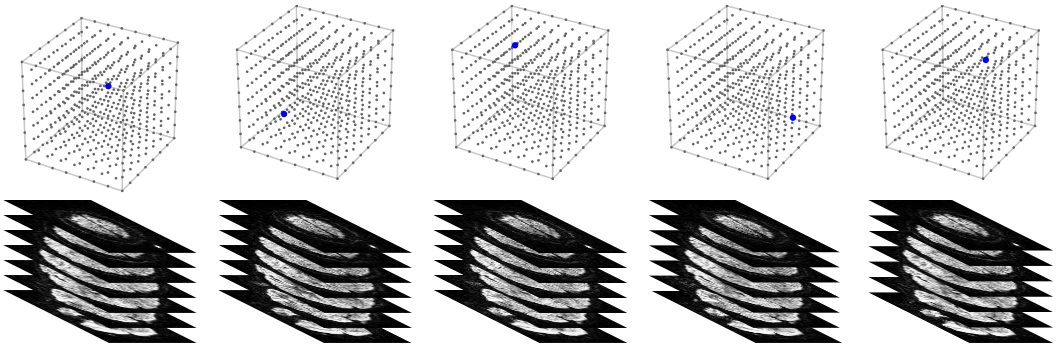

Figure 4.6: Diffusion MRI is a 6D imaging modality. (top) Coordinate of the wavevector in the q-space, (bottom) corresponding diffusion weighted image.

scanners are of the order of $100\,\mathrm{mT} \cdot \mathrm{m}^{-1}$. An other (straightforward) limitation is time: even with fast echo-planar imaging techniques, the acquisition of several hundreds of diffusion weighted images (see Fig. 4.6), necessary in DSI, can take up to one hour, which is not compatible with clinical use. Finally, the acquisition and reconstruction on a Cartesian lattice has some computational advantages, but when one wants to compute the orientation distribution function (ODF), only numerical methods apply, and it is necessary to interpolate the EAP to compute the radial integrations.

4.2.2 Model-based reconstruction

To overcome limitations of DSI, which is a model-free, direct reconstruction technique, several assumptions on the nature of the diffusion EAP have been made to

simplify the problem. We present in this section the most popular approach, called diffusion tensor imaging (DTI) [Basser et al., 1994a,b], as well as other related approaches.

Diffusion Tensor Imaging

The DTI technique assumes that the water molecules displacement has a multivariate Gaussian probability (see Section 3.4.1). Within this framework, the EAP is fully described by the so-called diffusion tensor, $\mathbf{D}$, which is a 3×3 symmetric, positive matrix. The Fourier transform relating the signal attenuation to the propagator (Eq. 4.3) reduces to the simple Stejskal-Tanner equation [Stejskal and Tanner, 1965],

$$E(\mathbf{q}) = \exp(-\mathbf{q}^{\mathrm{T}}\mathbf{D}\mathbf{q}). \tag{4.4}$$

Mathematically, the diffusion tensor is parameterized by its 6 independent coefficients. Given measurements of the diffusion signal attenuation in at least 6 independent positions in the q-space, the diffusion tensor can be estimated. Several techniques have been proposed in the literature for the estimation of the diffusion tensor. We describe below the first method originally proposed [Basser et al., 1994a], based on linear least squares.

Linear Least Squares The Eq. 4.4 can be linearized, and rewrites

$$-\log(E(\mathbf{q})) = \mathbf{q}^{\mathrm{T}}\mathbf{D}\mathbf{q}. \tag{4.5}$$

Put in matrix form, given K measurements $y_k = -\log(E(\mathbf{q}_k))$, this is a classical linear system

$$\mathbf{y} = \mathbf{H}\mathbf{d}, \tag{4.6}$$

where $\mathbf{H}$ is the corresponding observation matrix, and $\mathbf{d}$ is the vector of coefficients $\mathbf{d} = [D_{\mathrm{xx}} D_{\mathrm{yy}} D_{\mathrm{zz}} D_{\mathrm{xy}} D_{\mathrm{xz}} D_{\mathrm{yz}}]^{\mathrm{T}}$.

Since then, the 6 parameters of the diffusion tensor can be reconstructed by linear least squares [Basser et al., 1994a],

$$\hat{\mathbf{d}} = (\mathbf{H}^{\mathrm{T}}\boldsymbol{\Sigma}^{-1}\mathbf{H})^{-1}\mathbf{H}^{\mathrm{T}}\boldsymbol{\Sigma}^{-1}\mathbf{y}, \tag{4.7}$$

where Σ is the diagonal matrix with entries $\Sigma_{k,k} = \sigma_k^2 / S(\mathbf{q}_k)^2$. It accounts for the non-linear transform of Eq. 4.5, through first-order noise propagation. Under this model of additive, Gaussian noise, this estimator is the unbiased estimator of minimum variance [Kay, 1993].

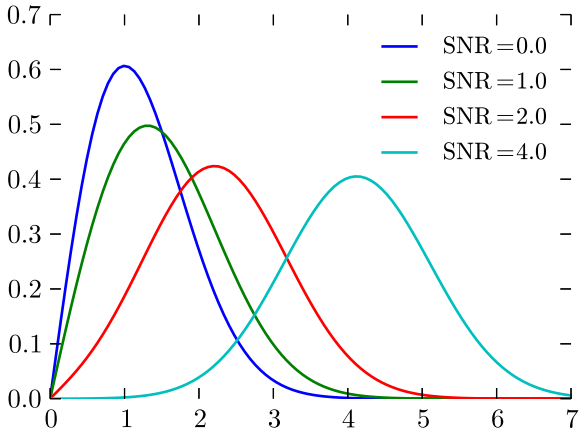

Figure 4.7: Rice distribution probability density function, for several values of the SNR. At low SNR, the Rice distribution is not symmetric, and the noise adds a positive shift to the signal. Estimation not taking into account this shift would result into inevitable bias.

Noise model and non-linear estimation Beyond the simple linear least squares, we could directly solve the non-linear least-squares version of Eq. 4.4. The rational behind this method is that the least-squares solution is the maximum-likelihood estimator, under the assumption that the measurements are corrupted by Gaussian noise. For sufficiently large signal-to noise ratio (SNR), this assumption is valid. However, when the SNR falls below 3 or 4, a more adapted noise model is the Rician noise distribution (see Fig. 4.7) [Sijbers et al., 1998, Sijbers, 1998].

Several methods were proposed to cope with this noise model. Some methods [Fillard et al., 2007, Basu et al., 2006, Landman et al., 2007] directly estimate the diffusion tensor, with a data fit term corresponding to the likelihood of the Rician distribution. Other methods propose to filter the diffusion weighted images prior to estimation, either to remove Rician noise [Descoteaux et al., 2008] or to transform the noise into a Gaussian, additive noise [Koay et al., 2009b]. These methods are more general are they do not rely on the tensor model for the diffusion signal. This is an active an important topic of research in diffusion MRI, as diffusion weighted images have very low SNR and must be processed carefully.

Positivity constraint In diffusion tensor MRI, the object of interest is the diffusion tensor. As it is proportional to the covariance matrix of the EAP, the estimated tensor should be positive-definite. Several methods were proposed to this end, such as the log-Euclidean metrics [Fillard et al., 2007], the Riemannian framework [Lenglet, 2006], or specific parameterizations [Landman et al., 2007].

Extensions to the Gaussian model

The Gaussian diffusion model is limited to describe the diffusion for a single preferred orientation, and cannot accurately describe configurations with several populations of fibers in a same voxel. Several groups have proposed to extend the diffusion tensor model to better describe these configurations. Alexander et al. [2002] propose a multi-tensor model, which is estimated in place of the diffusion tensor whenever a significant distance to the Gaussian model is detected. Other groups proposed to use higher order tensors to represent the diffusivity [Özarslan and Mareci, 2003], leading to a generalization of DTI. Jian et al. [2007] propose to model the diffusion as a mixture of Wishart distributions.

Beyond these extensions to the diffusion tensor model, several studies have been carried out to represent the diffusion signal, independently of a physical model of diffusion. A tour of these methods is presented in the next section.

4.2.3 Model-free reconstruction methods

Several methods reconstruct the diffusion signal in a model-independent fashion, and use the fundamental Fourier relation of Eq. 4.3 to reconstruct either the orientation distribution function, or the full ensemble average propagator. We present the methods that require samples on a shell (or q-ball) in the q-space, and methods that do not rely on a specific acquisition scheme.

q-ball imaging

q-ball imaging is a technique proposed in Tuch [2004a] to reconstruct the orientation distribution function ψ_{T}. We recall (see Section 3.4.2) that the orientation distribution function is defined as

$$\psi_{\mathrm{T}}(\mathbf{u}) = \frac{1}{Z}\int_0^\infty P(r\cdot\mathbf{u})\mathrm{d}r. \tag{4.8}$$

The work in Tuch [2004a] shows that the ODF ψ_{T} can be approximated by the Funk-Radon transform of the diffusion signal E restricted to a sphere of radius q_0. Formally,

$$\psi_{\mathrm{T}}(\mathbf{u}) \approx \frac{1}{Z}\int E(\mathbf{q})\delta(\mathbf{q}^{\mathrm{T}}\mathbf{u})\delta(||\mathbf{q}|| - q_0)\mathrm{d}\mathbf{q}, \tag{4.9}$$

where Z is a normalization constant.

Summary of advantages and limitations q-ball method

+ Reconstructs the ODF ψ_{T} from samples on a q-shell, instead of complete q-space (as in DSI),

+ Model-free method,

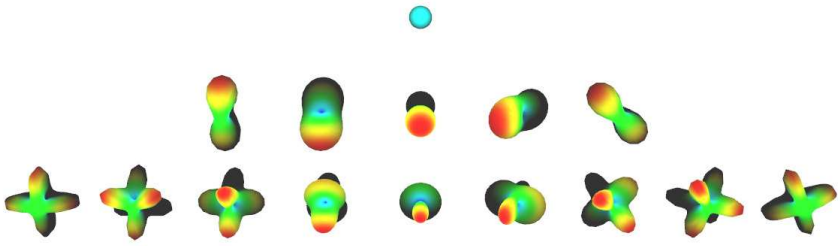

Figure 4.8: The spherical harmonic basis functions. Each line corresponds to orders $\ell = 0, 2, 4$. The parameter m ranges from $-\ell$ to ℓ.

– Discrete method, requires inefficient numerical Funk-Radon transform,

– Reconstructs the ODF ψ_{T}, not the marginal ODF ψ.

Analytical q-ball imaging The q-ball imaging technique [Tuch, 2004a] has been improved, with the use of spherical harmonics functions to represent the signal [Anderson, 2005, Hess et al., 2006, Descoteaux et al., 2007b]. The computation of the Funk-Radon transform in Eq. 4.9 in the spherical harmonic basis is analytical, therefore the computational cost in computing the ODF is reduced. Besides, this also provides a convenient way to regularize the signal on the sphere through the Laplace-Beltrami operator [Descoteaux et al., 2007b]. This regularization, minimizing the penalization $\int_{\mathcal{S}^2}(\nabla_{\mathrm{b}} E)^2$, acts as a low-pass filter and removes oscillations due to noise.

The signal $E(q_0 \cdot \mathbf{u})$ is approximated by the spherical harmonics basis, truncated to order L,

$$\forall \mathbf{u} \in \mathcal{S}^2, \qquad E(q_0 \cdot \mathbf{u}) = \sum_{\ell=0}^{L} \sum_{m=-\ell}^{\ell} c_{\ell,m} Y_{\ell,m}(\mathbf{u}). \tag{4.10}$$

The diffusion signal, E, is antipodally symmetric, and real as we generally measure the signal amplitude. Usually, we use a modified spherical harmonic basis, adapted to real, symmetric functions [Descoteaux et al., 2007b]. These functions are depicted on Fig. 4.8, for a truncation degree $L = 4$.

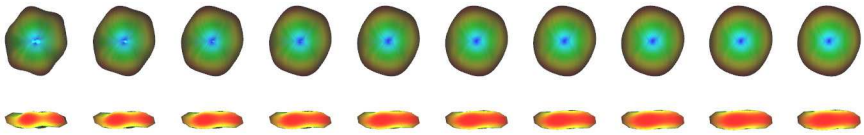

Figure 4.9: Effect of Laplace-Beltrami regularization for the estimation of a q-ball signal, in the spherical harmonic basis (single fiber, $b = 3000\,\mathrm{s}\cdot\mathrm{mm}^{-1}$, SNR = 20, $K = 30$ measurements). (top) top view, (bottom) side view. From left to right: λ weighting parameter increasing, from 0.0 to 0.01.

The mathematical expression of the spherical harmonics function is

$$Y_{\ell,m}(\vartheta,\varphi) = \begin{cases} \sqrt{\dfrac{2(2\ell+1)(\ell-m)!}{(\ell+m)!}} P_\ell^m(\cos\vartheta)\cos(m\varphi) & \text{for } m<0 \\ \sqrt{(2\ell+1)} P_\ell^m(\cos\vartheta) & \text{for } m=0 \\ \sqrt{\dfrac{2(2\ell+1)(\ell-m)!}{(\ell+m)!}} P_\ell^m(\cos\vartheta)\sin(m\varphi) & \text{for } m>0 \end{cases}$$

When truncated up to order L, this SH basis has dimension $R = (L+1)\cdot(L+2)/2$. To ease matrix representation, we introduce a single index j to designate the spherical harmonic function $Y_j = Y_{\ell,m}$ [Descoteaux et al., 2006]. The correspondence is given by $j = 1, 2, \ldots, R$ when $(\ell, m) = (0,0), (2,-2), (2,-1), \ldots, (2,2), \ldots, (L,-L), \ldots, (L,L)$ respectively.

The coefficients c_j of the signal in spherical harmonic basis are estimated from a series of measurements at points $q_0 \cdot \mathbf{u}_k$, minimizing

$$U(\mathbf{c}) = ||\mathbf{y} - \mathbf{B}\mathbf{c}||^2 + \lambda \mathbf{c}^{\mathrm{T}}\mathbf{L}\mathbf{c}, \tag{4.11}$$

where $\mathbf{B}$ is the spherical harmonics design matrix ($B_{k,j} = Y_j(\mathbf{u}_k)$), $\mathbf{y}$ is the vector of observations ($y_k = E(q_0 \cdot \mathbf{u}_k)$) and $\mathbf{c}$ is the vector of spherical harmonic coefficients. The matrix $\mathbf{L}$ is the Laplace-Beltrami operator in the spherical harmonic basis, and is diagonal, since the spherical harmonics are eigenfunctions of ∇_{b}. The entries of this matrix are $L_{j,j} = \ell^2 \cdot (\ell+1)^2$. The effect of Laplace-Beltrami regularization is visible on Fig. 4.9. In particular, the choice of the weighting parameter λ is critical, and should be adapted on a per-voxel basis, as studied in Descoteaux et al. [2010].

From the coefficients $\mathbf{c}$, describing the signal, the coefficients that represent the ODF ψ_{T} are $\mathbf{c}' = \mathbf{P}\mathbf{c}$, where $\mathbf{P}$ is the Funk-Radon operator in the spherical harmonics basis. $\mathbf{P}$ is a diagonal matrix, with entries $2\pi P_\ell(0)$, the Legendre polynomial of degree ℓ evaluated at 0.

The ODF (as well as the EAP) are probability density functions, so they are positive-valued. By analogy to the tools developed to constrain the tensor estimation on the Riemannian manifold of positive matrices, some work have been proposed recently to propose a similar framework for the ODF and the EAP [Cheng et al., 2009, Goh et al., 2011].

Summary of advantages and limitations analytical ODF in q-ball method

+ Fast estimation of the q-ball signal and ODF ψ_{T},
+ Laplace-Beltrami improves robustness to noise,
− Reconstructs the ODF ψ_{T}, not the marginal ODF ψ.

Real-time ODF computation The acquisition in high angular resolution diffusion imaging is quite demanding, and the scan time can become an issue. It might be interesting to get an online feedback on the quality of the reconstruction, to take decision accordingly in case of patient discomfort or patient motion. In that sense, an incremental reconstruction of the ODF has been proposed [Poupon et al., 2008b, Deriche et al., 2009]. The solution is based on a Kalman filter, and exploits the analytical joint estimation and regularization of the ODF [Descoteaux et al., 2006], which involves only linear operations.

The reconstruction method in Deriche et al. [2009] implements an incremental minimization of the energy in Eq. 4.11. The resulting Kalman filter is given by the following system of equations,

$$\text{Initialization} \quad \begin{cases} \mathbf{c}[0] &= \mathbb{E}[\mathbf{c}] \\ \tilde{\mathbf{P}}[0] &= \mathbb{E}[(\mathbf{c}-\mathbf{c}[0])(\mathbf{c}-\mathbf{c}[0])^{\mathrm{T}}] \\ \mathbf{P}[0] &= (\tilde{\mathbf{P}}[0]^{-1}+\lambda\mathbf{L})^{-1} \end{cases}$$

$$\text{Update} \quad \begin{cases} V[k] &= \mathbf{B}[k]\mathbf{P}[k-1]\mathbf{B}[k]^{\mathrm{T}}+\sigma^2[k] \\ \mathbf{g}[k] &= \mathbf{P}[k-1]\mathbf{B}[k]^{\mathrm{T}}V[k]^{-1} \\ \mathbf{P}[k] &= (\mathbf{I}-\mathbf{g}[k]\mathbf{B}[k])\,\mathbf{P}[k-1] \\ \gamma[k] &= y[k]-\mathbf{B}[k]\mathbf{c}[k-1] \\ \mathbf{c}[k] &= \mathbf{c}[k-1]+\mathbf{g}[k]\gamma[k] \end{cases} \tag{4.12}$$

As it is usually the case in discrete-time systems, the time index k is in square brackets rather than subscript, which would have made the notations confusing. The matrix $\mathbf{P}[k]$ is the estimate covariance, while the vector $\mathbf{c}[k]$ is the current estimate. The vector $\mathbf{g}[k]$ is usually referred to as the Kalman gain, while $\gamma[k]$ is the residual, or prediction error.

Summary of advantages and limitations of real-time ODF method

+ Fast estimation of the q-ball signal compatible with real-time processing,
+ Incremental solution matches the exact, off-line, reconstruction,
– Reconstructs the ODF ψ_{T}, not the marginal ODF ψ.

Marginal ODF in q-ball imaging As explained in Section 3.4.2, there are two concurrent definitions of the orientation distribution function. While Tuch originally proposed a solution to reconstruct the ODF ψ_{T} in q-ball imaging [Tuch, 2004a], it was recently shown that the marginal ODF, also known as the ODF in constant solid angle, could be reconstructed in q-ball imaging [Tristán-Vega et al., 2009, Aganj et al., 2010b].

Under the assumption of a mono-exponential decay of the diffusion signal E, the relation between $E(\mathbf{q})$, and the ODF ψ is given by:

$$\psi(\mathbf{u}) = \frac{1}{4\pi} + \frac{1}{16\pi^2}\mathrm{FRT}\left\{\nabla_b^2 \ln(-\ln E)\right\}(\mathbf{u}), \tag{4.13}$$

where FRT denotes the Funk-Radon Transform, and ∇_b^2 the Laplace-Beltrami operator Aganj et al. [2010b].

The work in Aganj et al. [2010b] also proposes to extend the reconstruction to acquisition on several concentric spheres in the q-space. This kind of acquisition is sometimes referred to as multiple q-shell imaging. This introduces the next section, in which we present general methods to reconstruct the signal, independently of a given acquisition protocol.

Summary of advantages and limitations of marginal ODF in q-ball imaging

+ Analytical reconstruction of the signal, and the ODF,
– Assumes a mono-exponential (single shell) or multi-exponential decay,
– Multi-shell sampling requires same number and sampling directions on each shell.

Continuous q-space imaging

We denote by continuous q-space imaging the techniques working with a continuous representation of the signal E, and implement a continuous Fourier transform to compute the EAP. We retain in this section only the model-free methods. The advantage of these methods is their generality as they assume no underlying physical model of diffusion. Besides, these methods usually do not rely on a specific acquisition strategy in the q-space. Several bases have been proposed to this end, together with methods to reconstruct the EAP and the ODF.

Diffusion propagator imaging An extension of the spherical harmonic basis to the 3D space is the Laplace equation by part, as proposed in Descoteaux et al. [2011]. The signal is decomposed as follows,

$$E(q \cdot \mathbf{u}) = \sum_{\ell,m} \left[\frac{c_{\ell,m}}{q^{\ell+1}} + d_{\ell,m} q^{\ell} \right] Y_{\ell,m}(\mathbf{u}), \tag{4.14}$$

where $Y_{l,m}$ is the real, spherical harmonic function introduced above. From this decomposition, the authors in Descoteaux et al. [2011] provide analytical formulae for the EAP, the ODF and the return-to-origin probability. Yet, the choice of the representation in Eq. 4.14 suffers from several drawbacks.

First, the signal reconstructed in this basis cannot be represented about zero, due to the denominator $q^{\ell+1}$. Besides, the behaviour for large q also is incompatible with what is observed generally ($E \to 0$ when $q \to \infty$). Therefore, the approximation is valid only in the range $[q_{\min}, q_{\max}]$, which is the volume comprised within the innermost and outermost shells. In particular, there is no chance to extrapolate the signal on the whole q-space. The Fourier transform in turn must be computed on the same cropped volume, and this can introduce inaccuracies in the estimation of the EAP. Other bases have been proposed, with a different radial profile, compatible with signal extrapolation.

Summary of advantages and limitations of DPI

\+ Model-free method,

\+ Analytical reconstruction of the signal, the EAP and the ODF

– No regularization provided,

– Basis functions not adapted to extrapolate the signal to the whole q-space.

Simple harmonic oscillator The simple harmonic oscillator-based estimation and reconstruction (SHORE) has originally been proposed for the reconstruction of one dimensional q-space diffusion signal [Ozarslan et al., 2008]. Given a direction $\mathbf{u}_0$ in the q-space, the signal is decomposed in a basis of polynomial functions, weighted by a Gaussian kernel. Formally, we have $E(q \cdot \mathbf{u}_0) = \sum_n a_n \Phi_n(q)$, with the basis function

$$\Phi_n(q) = \kappa_n(u) \exp(-2\pi^2 q^2 u^2) L_n^{-1/2}(4\pi^2 q^2 u^2), \tag{4.15}$$

where u is a characteristic length, $L_n^{-1/2}$ the generalized Laguerre polynomial of degree n chosen for orthogonality, and $\kappa_n(u)$ a normalization constant,

$$\kappa_n(u) = \sqrt{\frac{4\pi u n!}{\Gamma(n + 1/2)}}. \tag{4.16}$$

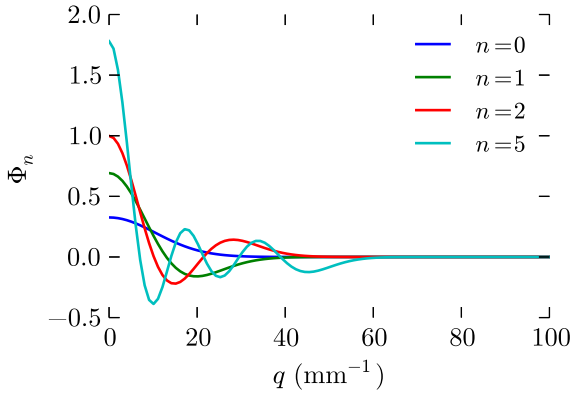

Figure 4.10: SHORE 1D basis functions, for $n = 0, 1, 2, 5$. The characteristic length is set to $u = 15$ µm.

We plot several basis functions on Fig. 4.10. In particular, these functions behave well when $q \to \infty$. Besides, this basis was designed to capture non-monotonic radial decay, as it is the case in most restricted geometries [Özarslan et al., 2011].

This radial profile was further extended to represent the 3D signal [Ozarslan et al., 2009], by using the spherical harmonics to capture angular information. The basis functions in 3D are therefore

$$\Phi_{n,\ell,m}(q \cdot \mathbf{u}) = \kappa_{n,\ell}(u) \exp(-2\pi^2 q^2 u^2) q^\ell L_{n-1}^{\ell+1/2}(2\pi^2 q^2 u^2) Y_{\ell,m}(\mathbf{u}). \tag{4.17}$$

The original method did not explicitly provide analytical formulations for the EAP and the ODF. They are however derived in Cheng et al. [2011].

Summary of advantages and limitations of SHORE

+ Model-free,
+ Analytical reconstruction of the signal,
− No regularization provided,
− No method to take into account $E(\mathbf{0}) = 1$.

Spherical Polar Fourier basis In parallel to the work of Ozarslan et al., a related basis has been proposed, called the spherical polar Fourier basis (SPF) [Assemlal et al., 2009b]. This is an orthonormal basis, whose functions are defined as the product of a radial and an angular function. The signal is decomposed as a sum of functions: $E(q) = \sum_{n,\ell,m} a_{n,\ell,m} B_{n,l,m}(\mathbf{q})$, where

$$B_{n,l,m}(q \cdot \mathbf{u}) = R_n(q) Y_{\ell,m}(\mathbf{u}), \text{ and } R_n(q) = \kappa_n(\zeta) e^{-q^2/2\zeta} L_n^{1/2}\left(\frac{q^2}{\zeta}\right). \tag{4.18}$$

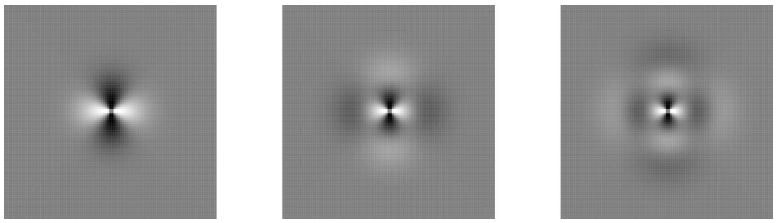

Figure 4.11: SPF functions $B_{n,2,-2}$, $n = 0, 1, 2$ (from left to right), plotted on the plane $z = 0$. Strong discontinuities about the origin are visible.

The work has been further extended to provide a dual SPF basis (dSPF) to represent the EAP with the same coefficients [Cheng et al., 2010b], as well as close-form formulae for the computation of the ODF ψ_{T} and the marginal ODF ψ [Cheng et al., 2010a]. The SHORE basis we previously reviewed and the SPF basis are familiar, yet show some differences. In particular, for the same radial truncation order N, the SHORE basis will span a subspace of that spanned by the SPF basis.

We point out a drawback of SPF basis functions: as reported on Fig. 4.11, the functions $B_{n,\ell,m}$ are discontinuous about $\mathbf{0}$. While both the Laguerre polynomial and the spherical harmonics are continuous functions on their respective domains, the problem comes from the parameterization $\mathbf{q} = q \cdot \mathbf{u}$. Indeed, the unit vector $\mathbf{u}$ is not uniquely defined about the origin, and care must be taken when this parameterization is used.

The SPF reconstruction method was proposed together with a regularization, to increase the stability of the reconstruction in presence of noise [Assemlal et al., 2009b]. The regularization acts directly on the coefficients, and the problem solved is a penalized least squares,

$$U(\mathbf{a}) = ||\mathbf{y} - \mathbf{H}\mathbf{a}||^2 + \lambda_L \mathbf{a}^{\mathrm{T}}\mathbf{L}\mathbf{a} + \lambda_N \mathbf{a}^{\mathrm{T}}\mathbf{N}\mathbf{a}, \tag{4.19}$$

where $\mathbf{y} = [E(\mathbf{q}_1), \ldots, E(\mathbf{q}_K)]$ is the vector of measurements, $\mathbf{H}$ the matrix of observation in the SPF basis and $\mathbf{a}$ the vector of coefficients $a_{n,\ell,m}$. The regularization matrices $\mathbf{L}$ and $\mathbf{N}$ are diagonal matrices, with weights $\ell^2(\ell+1)^2$ and $n^2(n+1)^2$, which are supposed to act as angular and radial low-pass filters, respectively.

Summary of advantages and limitations of SPF method

+ Model-free method,

+ Analytical reconstruction of the signal (least squares estimate),

+ Analytical computation of EAP and ODF,

− Discontinuity about the origin,

- No method to take into account $E(\mathbf{0}) = 1$,
- Low-pass filters $\mathbf{L}$ and $\mathbf{N}$ defined empirically.

4.3 Summary of the chapter

We have presented a tour of reconstruction method in diffusion MRI, from the diffusion signal in q-space to the reconstruction of diffusion characteristics. Several challenges were presented throughout the chapter, in particular the practical limitations in clinical settings, where the subjects are likely to move and can sometimes difficulty remain still in the scanner for dozens of minutes. The works on incremental reconstruction [Poupon et al., 2008b, Deriche et al., 2009] provide an answer by giving a real-time feedback on the reconstruction accuracy. We present in Chapter 7 of this thesis an extension to this work for the reconstruction of the ODF in constant solid angle, and the application to motion detection.

Besides, there is a growing interest for the development of techniques that permit the reconstruction of the full ensemble average propagator. In this domain, the SPF basis is a promising tool for the reconstruction of the signal in the whole q-space, and the subsequent estimation of EAP and ODF. However, we have highlighted some mathematical problems in the SPF basis, related to the continuity at the origin, and the regularization proposed in Assemlal et al. [2009b]. We present in Chapter 6 of this thesis a method for the reconstruction of a continuous signal, with a classical Laplace regularization.

Chapter 5

Acquisition strategy in q-space

Contents

Overview

Given the opportunity to acquire K samples in the q-space, how to arrange the points for an accurate reconstruction? What is the best strategy in q-ball imaging? We introduce the main methods and strategies for the acquisition of diffusion signal. Throughout this chapter, we also introduce some important open questions and challenges, some of which we address in this thesis.

Keywords pulse gradient spin echo; diffusion gradient; orthogonal bases; q-ball imaging; q-space sampling.

5.1 Introduction

We have presented in the last chapter a guided tour of model-free reconstruction methods in q-ball and q-space imaging. For all these methods, a constant is the estimation of the signal, from discrete samples. The sampling strategy is critical in diffusion MRI and applications, as the number of acquisitions is limited by the scan time. Indeed, the acquisition one sample in the q-space corresponds to the acquisition and reconstruction of the whole volume to be imaged, as illustrated on Fig. 4.6. In this section, we present a list of the state-of-the-art sampling strategies developed in diffusion MRI. We first present sampling on the sphere in diffusion MRI, referred to as q-ball imaging. Then we study the extensions to multiple shells and beyond.

5.2 Acquisition in q-ball imaging

To introduce this section on acquisition on the sphere, we state three fundamental requirements for the sampling in q-ball imaging. These are basic principles which are helpful to compare state-of-the-art methods.

Antipodal symmetry Although the diffusion propagator P is not necessarily symmetric, the diffusion attenuation signal measured in q-space is symmetric. Therefore it is equivalent to measure $E(\mathbf{q})$ and $E(-\mathbf{q})$, and this symmetry needs consideration to elaborate the sampling protocol.

As isotropic as possible Usually, there is no prior in the underlying tissue consideration, and it is important to sample each direction equivalently. This is to avoid any bias, introduced by a sampling with non isotropic density.

Information gathering and noise performance The signal is reconstructed from discrete samples, in order to finally estimate the diffusion tensor, the

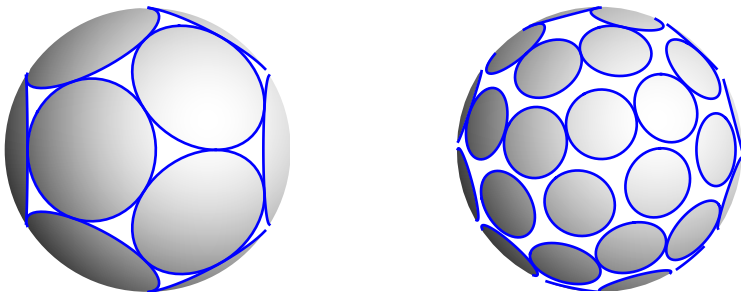

Figure 5.1: Spherical caps packing, (left) for $K = 12$ the Fejes-Tóth bound is achieved: the centers of the spherical caps are the vertices of an inscribed icosahedron; (right) for $K = 40$, suboptimal configuration provided by the electrostatic energy minimization, as in Jones et al. [1999a].

EAP or the ODF. For a given number of measurements, the sampling strategy should maximize the amount of information collected to reconstruct the quantity of interest with best accuracy.

5.2.1 Geometrical constructions

The two above-mentioned properties have motivated the construction of sampling scheme on a purely geometrical basis. We give a review of such in q-ball imaging.

Spherical caps packing

The problem of finding an arrangement of points "evenly" distributed on the surface of a sphere has a long history. One of the parameter of interest is the distance between any two points, and in particular the minimum distance between any two points.

Definition 1. *Given a set of points* $\mathbf{u}_k, k = 1 \dots K$ *on the sphere, we call the* radius *of this sequence the minimum distance* d *between any two points*

$$d = \min_{i \neq j} ||\mathbf{u}_i - \mathbf{u}_j||. \tag{5.1}$$

Maximizing the radius d can be equivalently seen as looking for a packing of non-overlapping spherical caps of maximal radius on the sphere. In 1943, the mathematician Fejes-Tóth showed that an upper bound exists for the radius [Fejes-Tóth, 1943]

$$d \leq \sqrt{4 - \csc^2 \frac{\pi K}{6(K-2)}}. \tag{5.2}$$

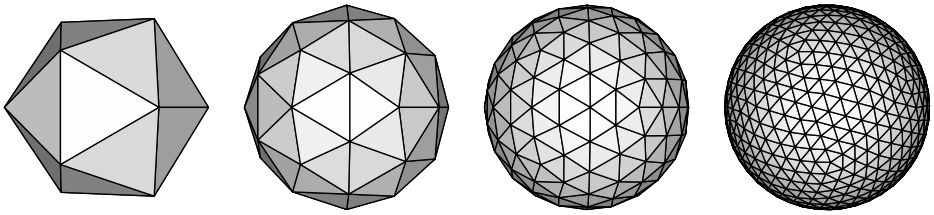

Figure 5.2: Sphere tessellation from an icosahedron. From left to right: regular icosahedron (12 vertices), two-fold tessellated icosahedron (42 vertices), 4-fold tessellated icosahedron (162 vertices) and 8-fold tessellated icosahedron (642 vertices).

For instance for $K = 12$, this bound is sharp and the corresponding set is the inscribed icosahedron, as in Fig. 5.1. However, the general case has not been solved however.

Lines packing

The problem of spherical caps packing is to arrange points evenly on the surface of the sphere. But in diffusion MRI, the measured signal $E(\mathbf{q})$ has antipodal symmetry. Therefore, the problem of uniformly arrange the sampling directions also should take into account this central symmetry. This problem has been extensively studied too, and is known as lines packing in $\mathbb{R}^3$ [Conway et al., 1996]. Surprisingly, and to the best of our knowledge, the results in Conway et al. [1996] have never been used for the design of acquisition schemes in q-ball imaging. We acknowledge the library of such designs at the authors' website.

Sphere tessellation

The tessellation of the sphere from an icosahedron is a geometric construction of a triangular mesh of the sphere. It is useful in numerous applications such as numerical analysis on the sphere [Sadourny et al., 1968], or computer graphics [Snyder and Barr, 1987]. The construction, sketched on Fig. 5.3, consists in starting from a regular polyhedron, usually the icosahedron, and subdivide each triangular face into smaller faces. The new vertices are then projected onto the surface of the sphere. By increasing the number of edge subdivisions d, it is possible to generate large collection of vertices (see Fig. 5.2), spread out on the surface of the unit sphere. The set of vertices of the constructed tessellation is antipodally symmetric, and therefore we can use the half of the points in diffusion MRI acquisition. In q-ball imaging, a five-fold icosahedron has been used [Tuch, 2004a, Descoteaux et al., 2007b] for the acquisition of diffusion attenuated signal.

There are two major drawbacks in this construction: first, it does not allow point set construction of an arbitrary size. Indeed, if the edge of each triangle is

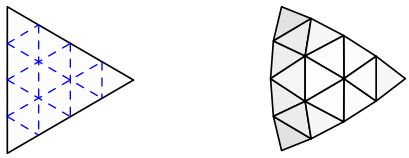

Figure 5.3: Construction of the sphere tessellation, by four-fold subdivision of the edges of a regular icosahedron. (left) The triangular face of the icosahedron is divided into equilateral sub-triangles, (right) the created vertices are back-projected onto the surface of the unit sphere.

Number of segments d	Number of vertices $K(d)$
1	12
2	42
3	92
4	162
5	252
6	362
7	492
8	642

Table 5.1: Number of vertices of a d-fold tessellated icosahedron.

subdivided into d segments, the number of triangles is multiplied by d^2, and the number of resulting vertices $K(d)$ is given in Table 5.1. We can show $K(d) = 12 + 10 \cdot (d^2 - 1)$.

The second drawback is related to the optimality, in terms of distance between two adjacent points. The icosahedron is made of equilateral triangles, and as stated above, it is an optimal configuration for the spherical caps packing problem, that achieves the Fejes-Tóth bound (see Fig. 5.1, left). When it is subdivided (see Fig. 5.3, on the left), the sub-triangles are also equilateral triangles, all with the same dimensions; but when the new vertices are projected back onto the surface of the sphere, the triangles are deformed, and are no-longer equilateral.

Summary of advantages and limitations of sphere tessellation

\+ Geometric construction, with rapid computation of vertex positions,

\+ Antipodal symmetry,

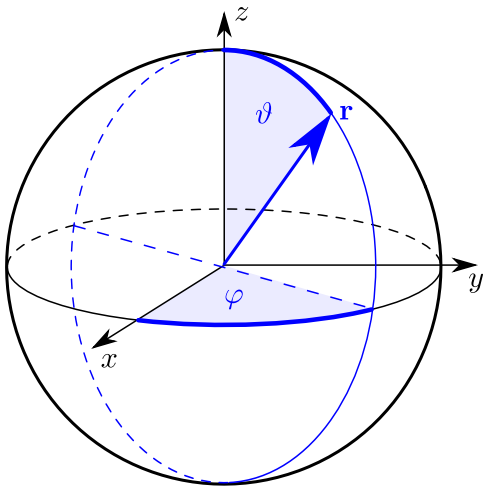

Figure 5.4: The colatitude angle, ϑ, and the longitude angle, φ.

– No means to create such arrangement for an arbitrary number of points,

– No evidence of uniformity.

Circles of latitude

The author in Koay [2011] provide a sampling scheme with nearly uniform density on the sphere. The unit sphere is usually parameterized by colatitude $\vartheta \in [0, \pi]$ and longitude angles $\varphi \in [0, 2\pi]$. Given a point $\mathbf{u}$ on the unit sphere, its Cartesian coordinates are $[\cos(\varphi)\sin(\vartheta)\, \sin(\varphi)\sin(\vartheta)\, \cos(\vartheta)]$, as illustrated on Fig. 5.4. A strategy consisting in creating a sampling scheme from a regular grid in the space of parameters ϑ, φ would provide a poor scheme, with a strong concentration of points about the poles, and a sparse density about the equator. Yet it is possible to arrange the points on circles of latitude (ϑ constant), with a clever choice of the number of discretization steps, and the number of points on each line parallel to the equator (see Fig. 5.5).

The construction in Koay [2011] arranges the points on circles parallel to the equator, determined by a finite number of colatitude angles $\vartheta_i, i = 1 \dots n$. On a given line i, the points are given by their longitudes $\varphi_{i,j}, j = 1 \dots k_i$. The number of discretization steps n for ϑ is chosen so that the angular distance between two consecutive latitude, $\Delta\vartheta$, equals the distance between two consecutive points on the same latitude. Thus up to the choice of rounding functions, the number of latitude circles, n, and the number of points on circle i, k_i, are determined by the equations

$$n = \frac{K}{2} \sin\left(\frac{\pi}{4n}\right) \tag{5.3}$$

$$k_i = 2\sin(\vartheta_i) \sin\left(\frac{\pi}{4n}\right) \tag{5.4}$$

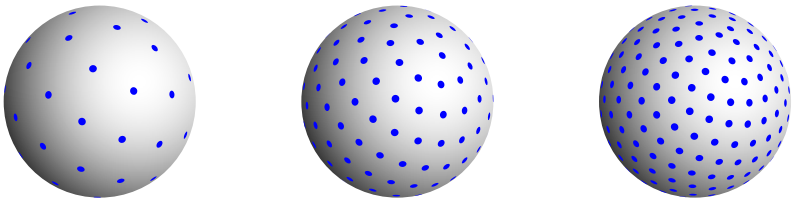

Figure 5.5: Point sets generated following the geometrical construction in Koay [2011]. (from left to right) $K = 25, 75, 125$. The alignment of points on circles of latitude is visible on these pictures.

The method is simple and fast, thus appreciated to generate efficiently sampling protocols with a large number of points (up to $K = 10^5$ reported in the paper). Yet this method does not optimize directly the angular distance between adjacent points in general. Only the angular distance between points on a same latitude line, and the angular distance between the supporting lines are considered, and this might result in a suboptimal configuration. As reported by the author, this method is best suited to large number of points and was designed with a primary focus on computational efficiency.

Summary of advantages and limitations of sampling on circles of latitude

+ Analytical geometric construction, with rapid computation of vertex positions,
+ Antipodal symmetry,
+ Construction for any number of points K,
+ Implemented in a free software, downloaded from the author's website,
− Not best suited for small sample size $K < 50$,
− No evidence of uniformity.

Electrostatic repulsion

To construct a collection of K points evenly distributed on a sphere, one method is to consider the points as electrostatic charges, repulsing each other, and to find the configuration of minimal energy. This problem is called the Thomson problem, after the physicist who originally studied this problem in his atom model [Thomson, 1904]. As the original formulation does not take into account the antipodal symmetry of diffusion attenuation signal, a slightly modified version of the energy was proposed in Jones et al. [1999a], Jansons and Alexander [2003] for use in diffusion MRI.

Specifically, a set of K points $\mathbf{u}_k$ is optimal if it minimizes the energy

$$\sum_{i \neq j} \frac{1}{||\mathbf{u}_i - \mathbf{u}_j||^2} + \frac{1}{||\mathbf{u}_i + \mathbf{u}_j||^2}. \tag{5.5}$$

Minimum-energy configurations are available in the distribution of the Camino toolkit [Cook et al., 2006], up to $K = 256$ (see Fig. 5.6). One of the drawback is that for a given K, there is no evidence that the minimum energy configuration has maximum radius, as shown on Fig. 5.1.

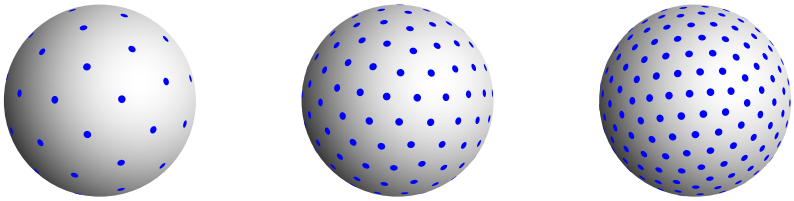

Figure 5.6: Point sets minimizing the electrostatic repulsion energy [Jones et al., 1999a, Jansons and Alexander, 2003]. (from left to right) $K = 25, 75, 125$.

Summary of advantages and limitations of electrostatic repulsion

+ Antipodal symmetry,

+ Construction for any number of points K,

+ Minimal energy configurations in the open-source Camino toolkit [Cook et al., 2006] for $K \leq 256$,

– The energy minimization can take some time for large K,

– No evidence on uniformity.

Power-law repulsion

As a generalization of the electrostatic physical analogy, the power law of the repulsion energy can be increased from r^{-2} to r^{-n}, and to the limit $n \to \infty$ [Papadakis et al., 2000]. Minimal configurations for this energy are supposedly more uniform, as this problem for $n \to \infty$ is equivalent to the Fejes-Tóth problem introduced above, which consists in finding K non-overlapping spherical caps of maximum radius on a sphere [Tammes, 1930]. The minimization of this energy as n increases becomes harder however, as a little change in the points configuration results in a big change in the energy.

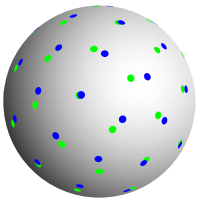

Figure 5.7: (blue) Point sets minimizing the power-law r^{-n} repulsion, and (green) minimizer of the electrostatic energy, used as initialization for the minimization of power-law repulsion. $K = 25$ points, convergence obtained for $n = 28$.

We implemented this method, minimizin the cost function

$$U_n = \left(\sum_{i \neq j} \frac{1}{||\mathbf{u}_i - \mathbf{u}_j||^n} + \frac{1}{||\mathbf{u}_i + \mathbf{u}_j||^n} \right)^{1/n} . \tag{5.6}$$

As suggested in Papadakis et al. [2000], the minimizer of U_n is taken as original guess for U_{n+1}, and n is increased until no significant change is reported. Solutions for $K = 25$ and $K = 75$ are plotted on Fig. 5.7.

Summary of advantages and limitations of power-law repulsion

+ When $n \to \infty$, equivalent to the spherical caps packing problem,
+ Antipodal symmetry,
+ Construction for any number of points K,
− Minimization numerically unstable as n increases,
− Cost function takes some time to minimize as K increases.

Comparison of geometrical methods

All the geometrical methods we have presented so far are designed with the objective to uniformly arrange points on the sphere, with central symmetry. We implemented these techniques, or downloaded optimal point sets for each method. We computed the minimum distance between any two points, which is a good index of the uniformity of the scheme. Intuitively, the further away we can place any two points on a sphere, the better the uniformity of the sampling scheme. Results for sample size K from 6 to 100 are reported on Fig. 5.8. The method that gives best results is the lines packing method [Conway et al., 1996]. We do not report the results of Papadakis et al. [2000], as we were unable to properly minimize the energy they propose.

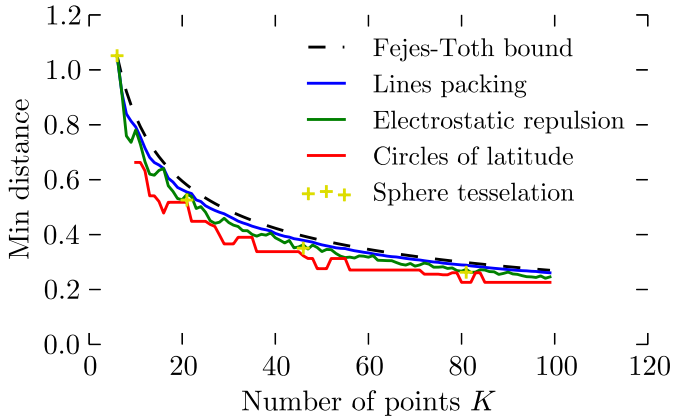

Figure 5.8: Comparison of the minimum distance between any two points for several geometric methods. The method that give results closest to the Fejes-Tóth bound is the lines packing method [Conway et al., 1996].

5.2.2 Incremental acquisition

As seen several times in this thesis, the acquisition time can become long in diffusion MRI. In a clinical scenario, the subject may feel uncomfortable, and request to abort the scan before completion. If the diffusion encoding gradient sequence is not properly arranged, the scanner operator might be unable to recover accurate diffusion characteristics (diffusion tensor, ODF or EAP) from the aborted scan. This issue has been addressed by several groups in research, for the design of q-ball imaging sequence.

Optimal orientation of partial subsets

The method proposed in Dubois et al. [2005] minimizes the sum of energy interaction, $E_{i,j}$, between any two points i and j, weighted by a factor $\alpha_{i,j}$. The weights are designed so that the repulsion of orientations corresponding to acquisitions adjacent in time is higher than the repulsion energy of two acquisitions separated in time. They propose in particular to design the weights $\alpha_{i,j}$ so that some subsets of a given number of acquisition (6 and 15 in their examples) are created. The authors provide two scenarios, with different formulae for the weights.

We believe that the difference between the extremal values of $\alpha_{i,j}$ will reflect how different from the isotropic case the created orientation set will be. However, this trade-off between general uniformity and the uniformity of each subset is not investigated. Besides, choosing the size of the subsets might depend on the application. This work brings a new method to the community, but at the end of the article, the reader is left with several unknowns, which makes it difficult to reproduce.

Summary of advantages and limitations of partial uniform subsets method

+ Compatible with corrupted data to some extent,
+ A generalization of electrostatic repulsion,
+ Construction for any number of points K,
+ Construction for subsets with any size S,
– No general method to design the weights $\alpha_{i,j}$,
– Trade-off between uniformity of partial sets and uniformity of the sequence as a whole to be investigated.

Optimal ordering of diffusion-weighted measurements

In a different approach, Cook et al. [2007] propose a method to find the best ordering of a sequence of acquisition gradient directions, so that any truncated version of this sequence offers a quasi-optimal, uniform coverage of the sphere. Given a set of acquisition directions $\mathbf{u}_k, k = 1 \dots K$, this method seeks the best arrangement of indices k_i, $i = 1 \dots K$, so that the following energy is minimized

$$E_{\text{Cook}}(k_1, \dots k_K) = \sum_{P=6}^{K} E(\mathbf{u}_{k_1}, \dots, \mathbf{u}_{k_P})/P^2. \tag{5.7}$$

The above energy is the sum of electrostatic energy of all the partial subsets of P points, for $6 \leq P \leq K$, weighted by $1/P^2$.

This method was reported to give similar results, compared to Dubois et al. [2005]. The discrete minimization problem associated to this method is hard to solve however, and has a complexity growing with $K!$. Hence Cook et al. [2007] use the simulated annealing minimization method to solve their problem.

Summary of advantages and limitations of partial uniform subsets method

+ Acquisition ordering compatible with corrupted data,
+ If the scan is completed, no difference with optimal acquisition,
+ Optimization implemented in the Camino open-source toolkit [Cook et al., 2006],
– Problem hard to minimize,
– The total number of acquisitions must be known in advance.

Incremental construction of acquisition sequence

The method in Deriche et al. [2009] is dedicated to the construction of acquisition sequence, suited to the reconstruction using Kalman filter. The general algorithm is incremental: given a set of K measurements, it gives a method to find the next, $K+1$-th measurement, and so forth. Formally, the construction of the point set $\{\mathbf{u}_k, k = 1 \dots K\}$ is implemented as in Algorithm 1.

Algorithm 1 Incremental construction of uniform point set, compatible with corrupted acquisition and incremental reconstruction.

1: $\mathbf{u}_1 \leftarrow [0,0,1]^{\mathrm{T}}$
2: **for** $k \in \{2 \dots K\}$ **do**
3: $\quad \mathbf{u}_k \leftarrow \arg\min_{\mathbf{u}\in\mathcal{S}^2} \sum_{j<k} \left(\frac{1}{||\mathbf{u}-\mathbf{u}_j||^2} + \frac{1}{||\mathbf{u}+\mathbf{u}_j||^2} \right)$
4: **end for**

Summary of advantages and limitations of incremental point set construction

+ Acquisition ordering compatible with corrupted data,
+ Simple and efficient scheme for minimization,
+ The total number of measurements K must not be known in advance,
− The construction is slightly suboptimal, even when the scan is complete.

5.2.3 Experimental design for diffusion tensor reconstruction

In place of optimizing the experimental design based on purely geometrical considerations and motivations, several groups have considered the optimization of experimental design for diffusion tensor reconstruction (see Section 4.2.2 for a review of the estimation methods). We present in this section a review of optimization methods for acquisition scheme, taking into account the diffusion tensor estimation.

Acquisition design for minimum variance

The noise performance of the acquisition scheme is studied in Papadakis et al. [1999], through the measure of total variance. This index of noise performance is used to evaluate several schemes, which were designed on the sole basis of 6 non-collinear directions. This index is also used to to generate a new scheme by minimization of this index. The total variance in this work is that of the linear estimate of the diffusion tensor, as in Eq. 4.7. The total variance TV is defined as

$$\mathrm{TV}(\mathbf{u}_1, \dots, \mathbf{u}_k) = \mathrm{tr}(\mathbf{H}^{\mathrm{T}}\mathbf{H})^{-1}, \tag{5.8}$$

where **H** is the observation matrix. It is indeed a measure of the sum of the variances of each tensor element estimate.

This work is important as it is one of the first approach beyond the common non-collinearity requirement, and other geometrical approaches. However, as stated by the authors themselves in Papadakis et al. [1999, 2000], the minimization of this criterion leads to possibly infinitely many solutions, even when congruence by rotation is considered. Therefore, this index can not be used as a unique criterion to generate acquisition point sets.

Summary of advantages and limitations of the total tensor variance criterion

+ A criterion which takes into account the reconstruction,

− This criterion is not suited to optimization to provide new sampling schemes.

Condition number in diffusion tensor estimation

Another measure of interest to evaluate the noise performance of an acquisition scheme is the condition number of the associated observation matrix **H**. The condition number κ is an upper bound for the ratio of the relative error on the measurements, to the relative error on the tensor estimate. This index has been considered in Skare et al. [2000], in this work the authors directly minimize the condition number associated to a set of gradient orientations $\mathbf{u}_k, k = 1 \dots K$, using the downhill simplex method.

This method provides new insights for the design of acquisition schemes, and the approach is validated through Monte-Carlo experiments in Skare et al. [2000]. This study of mostly empirical however, in particular no study of existence and uniqueness of the solution was carried out. However, as K increases, it is likely that several different configurations (beyond trivial congruence by rotation, permutation, symmetries, etc.) will lead to the same condition number.

Summary of advantages and limitations of the condition number minimization

+ A criterion which takes into account the reconstruction,

+ Provides acquisition schemes with lower condition number than conventional schemes,

− No mathematical proof of uniqueness of the solution.

Bayesian experimental design in diffusion tensor imaging

Generally, there is no assumption in experimental design for diffusion tensor imaging. This is the reason why most studies on experimental design use uniform sampling on the sphere, or general approaches on noise performance. Some groups have proposed [Peng and Arfanakis, 2007, Yanasak et al., 2008, Gao et al., 2009] to possibly incorporate a prior on the tensor characteristic, in the design of adapted acquisition sequence. This is most relevant when imaging highly structured regions of interest in the brain, or the spinal cord for instance.

The method in Peng and Arfanakis [2007] seeks a set of orientations to minimize the variance of the estimated tensor fractional anisotropy (FA). The general algorithm for optimization is the downhill simplex, and for each step the variance of the estimated FA is estimated through Monte-Carlo simulations. It is shown that the generated scheme (6 directions in their experiments) leads to a better reconstruction accuracy around the selected, preferred orientation. This is at the cost of a loss of performance to reconstruct diffusion tensors oriented perpendicularly to this selected orientation. It is however not clear that selecting only the FA is relevant for the other quantities of interest in diffusion tensor imaging. In particular, they do not show how the orientation estimation is improved or degraded using this adapted scheme. Another drawback is the cost function, which requires Monte-Carlo to be evaluated. The computational time might become very large, and therefore restrict applications to a larger number of acquisitions $K > 6$.

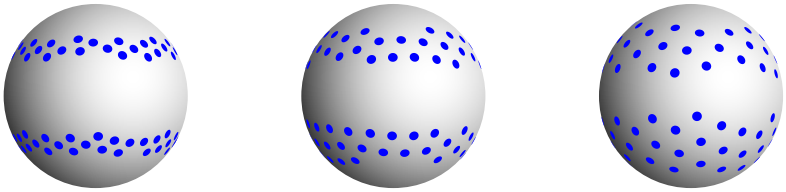

Figure 5.9: Non-uniform gradient directions, adapted to the measurement of a diffusion signal corresponding to a fiber direction along the z axis, as constructed in Yanasak et al. [2008]. (from left to right) dispersion angle $\Delta\vartheta = 10°, 25°$and $40°$.

The method in [Yanasak et al., 2008] seeks a set of gradient directions that maximizes the angular precision in principal tensor orientation estimate. Specifically, given a preferred orientation from the tissue structure of interest, they seek a method that deforms a uniform set of gradient directions, trying to give more importance to the acquisitions "far away" from the preferred direction. More precisely, and without loss of generality, if the preferred orientation is along the z axis, then they arrange gradient directions between two circles of latitude, centered around ϑ_0, and of width $\Delta\vartheta$ (see Fig. 5.9). The intuition it that in this region of the q-ball, the signal has maximum curvature, and also reasonable signal-to-noise ratio.

Therefore the measurements from this portion of the q-ball are supposed to be most informative. They optimize the two parameters ϑ_0 and $\Delta\vartheta$ through Monte-Carlo simulations, to find the best reconstruction accuracy of the tensor orientations. The results show improved angular precision in principal orientation estimation. This method is mainly empirical, and by imposing a specific geometry for the solution, they restrict the set of potentially optimal configurations. Besides, no method is given to uniformly arrange these points within this spherical ring of interest.

The authors in Gao et al. [2009] minimize the trace of the covariance matrix of the tensor parameters estimate, from a linear least squares minimization. They consider a prior as a collection of tensors of interest; in their study only synthetic tensor collections are provided, within a cone of angle 20° or several such cones, and for a maximum of 100 tensors. This criterion is used to optimize both the gradient directions, and other imaging parameters (such as pulse time δ, diffusion time Δ, etc.). We would like to point out an important weakness in their approach: everything is based on the covariance of the non-weighted least squares estimate $\hat{\mathbf{d}} = (\mathbf{H}^{\mathrm{T}}\mathbf{H})^{-1}\mathbf{T}^{\mathrm{T}}\mathbf{y}$, with the same notations as in Section 4.2.2. This is different from the commonly used weighted least squares, as in Eq. 4.7, which accounts for the log-transform of the signal, and indeed is the most commonly used linear method for tensor estimation [Salvador et al., 2005, Basser et al., 1994a], because it is the minimum-variance unbiased estimator [Kay, 1993]. In short, they use a suboptimal estimator with respect to their noise model, and try to find the sampling strategy to optimize the performance of this estimator. The results of their study are therefore hardly reusable.

Summary of advantages and limitations of the Bayesian experimental design in DTI

+ Construction of acquisition scheme adapted to region of interest,
+ Possibility to reduce the number of acquisitions for the same target reconstruction accuracy,
− The scenario of use is not well defined,
− The distribution of tensors of interest is modelled by a set of tensors, which makes the methods computationally inefficient,
− The methods use either empirical constructions, either minimization schemes not compatible with large K, and therefore poorly reproducible.

5.2.4 Harmonic analysis and experimental design

We present in this section so-called sampling theorems on the sphere. Beyond the diffusion tensor imaging technique, the spherical harmonic basis has proved useful

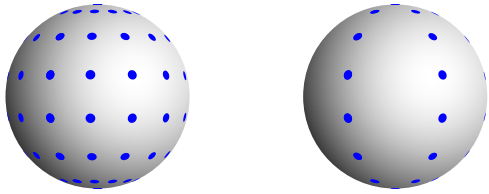

Figure 5.10: Sampling on equiangular grids, for exact reconstruction of band-limited functions at order $L = 4$. (left) the equiangular grid of $K = (2L-1)^2$ samples as in citetdriscoll-healy:94, and (right) the equiangular grid of $K = 2L^2 - 3L + 2$ samples, as in McEwen and Wiaux [2011].

in the study of high angular resolution diffusion imaging, for the reconstruction of the diffusion signal and the ODF. This is the reason why many groups have converged to the use of the spherical harmonic basis in q-ball imaging [Anderson, 2005, Hess et al., 2006, Descoteaux et al., 2006, 2007a], and in many other applications that handle functions and signals on the sphere. The dimension of the modified, real SH basis for functions with antipodal symmetry, truncated to order L is $R = (L+1) \cdot (L+2)/2$. On an algebraic point of view, we need at least R measurements to estimate the spherical harmonic coefficients of a function. A question of interest is that of the minimum number of acquisitions required for an exact reconstruction of a band-limited function in the SH basis.

The SH basis can be seen as the equivalent to Fourier analysis on the sphere. Recent studies [Shukowsky, 1986, Driscoll and Healy, 1994, McEwen and Wiaux, 2011] have emerged, providing sampling theorem on the sphere, similarly to the well-known Shannon-Nyquist theorem on $\mathbb{R}^n$. Therefore, for a band limited function at order L, an exact reconstruction is possible with $(2L-1)^2$ samples [Driscoll and Healy, 1994]. The samples are simply the nodes of an equiangular grid (also called longitude-latitude sampling), as shown on Fig. 5.10. This construction was recently improved, and it is shown in McEwen and Wiaux [2011] that exact reconstruction is feasible with only $2L^2 - 3L + 2$. The use of this scheme has been investigated for the application to diffusion signal measurements [Daducci et al., 2011], for multiple-shell sampling protocols.

These equiangular grids for sampling provide theoretical background on the exact reconstruction of band-limited signal. In addition, these equiangular sampling schemes can be associated with fast Fourier transform algorithms, which is most appreciated in applications where the truncation order L becomes large (several thousands in McEwen and Wiaux [2011]). However, it is clear that these sampling schemes are not uniform on the sphere, and therefore the reconstruction accuracy might not be rotational invariant. Besides, there is no proof that the number of samples given by these sampling theorems consists in a minimum for exact recon-

struction. As the cost in diffusion MRI is clearly on acquisition time, rather than on computational complexity, the price to pay for potentially many measurements is to be investigated more closely.

Summary of advantages and limitations of the equiangular grid sampling and theorem on the sphere

+ Construction of acquisition scheme leading to exact reconstruction for band-limited signals,
+ Extremely simple computation of the sampling nodes (equiangular grid),
+ Well adapted to the reconstruction in SH basis, in q-ball imaging,
− The repartition of points on the sphere is not uniform,
− The number of measurements for the same result could be decreased if the constraint of equiangular grid is relaxed.

5.3 Multiple q-shell acquisition

While the study of sampling on the sphere in diffusion MRI has received much attention, it is only very recently that multiple q-shell acquisition and reconstruction techniques have been considered by several groups [Khachaturian et al., 2007, Wu and Alexander, 2007, Assemlal et al., 2009b, Aganj et al., 2010a, Ye et al., 2012]. The acquisition on several shells brings new challenges, and new questions with respect to the placement of points. For a given number of acquisitions, how many shells should be selected? How many points per shell should be selected? How the points should be placed from one shell to another? In this section, we select and present the studies that bring specific methods for multiple q-shell acquisition design.

5.3.1 Geometrical method

In Ye et al. [2012], a geometric construction on concentric spheres is described. Each sphere is associated with an inscribed polyhedron, whose vertices correspond to the sampling points in q-space. In order to separate measurements directions from one shell to another, the construction in this work is based on the concept of dual polyhedra (see Fig. 5.11). From sample measurements on these interlaced concentric spheres of the diffusion signal E in the q-space, the authors in Ye et al. [2012] reconstruct the signal on a regular grid using interpolation, and then estimate the EAP through discrete Fourier transform. The sampling method is shown to

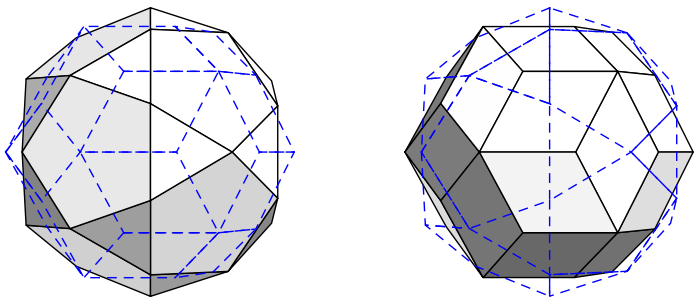

Figure 5.11: (left) icosidodecahedron and (right) its dual polyhedron, the rhombic triacontahedron. The vertices of the dual polyhedron are at the centers of faces of the original polyhedron (see blue, dashed lines). This geometric construction is used to design multiple shell interlaced sampling in Ye et al. [2012]

improve the angular resolution with respect to radial sampling, where sample points are aligned from one shell to another.

This sampling method however has several drawbacks. First, except for the icosahedron ($K = 12$), the vertices of regular polyhedra are in general not uniformly spread on the surface of the sphere. Besides, the construction of a regular polyhedron with an arbitrary number of vertices is not possible. Moreover, the number of points per shell is also fixed by the number of vertices of the considered polyhedra, and cannot be tuned. This is a severe drawback, as it was shown in Assemlal et al. [2009b] that this is an important parameter for the quality of the reconstruction. Finally, the use of a pair of dual polyhedra provides a natural construction for an experiment design on 2 shells. For a larger number of shells, the authors propose to alternatively use one polyhedron and its dual. At the end, shells number $1, 3, \ldots$ share the same sampling directions, and shells number $2, 4, \ldots$ a different set of directions. This is no much different from radial sampling.

Summary of advantages and limitations of the interlaced sampling construction based on dual polyhedra.

+ The sampling directions covers the sphere more densely than radial sampling,
+ The angular resolution is improved,
– Construction not possible for an arbitrary sample size,
– Provides only two separate sets of directions, to share among possibly many spheres,
– The number of points per shell cannot be finely tuned with respect to the radius of each shell.

5.3.2 Noise performance for parametric reconstruction

The acquisition design for multiple q-shell acquisition and parametric reconstruction has been recently studied in Assemlal et al. [2009a]. This study tries to find the sampling strategy that minimizes the condition number of the regularized observation matrix, for the problem of parametric reconstruction of the signal. The basis of interest is the spherical polar Fourier basis (SPF), that we reviewed in the last chapter (see in particular Section 4.2.3). In Assemlal et al. [2009a], the authors consider several possible strategies on how to chose the number of shells in q-space, and the number of points per shell, given a total of K measurements. To reduce the dimension of the configurations to explore, they impose the shell radii to be linearly distributed between $q_{\min}$ and $q_{\max}$. The number of points per shell is considered as a function of the shell radius, and is proportional to q^{α}. Possible values for alpha in their study was $\{-2, -1, 0, 1, 2\}$.

This is an interesting approach, as it is known that the condition number provides a good index of stability of the reconstruction. However the method to minimize the condition number is somehow disappointing: only a few predefined sampling strategies are tested, with the hope that one of these strategies would provide an optimal configuration. Besides, the angular aspect is omitted, and no particular care is addressed to make the sampling directions different from one shell to another, similarly as in Ye et al. [2012]. Finally, the authors chose to minimize the condition number of the regularized matrix, that is the matrix $\mathbf{H}^{\mathrm{T}}\mathbf{H} + \lambda_L\mathbf{L} + \lambda_N\mathbf{N}$, where $\mathbf{L}$ and $\mathbf{N}$ are angular and radial filters, respectively. Therefore the optimum strategy would depend on the regularization weights, which is counter-intuitive. Similarly, no study on the dependence on the choice of the scale factor ζ of the SPF basis is provided.

Summary of advantages and limitations of the optimal acquisition strategy in parametric q-space imaging.

+ The sampling strategy is adapted to the reconstruction problem,
+ The condition number is reduced, as compared to naive approach,
− Angular coverage of the acquisition scheme is not investigated,
− No systematic method to minimize the condition number is provided,
− Effect of $q_{\max}$ not investigated.

5.4 Summary of the chapter

In this chapter, we have presented a review of state-of-the-art acquisition methods and strategies developed in diffusion MRI. In the literature, different groups seem

working on q-ball imaging seem to converge to the use of electrostatic-like repulsion Jones et al. [1999a], Jansons and Alexander [2003], as it is the most flexible tool to generate uniform point sets on the sphere, with antipodal symmetry. For multiple shell acquisition, such a method has not been proposed yet, and we present in Chapter 9 a general and flexible method for the construction of uniform point sets on multiple shell.

Moreover, both for q-ball and q-space imaging, the approaches are either purely geometrical, either purely driven to the best possible reconstruction of interest. However we have seen for instance that the minimization of the condition number [Skare et al., 2000] or the total variance [Papadakis et al., 1999] in diffusion tensor imaging leads to non unique solution. In Chapter 9, we present a unifying framework, that takes into account both the reconstruction problem, and the question of angular uniformity.

Part III

Contributions

Chapter 6

Robust Signal Reconstruction with Continuity Constraint and Optimal Regularization

Contents

Overview

What are the parametric spaces of function to describe the diffusion signal in the q-space? What kind of regularization can be proposed for a reconstruction robust to noise? In this chapter, we present a method for the reconstruction of the diffusion attenuation in the whole q-space, with a special focus on continuity and optimal regularization. We derive a modified Spherical Polar Fourier (mSPF) basis, orthonormal and compatible with SPF (see Section 4.2.3), for the reconstruction of a signal with continuity constraint. We also derive the expression of a Laplace regularization operator in the basis, together with a method based on generalized cross validation for the optimal choice of the parameter. Our method results in a noticeable dimension reduction as compared with SPF. Tested on synthetic and real data, the reconstruction with this method is more robust to noise and better preserves fiber directions and crossings.

Keywords q-space imaging; parametric reconstruction; ensemble average propagator; Laplace regularization; continuity constraint.

Organization of the chapter

We first shortly review the definition of the SPF basis, and we exhibit the subspace of continuous functions described in this basis, verifying $E(\mathbf{0}) = 1$. We show that this subspace is an affine subspace, and we provide a reconstruction method through a novel basis, the mSPF basis, to directly estimate a signal with continuity constraint. On the top of this method, we propose a Laplace regularization, which is a classical operator in signal and image processing. Its expression in the mSPF basis leads to a quadratic form of the coefficients, and can be efficiently added as a penalization term to the least-squares estimation problem. Most mathematical derivations are described in the appendices.

6.1 Introduction

In diffusion MRI, the acquisition and reconstruction of the signal attenuation on the 3D q-space allows reconstruction of the full probability of water molecules displacement, known as the ensemble average propagator (EAP). The radial and angular information contained in the EAP opens a wide range of applications, such as the definition of new biomarkers [Cluskey and Ramsden, 2001, Piven et al., 1997], or the characterization of axon diameters in the brain white matter [Assaf et al., 2008, Özarslan et al., 2011]. The reconstruction techniques are based on the acquisition of diffusion-sensitized MR signals, with the acquisition sequence described in [Stejskal and Tanner, 1965], in which a pair of diffusion encoding magnetic field

gradient are applied before and after the 180° pulse. There exists a Fourier relation between the diffusion attenuation $E(\mathbf{q})$ and the EAP

$$P(\mathbf{r}) = \int_{\mathbb{R}^3} E(\mathbf{q}) e^{-2\imath\pi \mathbf{q}\cdot\mathbf{r}} \mathrm{d}^3\mathbf{q}, \tag{6.1}$$

where the wave vector $\mathbf{q}$ is directly related to the applied magnetic field gradient pulse magnitude, direction, and duration.

The diffusion tensor [Basser et al., 1994b] is the first model historically proposed to describe the EAP. Despite its wide acceptance into the research and clinical communities, this model restricts the diffusion EAP within the family of Gaussian probability density functions, and is limited for the description of complex tissue structure. Since then, several models and methods were described to extend the results of diffusion tensor, such as high angular resolution diffusion imaging [Tuch, 2004a, Descoteaux et al., 2007b, Aganj et al., 2010a], or higher order tensors [Özarslan and Mareci, 2003]. Beyond these approaches, it is possible to reconstruct the model-free diffusion propagator, through Diffusion Spectrum Imaging (DSI) [Wedeen et al., 2005], Diffusion Propagator Imaging (DPI) [Descoteaux et al., 2011], Diffusion Order Transform [Özarslan et al., 2011] or reconstruction in Spherical Polar Fourier (SPF) basis [Assemlal et al., 2009b]. DSI relies on the sampling of the diffusion signal on a regular Cartesian grid, and reconstructs the EAP through fast Fourier transform. The main limitation of DSI is its huge demand in acquisition time, and gradient pulse strength to fulfill the Nyquist conditions [Callaghan, 1991b, Tuch, 2004a, Wedeen et al., 2005].

DPI [Descoteaux et al., 2011] is a more natural method to describe the diffusion signal by a basis of functions solution to the 3D Laplace equation by parts. Though this method enables analytical reconstruction of the diffusion propagator, it cannot represent the diffusion signal in the whole q-space. Indeed, DPI represents the signal using the 3D Laplace equation by part [Descoteaux et al., 2011]

$$E(q\cdot\mathbf{u}) = \sum_{l,m} \left[\frac{c_{l,m}}{q^{l+1}} + d_{l,m} q^l \right] Y_{l,m}(\mathbf{u}), \tag{6.2}$$

where $Y_{l,m}$ is the real, spherical harmonic function. The basis functions in DPI diverge both for $q \to 0$ and $q \to \infty$.

The SPF basis functions instead have a radial profile with a Gaussian-like decay, which is similar to the commonly observed diffusion signal. Besides, it is possible to recover the EAP [Cheng et al., 2010b] and the Orientation Distribution Function (ODF) [Cheng et al., 2010a] from the coefficients of the signal reconstructed in the SPF basis. The SPF basis is thus a unique, model-free approach for the reconstruction of the full signal E, the estimation of EAP and its derived characteristics. It has been introduced in [Assemlal et al., 2009b] together with a regularization method to overcome ill-condition of the estimation problem.

However, the definition of the 3D functions of the SPF basis makes use of the parameterization $\mathbf{q} \in \mathbb{R}^3 = q \cdot \mathbf{u}$, where $q \in \mathbb{R}^+$ and $\mathbf{u} \in \mathcal{S}^2$. Near the origin, the corresponding $\mathbf{u}$ is not unique, and we show in Section 6.2.1 that continuity problems near the origin may arise if this parameterization is not used with care. Adding to that, the regularization method introduced in [Assemlal et al., 2009b] is based on a pair of empirical angular and radial low-pass filters. This regularization method fully relies on the choice of the basis of functions. Besides, its implementation requires to tune two separate regularization weights, which is impractical.

In this chapter, we present original and efficient solutions to solve all these important problems. First, we show that continuous functions reconstructed in the classical SPF basis lie in an affine subspace which has a significantly reduced dimension. This means that the signal diffusion could be represented in this subspace with less coefficients, leading to an estimation process with less measurements than those required when representing the signal in the classical SPF basis. Second, we propose a modified SPF (mSPF) basis, an orthonormal basis for this affine subspace, compatible with the SPF basis, but with reduced dimension and intrinsic continuity near the origin. Thus, the signal reconstructed in the mSPF will satisfy the important continuity constraint. Third, a Laplace regularization functional in the mSPF basis is proposed and minimized for a robust reconstruction of the diffusion signal. The method is analytical and ensures a fast implementation and reconstruction with continuity constraints. The Generalized Cross Validation method is applied to find the unique optimal regularization weight between the regularity of the solution and the data fit. Finally, synthetic and real data are used to illustrate and validate the proposed method. In particular, better reconstruction results with exact continuity constraints are obtained and illustrated in crossing fibers regions.

6.2 Theory

The Spherical Polar Fourier basis was recently introduced in [Assemlal et al., 2009b] to reconstruct the diffusion signal in the complete 3D space. The functions $B_{n,l,m}$ of this basis are defined as the product of a radial and an angular function

$$B_{n,l,m}(q \cdot \mathbf{u}) = R_n(q) Y_{l,m}(\mathbf{u}). \tag{6.3}$$

$Y_{l,m}$ is the real, symmetric spherical harmonic introduced in [Descoteaux et al., 2006], and the radial function R_n is reported below for the record

$$R_n(q) = \kappa_n L_n^{1/2}\left(\frac{q^2}{\zeta}\right) \exp\left(-\frac{q^2}{2\zeta}\right) \tag{6.4}$$

$$\kappa_n = \sqrt{\frac{2}{\zeta^{3/2}} \frac{n!}{\Gamma(n+3/2)}}, \tag{6.5}$$

where $L_n^{1/2}$ is the generalized Laguerre polynomial, and Γ is the Gamma function $\Gamma(z) = \int_0^\infty t^{z-1}e^{-t}\mathrm{d}t$. We use $\Omega_{N,L}$ to denote the linear space of functions spanned by the truncated basis $\{B_{n,l,m}, n \leq N, l \leq L, |m| \leq l\}$. The choice of the scale factor ζ can be related to the mean diffusivity of the measured data. Several strategies were proposed in Assemlal et al. [2009b], here and throughout the experiments, we retain

$$\zeta = \frac{1}{8\pi^2\tau D}, \tag{6.6}$$

where τ is the diffusion time, and D is the mean diffusivity.

The SPF basis is orthonormal for the dot product

$$\langle f, g\rangle = \int_{\mathbb{R}^3} f(\mathbf{q})g(\mathbf{q})\mathrm{d}^3\mathbf{q}. \tag{6.7}$$

The construction of this basis was motivated by the need for a complete orthonormal basis of antipodally symmetric and real functions. Besides, the radial profiles R_n have a quasi-Gaussian decay, so that even a low radial truncation order leads to an accurate reconstruction and extrapolation beyond the sampling domain of the diffusion weighted attenuation $E(\mathbf{q})$. From the reconstruction of the signal in this basis, we can estimate the EAP following Cheng et al. [2010b] and the ODF following Cheng et al. [2010a].

However, a closer look at the functions $B_{n,l,m}$ near the origin reveals rapid oscillations and a discontinuity. Moreover, by definition the value of the attenuation E is equal to 1 when $\mathbf{q} = \mathbf{0}$, but there is nothing in the SPF basis to impose this. In this chapter, we show that the subset of functions verifying these properties of continuity and imposed value at the origin is an affine subspace of $\Omega_{N,L}$. We propose mSPF, an orthonormal basis for this subspace, and we give for convenience the relation between this modified SPF (mSPF) basis and the SPF basis $B_{n,l,m}$ introduced in Assemlal et al. [2009b].

We also derive the Laplacian regularization functional expression in the mSPF basis, for a robust reconstruction of the diffusion signal. Indeed, the dimension of the basis grows rapidly with the angular and radial orders, and diffusion weighted images have a very low SNR. For the reconstruction of a smooth function, the Laplacian operator is a commonly proposed approach for regularization [Descoteaux et al., 2007b]. We derive the calculation of the Laplacian operator in the mSPF basis. The method is analytical, which ensures a fast implementation and reconstruction.

In this section, we use indifferently a notation with three indices for the bases elements, such as $B_{n,l,m}$, or a notation with a simple index i, convenient for matrix notation. The link between both indexing systems is given by the functions $n(i)$, $l(i)$ and $m(i)$.

6.2.1 Continuity in $\Omega_{N,L}$

Theorem 1. *A function $f = \sum_{n,l,m} a_{n,l,m} B_{n,l,m}$ of the SPF basis is continuous if and only if*

$$\forall l > 0, \forall |m| \leq l, \sum_n a_{n,l,m} R_n(0) = 0. \tag{6.8}$$

The proof of this theorem is detailed in Appendix 6.A. The linear constraint in Eq. 6.8 imposes that the polynomial part of $f_{l,m} = \sum_n a_{n,l,m} R_n$ has no constant term. This linear constraint can be imposed while estimating the coefficients by constrained least squares estimation. Alternatively, we will derive a new basis of functions to span the subspace of continuous functions. This approach greatly simplifies the Laplace regularization formulation and implementation, as we show in the next section.

In addition to this continuity constraint, we emphasize that the diffusion attenuation signal is defined as $E(\mathbf{q}) = S(\mathbf{q})/S(\mathbf{0})$, and therefore should verify

$$f(\mathbf{0}) = 1. \tag{6.9}$$

The set of continuous functions in $\Omega_{N,L}$ verifying Eq. 6.9 is the solution of an inhomogeneous linear equation, and therefore is an affine subspace of $\Omega_{N,L}$. This affine space is fully characterized by an underlying linear subspace, and an origin. It is underlain by $\Omega^0_{N,L}$, the kernel of the associated homogeneous equation $f(\mathbf{0}) = 0$. As for the origin of the affine subspace, we can choose any solution of Eq. 6.9. For the sake of simplicity, we choose a simple Gaussian as the origin.

To sum up, any function $f \in \Omega_{N,L}$ verifying the continuity property, together with the property $f(\mathbf{0}) = 1$ can be expressed as

$$f(\mathbf{q}) = \exp\left(-\frac{||\mathbf{q}||^2}{2\zeta}\right) + \sum_{n,l,m} x_{n,l,m} C_{n,l,m}(\mathbf{q}), \tag{6.10}$$

where $\{C_{n,l,m}\}$ is a basis of $\Omega^0_{N,L}$, the subspace of continuous functions f in $\Omega_{N,L}$ verifying $f(\mathbf{0}) = 0$. In the remaining of this section, we give a construction for the orthogonal basis $\{C_{n,l,m}\}$.

We first construct a basis of radial functions $\{F_n, n = 0 \dots N\}$, expressed as

$$F_n(q) = \chi_n \frac{q^2}{\zeta} P_n\left(\frac{q^2}{\zeta}\right) \exp\left(-\frac{q^2}{2\zeta}\right).$$

This verifies $F_n(0) = 0$; the polynomials P_n and the normalization constant χ_n are to determine, provided that the following orthogonality property is fulfilled

$$\langle F_n, F_p \rangle_{\mathbb{R}^3} = \int_0^\infty F_n(q) F_p(q) q^2 \mathrm{d}q = \delta_{n,p}. \tag{6.11}$$

The substitution $u = q^2/\zeta$ in Eq. 6.11 gives

$$\int_0^\infty \chi_n \chi_m \frac{\zeta^{3/2}}{2} P_n(u) P_p(u) u^{5/2} e^{-u} \mathrm{d}u = \delta_{n,p}. \tag{6.12}$$

The generalized Laguerre polynomial $L_n^{5/2}$ suits this orthogonality property. Finally the modified radial basis functions are

$$F_n(q) = \chi_n \frac{q^2}{\zeta} L_n^{5/2}\left(\frac{q^2}{\zeta}\right) e^{-q^2/2\zeta}, \tag{6.13}$$

and the normalization constant

$$\chi_n = \sqrt{\frac{2}{\zeta^{3/2}} \frac{n!}{\Gamma(n+7/2)}}. \tag{6.14}$$

The diffusion attenuation $E(\mathbf{q}) - \exp(-||\mathbf{q}||^2/2\zeta)$ is reconstructed through the functions

$$C_{n,l,m}(\mathbf{q}) = F_n(||\mathbf{q}||) Y_{l,m}\left(\frac{\mathbf{q}}{||\mathbf{q}||}\right). \tag{6.15}$$

The family of functions $\{C_{n,l,m},\ n = 0 \dots N-1,\ l = 0 \dots L,\ m = -l \dots l\}$ is the modified SPF (mSPF) basis, an orthonormal basis of $\Omega^0_{N,L}$.

The coefficients $x_{n,l,m}$ are estimated by minimization of the squared error criterion $||\mathbf{y} - \mathbf{H}\mathbf{x}||^2$, where $\mathbf{y}$ is the vector of observations $y_k = E(\mathbf{q}_k) - \exp(-||\mathbf{q}_k||^2/2\zeta)$ measured at wave vectors $\mathbf{q}_k$. The observation matrix has entries

$$H_{k,i} = C_{n(i),l(i),m(i)}(\mathbf{q}_k).$$

This new space has a substantially reduced dimension: $\dim(\Omega_{N,L}) = (N+1) \cdot L(L+1)/2$, whereas $\dim(\Omega^0_{N,L}) = N \cdot L(L+1)/2$. This dimension reduction comes from the two systems of linear constraints of Eq. 6.8 ($L(L+1)/2 - 1$ equations), and Eq. 6.9 (1 equation). As an example, when the angular truncation order $L = 4$ is used, the reconstruction in $\Omega^0_{N,L}$ requires 15 less coefficients, to represent the same signal. This simplifies the implementation, reduces the demand in storage capacity, and improves computational efficiency.

6.2.2 Link with the SPF basis

In this section we give the link between SPF and mSPF bases. This relationship is useful as SPF [Assemlal et al., 2009b] is a now a state-of-the-art method in diffusion MRI. We can therefore reconstruct the ensemble average propagator (EAP) following Cheng et al. [2010b], the orientation distribution function (ODF) following Cheng et al. [2010a], or the apparent fiber population dispersion following Assemlal et al. [2011]. The SPF basis is built on Laguerre polynomials $L_n^{1/2}$

while we use $L_n^{5/2}$ in this chapter. Using the recurrence relations between Laguerre polynomials detailed in [Abramowitz and Stegun, 1970, p. 783], we have:

$$F_n(q) = \sum_{i=0}^{n} \frac{3\chi_n}{2\kappa_i} R_i(q) - \frac{(n+1)\chi_n}{\kappa_{n+1}} R_{n+1}(q). \tag{6.16}$$

If the function $f(\mathbf{q}) = E(\mathbf{q}) - \exp(-||\mathbf{q}||^2/2\zeta)$ is expressed in this basis, $f(\mathbf{q}) = \sum x_{n,l,m} C_{n,l,m}(\mathbf{q})$, then the coefficients $a_{n,l,m}$ of E in the SPF basis are obtained by $\mathbf{a} = \mathbf{M}\mathbf{x} + \mathbf{a}^0$, where

$$M_{ij} = \delta_{l(i),l(j)}\delta_{m(i),m(j)} \cdot \begin{cases} \dfrac{3\chi_{n(j)}}{2\kappa_{n(i)}} & n(i) \leq n(j) \\ -\dfrac{n(i)\chi_{n(j)}}{\kappa_{n(i)}} & n(i) = n(j)+1 \\ 0 & n(i) > n(j)+1 \end{cases}$$

and $\mathbf{a}^0 = [\sqrt{4\pi}/\kappa_0 \; 0 \; 0 \; \ldots]^{\mathrm{T}}$, as $\exp(-||\mathbf{q}||^2/2\zeta) = \sqrt{4\pi}/\kappa_0 B_{0,0,0}(\mathbf{q})$.

$\mathbf{M}$ is the change-of-basis matrix from mSPF to SPF, two orthonormal bases. Therefore, this matrix is orthogonal: the orthogonal projection of any function in $\Omega_{N,L}$, represented by its coefficients $\mathbf{a}$ in the SPF basis, onto the subspace $\Omega^0_{N,L}$ has coefficients $\mathbf{x} = \mathbf{M}^{\mathrm{T}}\mathbf{a}$.

6.2.3 Laplace regularization in the mSPF basis

In this section, we propose to introduce a regularization term in the fitting procedure. We choose as a regularization functional

$$U(\mathbf{x}) = \int_{\mathbb{R}^3} |\Delta E_{\mathbf{x}}(\mathbf{q})|^2 \; \mathrm{d}^3\mathbf{q}, \tag{6.17}$$

where $E_{\mathbf{x}}(\mathbf{q}) = \exp(-||\mathbf{q}_k||^2/2\zeta) + \sum_i x_i C_i(\mathbf{q})$ is the reconstructed signal. This continuous operator is rotational invariant, and independent on the choice of a specific basis. Besides, the Laplace operator was already applied successfully for several applications ranging from natural image denoising [You and Kaveh, 2000, Chan and Shen, 2005] to the field of diffusion MRI, for signal reconstruction [Descoteaux et al., 2007b, Koay et al., 2009b, Descoteaux et al., 2010].

We minimize $||\mathbf{y} - \mathbf{H}\mathbf{x}||^2 + \lambda U(\mathbf{x})$, where the observations are $y_k = E(\mathbf{q}_k) - \exp(-||\mathbf{q}_k||^2/2\zeta)$ and $\mathbf{H}$ is the observation matrix. In this section, we write the Laplace penalization as a quadratic form

$$U(\mathbf{x}) = (\mathbf{x} - \mathbf{x}_0)^{\mathrm{T}} \mathbf{\Lambda} (\mathbf{x} - \mathbf{x}_0) + U_0. \tag{6.18}$$

Hence the penalized least squares has a unique minimum

$$\hat{\mathbf{x}} = \mathbf{x}_0 + (\mathbf{H}^{\mathrm{T}}\mathbf{H} + \lambda\mathbf{\Lambda})^{-1}(\mathbf{y} - \mathbf{H}\mathbf{x}_0). \tag{6.19}$$

In what follows, we give explicit directions how to compute the matrix $\mathbf{\Lambda}$ and the vector $\mathbf{x}_0$.

When $E_{\mathbf{x}}(\mathbf{q}) - \exp(-||\mathbf{q}_k||^2/2\zeta)$ is expressed in the mSPF basis with coefficients x_i,

$$\begin{aligned} U(\mathbf{x}) &= \int_{\mathbb{R}^3} \left(\sum_i x_i \Delta C_i(\mathbf{q}) + \Delta e^{-||\mathbf{q}_k||^2/2\zeta} \right)^2 \mathrm{d}^3\mathbf{q} && (6.20) \\ &= \sum_i \sum_j x_i x_j \int_{\mathbb{R}^3} \Delta C_i(\mathbf{q}) \cdot \Delta C_j(\mathbf{q}) \ \mathrm{d}^3\mathbf{q} \\ &\quad +2 \sum_i x_i \int_{\mathbb{R}^3} \Delta C_i(\mathbf{q}) \cdot \Delta e^{-||\mathbf{q}_k||^2/2\zeta} \mathrm{d}^3\mathbf{q} \\ &\quad + \ldots && (6.21) \end{aligned}$$

The constant term is discarded since it plays no role in the minimization. Thus we have the quadratic form of Eq. 6.18, where

$$\Lambda_{ij} = \int_{\mathbb{R}^3} \Delta C_i(\mathbf{q}) \cdot \Delta C_j(\mathbf{q}) \ \mathrm{d}^3\mathbf{q}, \tag{6.22}$$

and $\mathbf{x}_0 = \mathbf{\Lambda}^{-1}\mathbf{v}$, with

$$v_i = \int_{\mathbb{R}^3} \Delta C_i(\mathbf{q}) \cdot \Delta e^{-||\mathbf{q}_k||^2/2\zeta} \mathrm{d}^3\mathbf{q} \tag{6.23}$$

The Laplace operator Δ can be written in spherical coordinates, with the Laplace-Beltrami operator Δ_{b},

$$\begin{aligned} \Delta C_{n,l,m}(q\ \mathbf{u}) &= \chi_n \Big(\frac{1}{q^2} \frac{\partial}{\partial q} \big(q^2 F_n'(q) \big) Y_{l,m}(\mathbf{u}) \\ &\quad + \frac{F_n(q)}{q^2} \Delta_{\mathrm{b}} Y_{l,m}(\mathbf{u}) \Big) && (6.24) \end{aligned}$$

Since the spherical harmonics are eigenfunctions of the Laplace-Beltrami operator with eigenvalue $-l(l+1)$, we have

$$\Delta C_{n,l,m}(q\ \mathbf{u}) = \chi_n \Big(F_n''(q) + 2\frac{F_n'(q)}{q} - \frac{l(l+1)F_n(q)}{q^2} \Big) Y_{l,m}(\mathbf{u}) \tag{6.25}$$

As the spherical harmonics form an orthonormal basis for the canonical dot product on $\mathcal{S}^2$, the entries of the matrix $\mathbf{\Lambda}$ are

$$\Lambda_{i,j} = \delta_{l(i),l(j)} \delta_{m(i),m(j)} \int_0^\infty h_i(q) h_j(q) \, \mathrm{d}q, \tag{6.26}$$

where

$$h_i = \chi_{n(i)} \left(q F_{n(i)}'' + 2F_{n(i)}' - \frac{l(i)\,(l(i)+1)}{q} F_{n(i)} \right). \tag{6.27}$$

Similarly, the vector $\mathbf{v}$ has entries

$$v_i = \delta_{l(i),0}\delta_{m(i),0} \int_0^\infty h_i(q) \cdot \left(\frac{q^3}{\zeta^2} - \frac{3q}{\zeta}\right) \exp\left(-\frac{q^2}{2\zeta}\right) \mathrm{d}q. \tag{6.28}$$

The computation of the integrals in Eq. 6.26 and 6.28 is analytical and needs no numerical integration. It is described in details in Appendix 6.B.

6.3 Material and methods

6.3.1 Optimal regularization parameters

We adopted the Generalized Cross Validation (GCV) algorithm [Craven and Wahba, 1985] to find the regularization weight λ which guarantees the best balance between the smoothness of the reconstruction, and the data fit. This algorithm, as well as the L-curve method [Hansen, 2000], have already been applied successfully for other applications in q-ball diffusion MRI [Koay et al., 2009b, Descoteaux et al., 2010, 2007b]. The GCV method has the major advantage to be generalizable to the situation where there is more than one λ parameter to optimize. It is the case in [Assemlal et al., 2009b], where there are two regularization matrices $\mathbf{N}$ and $\mathbf{L}$, which act respectively as radial and angular low-pass filters, with corresponding weights λ_N and λ_L.

The GCV method is based on a one-fold cross validation: among K samples, we use $K-1$ samples to fit the model parameters, and predict the K-th left-apart sample. The process is repeated K times, and the mean prediction error is the value we want to minimize. Fortunately, the mean prediction error, called the GCV function, has a simple expression

$$\mathrm{GCV}(\lambda; \mathbf{y}) = \frac{||\mathbf{y} - \hat{\mathbf{y}}_\lambda||^2}{K \ - \mathrm{Tr}(\mathbf{S}_\lambda)}, \tag{6.29}$$

which makes this method very efficient. The matrix $\mathbf{S}_\lambda = \mathbf{H}(\mathbf{H}^\mathrm{T}\mathbf{H} + \lambda\mathbf{\Lambda})^{-1}\mathbf{H}^\mathrm{T}$ is the smoother matrix, and $\hat{\mathbf{y}}_\lambda = \mathbf{S}_\lambda\mathbf{y}$. With the GCV method, it is possible to adapt the regularization parameters to the data. However, there is no analytical solution for the minimization of the GCV function and for computational efficiency, we compute the optimal λ parameters once. This choice is validated in the next section, and results show it is indeed a good compromise.

6.3.2 Synthetic and real data

We simulate diffusion weighted measurements with a multi-compartment Gaussian model

$$E(\mathbf{q}) = \sum_{p=1}^{P} \omega_p \exp(-2\pi\tau\mathbf{q}^\mathrm{T}\mathbf{D}_p\mathbf{q}), \tag{6.30}$$

where $P \in 1, 2, 3$ is the number of compartments, ω_p is the relative compartment size and $\mathbf{D}_p$ the corresponding diffusion tensor. The diffusion weighted signal is corrupted by Rician noise, with controlled variance parameter σ. Using this diffusion model locally, we created a synthetic diffusion field simulating a sin-shaped and a straight fiber, crossing each other at 90°.

The wave vectors $\mathbf{q}_k$ for synthesis are arranged on 3 shells, with the strategy recently proposed in [Caruyer et al., 2011a,b]. In short, this method is a generalization of the electrostatic repulsion, introduced in [Jones et al., 1999b] for single q-shell experiment design, to the multiple q-shell case.

The experiments on real data were carried out on the publicly available phantom [Poupon et al., 2008a, Fillard et al., 2011] which served as the data for a tractography contest, held at the DMFC MICCAI workshop, London (2009). The diffusion signal was sampled on 3 q-shells, with b-values ranging from 650 to 2000 $\mathrm{s \cdot mm^{-2}}$, and 64 directions per shell.

For the experiments, we compare the diffusion signal, the ensemble average propagator (EAP) reconstructed from the SPF coefficients by the method in [Cheng et al., 2010b], and the orientation distribution function (ODF) reconstructed in constant solid angle, implementing the technique in [Cheng et al., 2010a].

6.3.3 Exact and empirical continuity constraints

We presented in Section 6.2.1 a linear constraint to impose the continuity of the reconstructed signal. An alternate solution proposed in [Cheng et al., 2010b] is to artificially add P virtual data points $\mathbf{q}_k, k = K + 1 \dots P$ close to zero, verifying $E(\mathbf{q}_k) = 1$. As P goes to infinity, it is possible to show that the solution of this system tends to the exact solution [see Golub and Van Loan, 1983, pp. 410–412]. We study the convergence of this empirical continuity approach. As a measure of discontinuity of the reconstructed signal $\hat{E}$ about $\mathbf{0}$, we define $d(\hat{E})$ the difference between extremal values of the set $\{\lim_{q \to 0^+} \hat{E}(q\mathbf{u}), \mathbf{u} \in \mathcal{S}^2\}$. We also compare the relative difference between the solution $\mathbf{c}_{\mathrm{AC}}$ of the least squares problem with analytical constraint, and the solution $\mathbf{c}_{\mathrm{EC}}(P)$ of the system with empirical constraint with P virtual measurements.

6.4 Results and discussion

6.4.1 Continuity constraint

We compare the solution $\mathbf{c}_{\mathrm{AC}}$ and $\mathbf{c}_{\mathrm{EC}}(P)$, for a single Gaussian distribution. To focus on the continuity constraint, we do not impose any other kind of regularization. The signal is corrupted by Rician noise, with corresponding SNR = 25. An

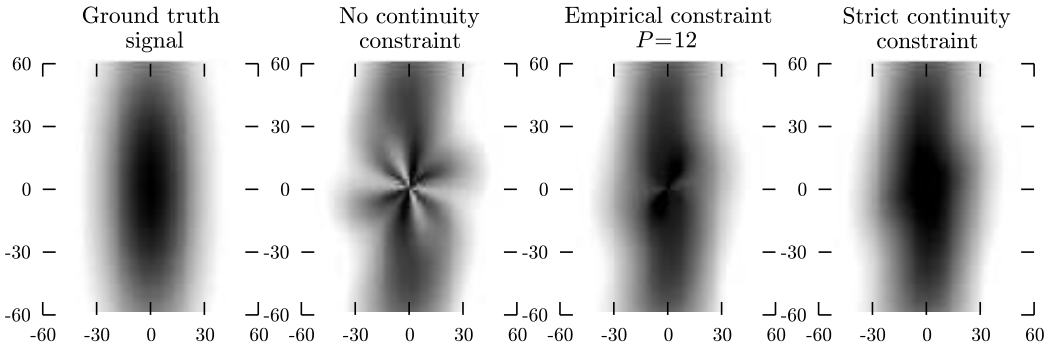

Figure 6.1: Diffusion signal corresponding to a single fiber oriented along the x-axis, reconstructed from 120 samples in the q-space. The signal is shown on the (q_x, q_y)-plane, and the grey levels correspond to signal range from 0.0 (white) to 1.0 (black). q values are understood in mm^{-1}. This illustrates the discontinuity at the origin inherent to the SPF basis, and how the reconstruction in mSPF solves this problem.

example of signal and its reconstruction is reported on Fig. 6.1.

We evaluate the difference of the signal reconstructed with exact continuity constraint and with empirical constraint. We plot on Fig. 6.2 the relative squared difference between the coefficients estimated with a strict continuity constraint, $\hat{\mathbf{c}}_{\text{AC}}$, and the coefficients estimated with an empirical continuity constraint, $\hat{\mathbf{c}}_{\text{EC}}$. The convergence is pretty fast, and $P = 60$ virtual measurements give good results. This confirms the intuition in [Cheng et al., 2010b]; however the minimum number of virtual measurements P for an acceptable accuracy heavily depends on the angular order of the SPF basis, as reported on Fig. 6.2. This makes this empirical solution impractical. Besides, discontinuity is not strictly imposed: as experimented and reported on Fig. 6.3, the value of $d(\hat{E})$ remains unacceptably high while we impose the value on $P = 150$ virtual measurements.

6.4.2 Laplace regularization

Laplace regularization was implemented in the mSPF basis, and we compare it with separate Laplace-Beltrami and radial low-pass filter, proposed in [Assemlal et al., 2009b]. The GCV function is significantly lower for the optimal Laplace regularization (Table 6.1). This result suggests that Laplace regularization is more suitable than separate Laplace-Beltrami and radial low-pass filtering. Furthermore, the optimal λ_Λ parameter does not vary much from one diffusion model to another. We can therefore select a unique λ_Λ parameter for the regularization of a whole volume.

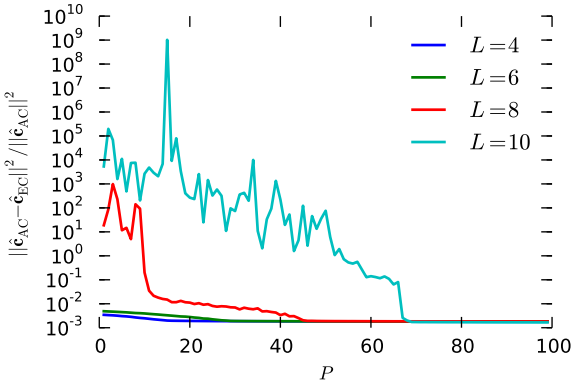

Figure 6.2: Relative difference between reconstruction with a strict continuity constraint, and reconstruction with a loose continuity constraint. Results on a synthetic Gaussian diffusion signal, from $K = 150$ measurements on 3 q-shells, plus P *virtual* measurements at $\mathbf{q} = \mathbf{0}$, for various angular orders L of the SPF basis. Depending on the radial order, the number of additional measurements needed for an accurate reconstruction may become huge, and really impractical.

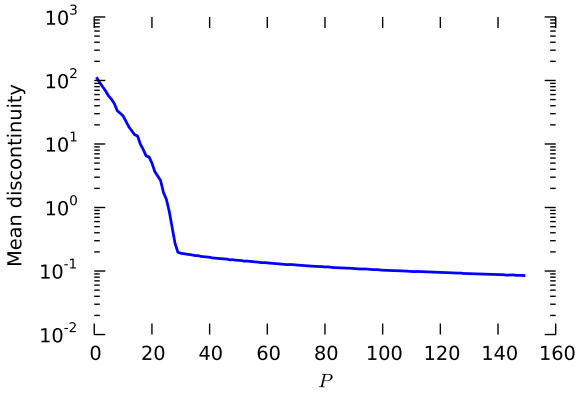

Figure 6.3: Discontinuity, measured about the origin, of a synthetic Gaussian diffusion signal, reconstructed from K measurements on 3 q-shells, plus P *virtual* measurements at $\mathbf{q} = \mathbf{0}$. The discontinuity remains very high, even for a large number of additional, virtual measurements ($P = 150$).

	1 fiber	2 fibers, 90°	2 fibers, 60°
λ_L^0, λ_N^0	$4.0 \cdot 10^{-7}, 8.1 \cdot 10^{-9}$	$3.2 \cdot 10^{-7}, 1.2 \cdot 10^{-8}$	$5.1 \cdot 10^{-8}, 5.5 \cdot 10^{-8}$
$\mathrm{GCV}_{L,N}^0$	$5.7 \cdot 10^{-1}$	$3.4 \cdot 10^{-1}$	$4.8 \cdot 10^{-1}$
λ_Λ^0	$1.6 \cdot 10^{-1}$	$1.7 \cdot 10^{-1}$	$2.4 \cdot 10^{-1}$
GCV_Λ^0	$5.3 \cdot 10^{-1}$	$3.1 \cdot 10^{-1}$	$4.2 \cdot 10^{-1}$

Table 6.1: Optimal λ parameters and corresponding GCV minimum, for various synthetic diffusion models. The sampling consists in 200 diffusion weighted measurements on 3 q-shells, with a max b-value of $3000\mathrm{s} \cdot \mathrm{mm}^{-2}$. Radial and angular orders were set to 5 and 6, respectively. 1st row: separate Laplace-Beltrami and radial low-pass filter smoothing, 2nd row: Laplace regularization.

The regularization also impacts on the extrapolation capacity of the method. Hardware limitations often restrict the sampling to a bounded region in the q-space. Increasing the radial order of the mSPF basis will allow better signal reconstruction within the sampled area of the q-space. It might however introduce undesirable oscillations outside this area, as reported on Fig. 6.4, where the radial truncation order was set to $N = 5$. Adding a regularization constraint greatly improves the extrapolation of the diffusion signal. Laplace regularization performs slightly better in this task, though a more complete study, involving real data and outside the scope of this paper, should be carried out to further validate this.

We also compare the reconstruction with both regularization constraints on our synthetic diffusion field in Fig. 6.5. Laplace regularization performs better in crossing fiber regions, and the results show better directional coherence. Besides, in isotropic regions, the reconstructed ODFs have a smoother profile than with separate Laplace-Beltrami and radial filtering.

Similar results are obtained on the real data experiment, depicted on Fig. 6.6. We have overlaid the ground truth fiber orientations, as provided by Fillard et al. [2011]. The reconstruction results with optimal Laplace regularization show slighly sharper EAP and ODF profiles. We acknowledge that the reconstruction of this dataset was very challenging, due to the low anisotropy of the signal.

6.5 Conclusions

We have proposed a novel orthonormal basis for the reconstruction of the diffusion signal in the complete 3D q-space, based on Gaussian-Laguerre functions. This new method enables the reconstruction of a continuous signal, with known value at the origin. This mathematical constraint results in a dimension reduction with respect to the SPF basis, and a better reconstruction of the diffusion signal at the

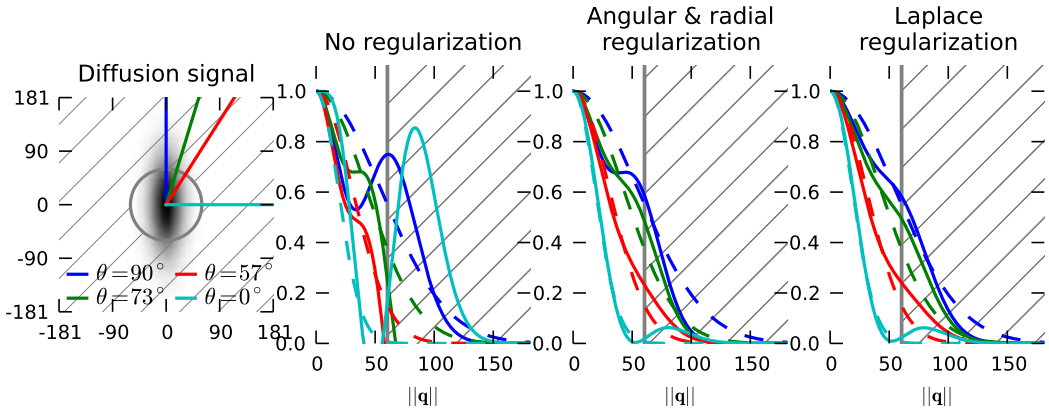

Figure 6.4: Reconstruction and extrapolation of a diffusion signal, for a Gaussian diffusion model, from 120 measurements on 3 q-shells. We plot the reconstructed (solid lines) and ground truth (dashed lines) radial profiles of the signal on selected lines in the q-space. The maximum q value of the sampling scheme was set to 60mm^{-1}, the hatched area represents the no-sample area. We compare the reconstruction without regularization, with separate Laplace-Beltrami and radial filter, and with Laplace regularization. Laplace regularization performs better in smoothing radial profiles, and we avoid oscillations outside the sampling area.

same sampling rate. This also greatly simplifies the reconstruction method, and reduces the associated computational cost as the continuity constraint is naturally imposed. The mSPF basis is presented with its linear relation to the SPF basis for convenience, so that the methods of SPF imaging directly transpose to mSPF.

We also derive a regularization functional based on the Laplace operator, together with its analytical expression in the mSPF basis. This is shown to be mathematically and practically better than separate Laplace-Beltrami and radial low-pass filtering. The experiments on simulations and real data show good results, for the reconstruction and extrapolation of the radial profile. The angular profile reconstruction is more robust to noise, and better detection of fiber crossing is reported.

Summary of the contributions of this chapter

- Continuous signal representation in a modified Spherical Polar Fourier (SPF) basis.
- Dimension reduction with respect to conventional SPF basis.
- Analytical Laplace regularization for a robust reconstruction.
- Optimal regularization weight through generalized cross validation.

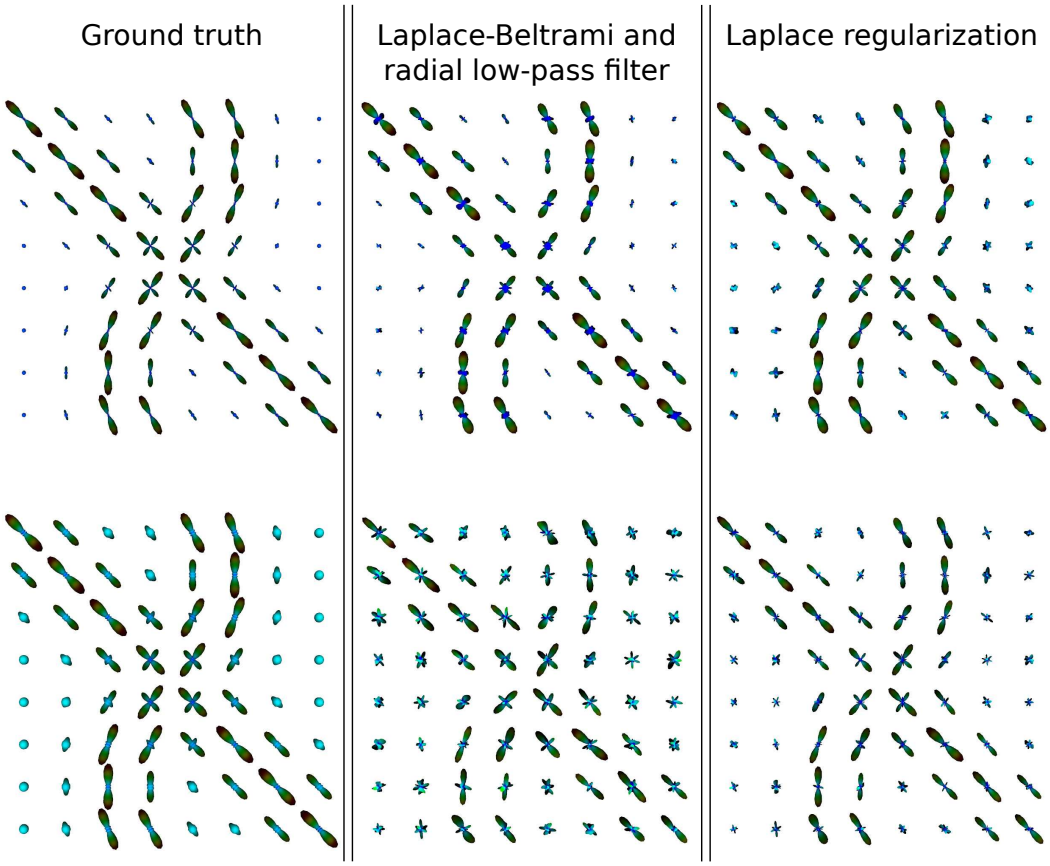

Figure 6.5: Reconstruction of a diffusion propagator field, from 120 measurements on 3 shells (max b-value was $3000\text{s} \cdot \text{mm}^{-2}$). We compare the diffusion EAP profile (top row) $P(r_0\mathbf{u})$, for $r_0 = 15\mu\text{m}$, and the diffusion ODF $\psi(\mathbf{u})$ (bottom row). Fiber crossing are better resolved with Laplace regularization, and isotropic regions are smoother.

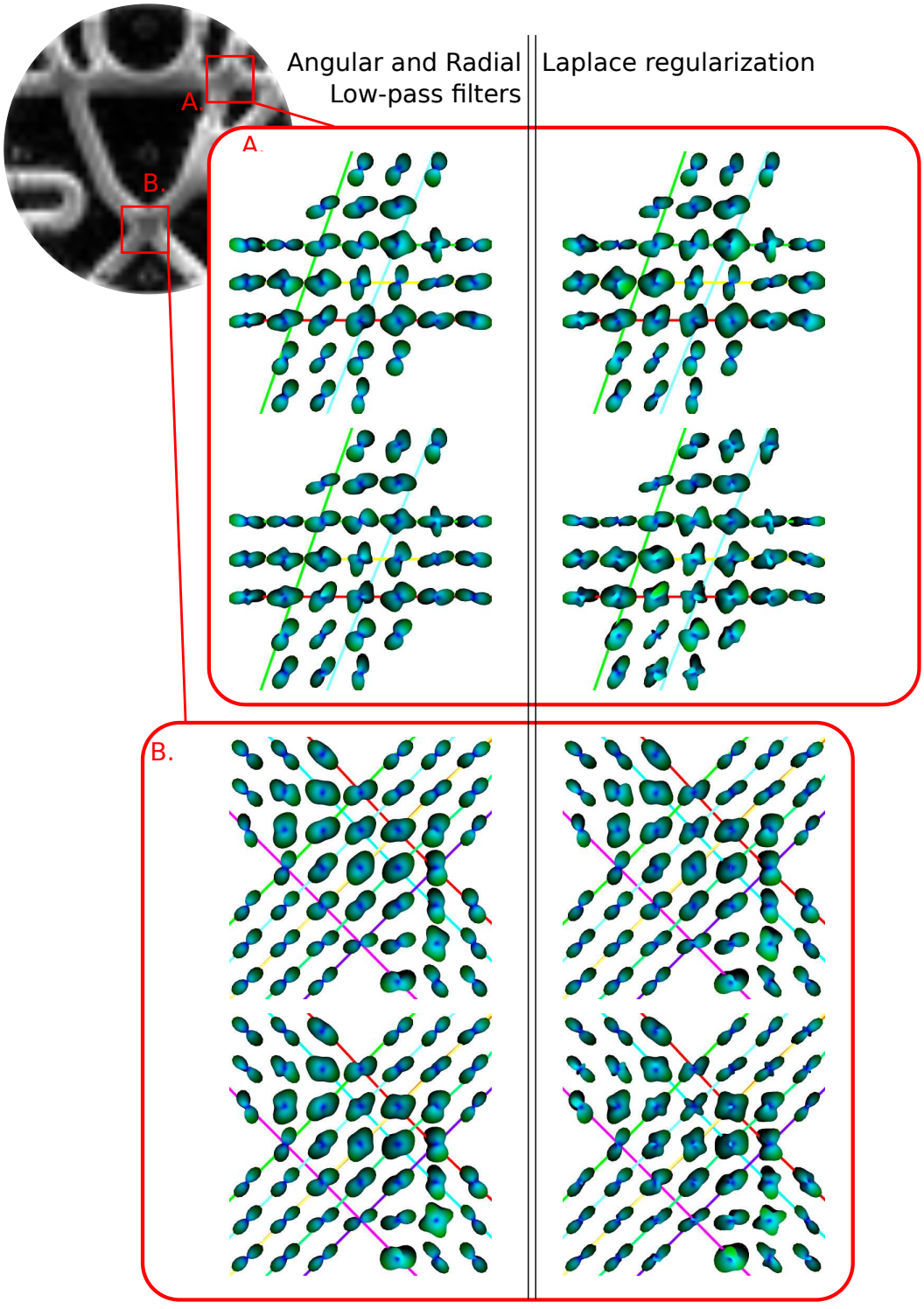

Figure 6.6: Diffusion ODF and EAP profiles reconstructed from the diffusion MRI data of the fiber cup. Zooms on crossing regions A and B are displayed. Within each block: EAP profile $P(r_0\mathbf{u})$, for $r_0 = 17\mu$m (top row) and diffusion ODF reconstructed in constant solid angle $\psi(\mathbf{u})$ (bottom row). The left column corresponds to a reconstruction with separate angular and radial low-pass filters, while the right column is the reconstruction with Laplace regularization. The EAP profiles and ODF reconstructed with Laplace regularization are somehow sharper in crossing regions.

- Validation on simulations and real experimental data.

6.A Necessary and sufficient condition for continuity

In this appendix, we give a proof of Theorem 1, relative to the continuity of a function $f \in \Omega_{N,L}$, expressed as a sum of SPF functions.

6.A.1 Necessary condition

A necessary condition for the continuity of the function f is that the restriction of f to any line in $\mathbb{R}^3$ must be continuous about 0. For $\mathbf{u} \in S^2$ and $q \in \mathbb{R}$, we note $f_{\mathbf{u}}(q) = f(q\mathbf{u})$ the restriction of f to the line of direction $\mathbf{u}$.

$$\lim_{q \to 0^+} f_{\mathbf{u}}(q) = f_{\mathbf{u}}(0) = f(\mathbf{0}) \tag{6.31}$$

$$\Rightarrow \quad \sum_{n,l,m} a_{n,l,m} R_n(0) Y_{l,m}(\mathbf{u}) = f(\mathbf{0}) \tag{6.32}$$

$$\Rightarrow \quad \sum_{l,m} \left(\sum_{n=0}^{N} a_{n,l,m} R_n(0) \right) Y_{l,m}(\mathbf{u}) = f(\mathbf{0}). \tag{6.33}$$

Eq. 6.33 must hold for any $\mathbf{u} \in S^2$. The left hand part is written as a sum of spherical harmonic functions, while the right hand part does not depend on $\mathbf{u}$.

The only constant function in the Spherical Harmonics basis is $Y_{0,0}$. Hence all the spherical harmonic coefficients in Eq. 6.33 must be zero, except for $l = m = 0$.

$$\forall l > 0, \forall m \text{ s. t. } |m| \leq l, \sum_{n=0}^{N} a_{n,l,m} R_n(0) = 0 \tag{6.34}$$

6.A.2 Sufficient condition

Now we show that if the necessary condition in Eq. 6.34 is met, then the function f is continuous about $\mathbf{0}$. We can write f as a finite sum of functions $f_{l,m} = \sum_n a_{n,l,m} B_{n,l,m}$. If we prove the continuity of $f_{l,m}$, for any $0 \leq l \leq L$ and any $-l \leq m \leq l$, then by linearity we prove the continuity of f.

The continuity of f_{00} is direct, as the Gauss-Laguerre functions are continuous and Y_{00} is constant. Next, we consider $0 < l \leq L$ and $-l \leq m \leq l$. By continuity of R_n, we can write $\forall \epsilon' > 0, \exists \alpha > 0$ such that

$$|q| < \alpha \Rightarrow \left|\left| \sum_{n=0}^{N} a_{n,l,m} R_n(q) \right|\right| < \epsilon'. \tag{6.35}$$

This is true for $\epsilon' = \epsilon / ||Y_{l,m}||_\infty$. Besides,

$$\forall \mathbf{u} \in S^2, \frac{|Y_{l,m}(\mathbf{u})|}{||Y_{l,m}||_\infty} \leq 1, \tag{6.36}$$

hence

$$\forall \mathbf{u} \in S^2, |q| < \alpha \Rightarrow \tag{6.37}$$

$$\left|\left|\sum_{n=0}^{N} a_{n,l,m} R_n(q)\right|\right| \frac{||Y_{l,m}(\mathbf{u})||}{||Y_{l,m}||_\infty} < \frac{\epsilon}{||Y_{l,m}||_\infty}. \tag{6.38}$$

This proves the continuity of $f_{l,m}$ about $\mathbf{0}$, and by linearity the continuity of f.

6.B Laplace regularization matrix

In this appendix, we derive the general expression of the Laplace regularization matrix $\mathbf{\Lambda}$ in the mSPF basis. The entries of the matrix $\mathbf{\Lambda}$ are

$$\Lambda_{i,j} = \delta_{l(i),l(j)} \delta_{m(i),m(j)} \int_0^\infty h_i(q) h_j(q) \, \mathrm{d}q, \tag{6.39}$$

where

$$h_i = \chi_{n(i)} \left(q F''_{n(i)} + 2 F'_{n(i)} - \frac{l(i)\,(l(i)+1)}{q} F_{n(i)} \right). \tag{6.40}$$

The function h_i can be written as

$$h_i(q) = \chi_{n(i)} \frac{q}{\zeta} \exp\left(-\frac{q^2}{2\zeta}\right) G_{n(i),l(i)}\left(\frac{q^2}{\zeta}\right), \tag{6.41}$$

where $G_{n,l} = \sum_k g_k^{n,l} X^k$ is a polynomial. It is hard to express the coefficients $g_k^{n,l}$ in a compact form. Instead of manually deriving these coefficients, we compute them using polynomial algebra facilities, provided in the SciPy library [Jones et al., 2001] in Python™. The coefficients $g_k^{n,l}$ are algebraically computed on demand as it involves simple operation on polynomials: derivation and addition. The first coefficients are given in Table 6.B for convenience.

Hence the integrand $h_i(q)h_j(q)$ can be written as

$$h_i(q) h_j(q) = \frac{\chi_{n(i)} \chi_{n(j)}}{\zeta} \exp\left(-\frac{q^2}{\zeta}\right) T_{i,j}\left(\frac{q^2}{\zeta}\right) \tag{6.42}$$

where $T_{i,j}(X)$ is the polynomial $X G_{n(i),l(i)}(X) G_{n(j),l(j)}(X)$. The coefficients $a_k^{i,j}$ of $T_{i,j}$ are simply obtained from the coefficients of $G_{n(i),l(i)}$ and $G_{n(j),l(j)}$. Therefore, the entries of the regularization matrix are

$$\begin{aligned} \Lambda_{i,j} &= \frac{\chi_{n(i)} \chi_{n(j)}}{\zeta} \sum_{k=0}^{d} a_k^{i,j} \int_0^\infty \exp(-q^2/\zeta) \left(\frac{q^2}{\zeta}\right)^k \mathrm{d}q \\ &= \frac{\chi_{n(i)} \chi_{n(j)}}{2\sqrt{\zeta}} \sum_{k=0}^{d} a_k^{i,j} \Gamma(k + 1/2). \end{aligned} \tag{6.43}$$

h

Table 6.2: Coefficients $g_k^{n,l}$ of the polynomials involved in the computation of the Laplace regularization matrix in mSPF basis.

k	$G_{0,l}$	$G_{1,l}$	$G_{2,l}$
0	$6 - l(l+1)$	$7(3 - l(l+1)/2)$	$15.75(3 - l(l+1)/2)$
1	-7	$-44.5 + l(l+1)$	$-145.125 + 4.5l(l+1)$
2	1	14.5	$78.375 - l(l+1)/2$
3		-1	-12
4			0.5

Chapter 7

Online Reconstruction of the ODF in High Angular Resolution Diffusion Imaging and its Application to Motion Detection

Contents

Overview

Is it possible to process the diffusion signal during acquisition, in real-time? Could the ODF be estimated online? What kind of feedback could an online estimation system provide on the accuracy of the reconstructed diffusion information? In this chapter, we first provide an online estimation method of the ODF in constant solid angle, based on Kalman filter. We carefully design the Kalman filter to include an adequate error propagation method, adapted to the estimation of the ODF in constant solid angle. This online reconstruction provides a real-time feedback on the reconstruction accuracy throughout the acquisition process. Then, a method called STAR (STatistical Analysis of Residuals) is presented and applied to the online detection of motion in high angular resolution diffusion images. Compared to existing techniques, this method is image-based, and is built on top of a Kalman filter at no additional cost. The performance of STAR is tested on simulated and on real data, and compared to the classical generalized likelihood ratio test.

Keywords online estimation; orientation distribution function; motion detection; q-ball imaging; real-time processing.

Organization of the chapter

We first quickly review the method of estimation of the ODF in constant solid angle in q-ball imaging, with a special focus on error propagation in the least-squares estimation problem. Then we present an incremental solution based on Kalman filtering, to the estimation of this ODF. On the top of the Kalman filter, we propose a method to detect subject motion, based on a monitoring of Kalman filter residuals. We end the chapter with an experimental section, showing the sensitivity and specificity of the motion detection, on real and simulated data.

7.1 Introduction

Diffusion MRI has provided a great tool for neuroscientists to understand and analyze *in vivo* the anatomy of the brain white matter fiber tracts, that connect different areas of the cortex. The diffusion tensor model [Basser et al., 1994a] has become increasingly popular, and the study of scalar indices derived from it has proved useful in the diagnosis of a wide range of neurological diseases [Jones, 2010a, Johansen-Berg and Behrens, 2009]. For several specific applications, among which fiber tractography, this model is however known to be limited, and high angular resolution imaging techniques should be used instead, to reconstruct the model-free ensemble average propagator [Assemlal et al., 2008, Ozarslan et al., 2009, Descôteaux et al., 2009], or the orientation distribution function (ODF) [Tuch, 2004b, Descoteaux et al., 2007a, Aganj et al., 2010b, Tristán-Vega et al., 2009].

The acquisition of high angular resolution diffusion images requires longer time than diffusion tensor imaging. As the quality of the reconstruction depends on the noise level and the acquisition parameters, the number of required acquisitions in diffusion MRI might not be known in advance. Therefore, the online estimation of the ODF provides a valuable feedback on the reconstruction accuracy. A Kalman filtering framework for the online estimation of ODF has already been proposed [Poupon et al., 2008b, Deriche et al., 2009]. The first contribution in this chapter is to adapt the Kalman filtering framework to the online reconstruction of ODF in constant solid angle, recently introduced in the Q-Ball imaging community [Aganj et al., 2010b, Tristán-Vega et al., 2009]. With a special focus on a proper error propagation in the estimation, we show that the Kalman filter provides online a relevant index for the accuracy of the reconstructed ODF.

Besides, subjects are likely to move during diffusion acquisitions, and we can identify at least three motivations to develop a method for the online detection of motion. First, images can be registered prior to diffusion model estimation; however this might increase partial volume effects [Pfefferbaum et al., 2000], because of the relatively low spatial resolution of diffusion weighted images and of interpolation in the registration procedure. This also modifies the variance properties of the image [Rohde et al., 2005], which should be considered carefully for group studies. When subject moves during acquisition, a warning could be issued, so as to take a decision accordingly. Depending on the number of images already acquired, the decision could be to restart the scan, or acquire a few more diffusion weighted images than originally planned to compensate for the variance increase due to the registration. Second, diffusion acquisitions use a gradient table, which is a set of orientations and b-values, and has been designed following an optimal sampling strategy. In Q-ball imaging for instance, the set of orientations is designed to sample the sphere in an optimal isotropic fashion [Jones et al., 1999a, Papadakis et al., 2000]. When correcting for motion, the diffusion encoding gradients should be rotated to be consistently defined in a coordinate frame related to the subject [Rohde et al., 2004, Barmpoutis et al., 2007, Leemans and Jones, 2009]. This modification might break the optimal sampling strategy as originally planned, and affect the reconstruction of the ODF. Finally, in the context of online processing of diffusion images, motion must be detected, so that it can be corrected to continue the incremental reconstruction.

A solution for online motion detection and correction was recently proposed [Aksoy et al., 2011]. The authors use a camera inside the scanner to detect and evaluate a rigid motion. Their study shows the improvement in ODF reconstruction with this prospective approach for motion correction, over a classical offline registration. However this technique requires additional hardware which is to date not always available on scanners. Another approach [Alhamud et al., 2011] is based

on the interleaving of echo navigators through the acquisition sequence. Authors in [Alhamud et al., 2011] also report good results in detecting and correcting motion, but these additional acquisitions affect the overall protocol time.

In this chapter, we apply the online reconstruction to the online detection of motion in Q-ball imaging. Our method does not require new hardware nor change in the acquisition protocol, and is based on a Kalman filter reconstruction of the HARDI signal [Poupon et al., 2008b, Deriche et al., 2009]. Then we introduce STAR (STatistical Analysis of Residuals), an original method for the detection of motion in diffusion weighted images. The method is tested under various experimental conditions on semi-artificial and on real data, and compared to the Generalized Likelihood Ratio Test (GLRT) [Willsky and Jones, 1976]. In the Results section, we report successful detection of small motion (rotation by angle under 2°), even in noisy conditions. The detection using STAR outperforms GLRT, while STAR does not need any delay for the detection.

7.2 Methods

In this section, we review the definition and the expression of the ODF calculated in constant solid angle. It has been shown recently that this mathematically correct definition of ODF can be reconstructed in Q-ball imaging [Aganj et al., 2010b, Tristán-Vega et al., 2009]. We present an incremental reconstruction algorithm for this ODF, based on the Kalman filter. A special focus on the noise propagation is addressed, for an accurate reconstruction of the ODF in constant solid angle.

We formalize the problem of motion detection only from the observation of the diffusion signal. We present a brief review of methods for fault detection, in particular GLRT built upon the Kalman filter, as first described by [Willsky and Jones, 1976]. Finally, we present STAR, an original approach based on a statistical modeling of the image. It has several advantages over GLRT. Both algorithms are implemented, and we present at the end of this section the validation methods used to compare them.

7.2.1 ODF in constant solid angle

The ODF is a spherical function, retaining the angular information of the ensemble average propagator, P. When defined as the marginal probability of direction, the ODF, ψ, is the probability for a water molecule to diffuse along a given direction, in a constant solid angle. It is defined from the diffusion propagator as:

$$\psi(\mathbf{u}) = \int_0^\infty P(r\mathbf{u})r^2 \mathrm{d}r. \tag{7.1}$$

In diffusion MRI, we measure the signal, $s(\mathbf{q})$, which is related to the ensemble

average propagator P through a Fourier transform, under the narrow-pulse condition [Callaghan, 1991a],

$$P(\mathbf{r}) = \int_{\mathbf{q}\in\mathbb{R}^3} \frac{s(\mathbf{q})}{s(\mathbf{0})} e^{-2\pi i \mathbf{q}\cdot\mathbf{r}} \mathrm{d}\mathbf{q}. \tag{7.2}$$

Under the assumption of a mono-exponential decay of the diffusion signal s, the relation between $s(\mathbf{q})$, $s(\mathbf{0})$ and the ODF ψ is given by:

$$\psi(\mathbf{u}) = \frac{1}{4\pi} + \frac{1}{16\pi^2}\mathrm{FRT}\left\{\nabla_b^2 \ln(-\ln\frac{s}{s(\mathbf{0})})\right\}(\mathbf{u}), \tag{7.3}$$

where FRT denotes the Funk-Radon Transform, and ∇_b^2 the Laplace-Beltrami operator [Aganj et al., 2010b].

The computation of the ODF can be implemented using the modified spherical harmonic basis for real and symmetric functions [Descoteaux et al., 2007a] to describe the transformed signal $y = \ln(-\ln(s/s(\mathbf{0})))$ [Aganj et al., 2010b], as both the Funk-Radon transform and the Laplace-Beltrami operations in Eq. 7.3 have a close-form matrix expression in the spherical harmonic basis. If $\hat{c}_j$ are the spherical harmonic coefficients that describe y, then the spherical harmonic coefficients to describe the ODF ψ are

$$\hat{c}'_j = \begin{cases} \dfrac{1}{2\sqrt{\pi}} & j = 1 \\ -\dfrac{1}{8\pi}(-1)^{\frac{l_j}{2}} \dfrac{1\times 3\times\ldots\times(l_j+1)}{2\times 4\times\ldots\times(l_j-2)}\hat{c}_j & j > 1, \end{cases} \tag{7.4}$$

$l_j = \{0, 2, 2, 2, 2, 2, 4, 4, 4, \ldots\}$ for $j = \{1, 2, 3, \ldots\}$ is the order associated to the j-th spherical harmonic.

7.2.2 Estimation in presence of noise

The computation of the spherical harmonic coefficients $\hat{\mathbf{c}}$ describing y from a series of measurements $y[k] = \ln(-\ln(s[k]/s(\mathbf{0}))) = \ln(-\ln(s(q\mathbf{u}[k])/s(\mathbf{0})))$, $k = 1\ldots K$ at discrete positions $\mathbf{u}[k]$ on the unit sphere, and a measurement without any diffusion encoding gradient $s(\mathbf{0})$ is implemented by minimizing:

$$M(\mathbf{c}) = (\mathbf{y} - \mathbf{B}\mathbf{c})^{\mathrm{T}}\boldsymbol{\Sigma}^{-1}(\mathbf{y} - \mathbf{B}\mathbf{c}) + \lambda\mathbf{c}^{\mathrm{T}}\mathbf{L}\mathbf{c}. \tag{7.5}$$

The second term is a Laplace-Beltrami regularization constraint on the fitted signal, with the matrix $\mathbf{L}$ having diagonal elements $l_j^2(l_j+1)^2$. The matrix $\boldsymbol{\Sigma}$ in the data fitting term of Eq. 6.17 accounts for the uncertainty in the diffusion weighted measurements $s[k]$, as well as for the distortion introduced by the non-linear transform, which is illustrated in Fig. 7.1. The distortion is higher in high-magnitude and low-magnitude signal modes.

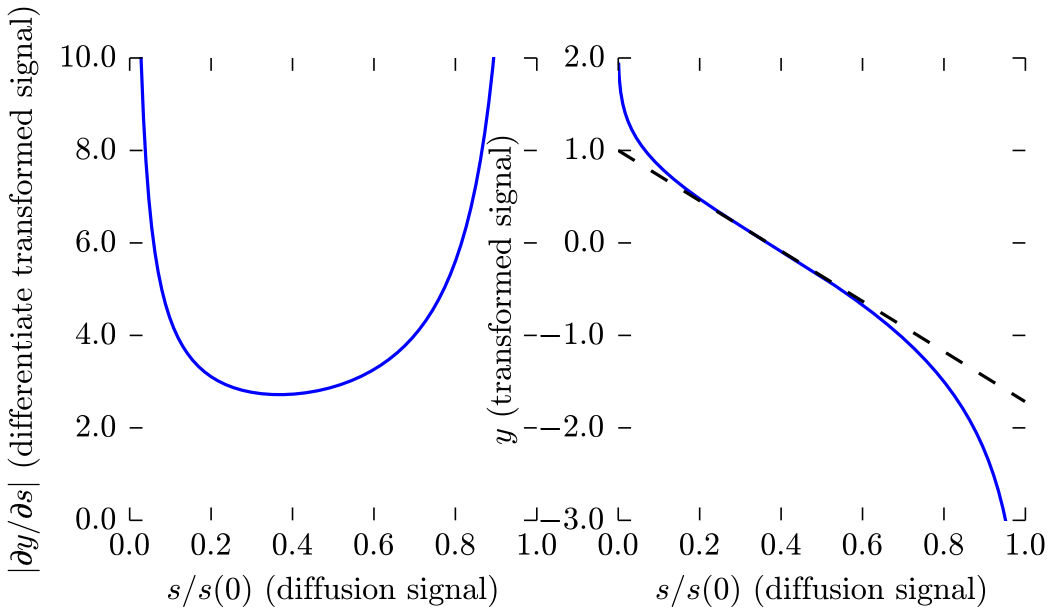

Figure 7.1: (left) Non linear transform on the diffusion signal; (right) derivative with respect to the signal. The distortion is maximum for $s/s(\mathbf{0}) \to 0.0$ and $s/s(\mathbf{0}) \to 1.0$, and minimum for $s/s(\mathbf{0}) \approx 1/e$.

The diagonal elements of $\mathbf{\Sigma}$ can be approximated through first-order error propagation. The uncertainty on the transformed signal y can be approximated as

$$\delta y = \frac{\partial y}{\partial s}\delta s = -\frac{1}{s\ln(s/s_0)}\delta s \tag{7.6}$$

Provided that the error on separate measurements are uncorrelated, the diagonal elements $\sigma^2[k]$ of $\mathbf{\Sigma}$ are

$$\sigma^2[k] = \frac{\mathrm{Var}(s[k])}{s[k]^2\ln^2(s[k]/s_0)}, \tag{7.7}$$

where $\mathrm{Var}(s[k])$ denotes the variance of the diffusion signal $s[k]$, and can be estimated once for the whole volume using a method like PIESNO for instance [Koay et al., 2009a].

7.2.3 Incremental ODF reconstruction

Provided that the acquisition sequence is incremental (in this study we use the incremental point sets as in [Deriche et al., 2009]), the energy in Eq. 6.17 can be minimized incrementally using a Kalman filter [Deriche et al., 2009]. The incremental system adapted to the reconstruction of the ODF in constant solid angle is

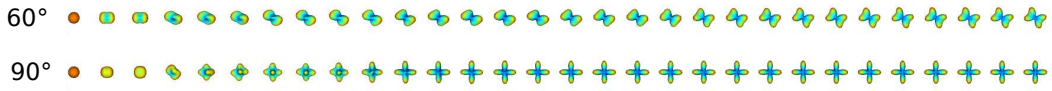

Figure 7.2: Synthetic mixture of Gaussian model, and reconstruction of the ODF in constant solid angle using the Kalman filter. (top) 60°, and (bottom) 90° crossing fibers. The 30 first iterations of the Kalman filter are shown.

given by:

$$\text{Initialization} \quad \begin{cases} \mathbf{c}[0] &= \mathbb{E}[\mathbf{c}] \\ \tilde{\mathbf{P}}[0] &= \mathbb{E}[(\mathbf{c}-\mathbf{c}[0])(\mathbf{c}-\mathbf{c}[0])^{\mathrm{T}}] \\ \mathbf{P}[0] &= (\tilde{\mathbf{P}}[0]^{-1}+\lambda\mathbf{L})^{-1} \end{cases}$$

$$\text{Update} \quad \begin{cases} V[k] &= \mathbf{B}[k]\mathbf{P}[k-1]\mathbf{B}[k]^{\mathrm{T}}+\sigma^2[k] \\ \mathbf{g}[k] &= \mathbf{P}[k-1]\mathbf{B}[k]^{\mathrm{T}}V[k]^{-1} \\ \mathbf{P}[k] &= (\mathbf{I}-\mathbf{g}[k]\mathbf{B}[k])\,\mathbf{P}[k-1] \\ \gamma[k] &= y[k]-\mathbf{B}[k]\mathbf{c}[k-1] \\ \mathbf{c}[k] &= \mathbf{c}[k-1]+\mathbf{g}[k]\gamma[k] \end{cases} \tag{7.8}$$

The $\sigma^2[k]$ depend on the data as expressed in Eq. 7.7, and the covariance $V[k]$ of the residual $\gamma(k)$ can no longer be precomputed off-line. The expected covariance of the estimated spherical harmonic coefficients $\mathbf{c}[k]$ is the matrix $\mathbf{P}[k]$ computed by the Kalman filter. Then the expected mean squared error on the spherical harmonic coefficients describing the ODF is given by:

$$\mathrm{MSE}(\mathbf{c}'[k]) = \mathrm{Tr}(\mathbf{F}^{\mathrm{T}}\mathbf{L}^{\mathrm{T}}\mathbf{P}[k]\mathbf{L}\mathbf{F}), \tag{7.9}$$

where $\mathbf{F}$ is the matrix form of the Funk-Radon transform and has diagonal elements $2\pi P_{l_j}(0)$, where $P_{l_j}(0)$ is the Legendre polynomial of degree l_j evaluated at 0, and $\mathbf{L}$ is the Laplace-Beltrami matrix as in Eq. 6.17.

The Kalman filter was derived with the assumption that the local diffusion propagator does not change in time. Next, we show how we can derive a motion detection algorithm from this Kalman filter.

7.2.4 Motion and diffusion signal

Subject motion generally occurs in a short time compared to the acquisition time. This may induce an *abrupt* change in the diffusion signal. The detection of abrupt changes in dynamical systems has been extensively studied [Willsky and Jones,

1976, Basseville and Benveniste, 1984]; a very good review of methods and algorithms can be found in [Basseville and Nikiforov, 1993]. They propose a classification of change detection problems, together with suggested methods and algorithms to address them.

In the previous section, we have introduced a Kalman filter solution to reconstruct the spherical harmonic coefficients of the Q-ball signal. The state of our system is the vector of spherical harmonic coefficients $\mathbf{c}[k]$, and a motion of the subject at time θ is likely to imply a modification of this state, $\mathbf{c}[k \geq \theta] = \mathbf{c}[k < \theta] + \mathbf{p}$. The problem of motion detection reduces to the problem of change detection in this multidimensional system. Besides, since both the time θ and the magnitude $\mathbf{p}$ of the change are unknown *a priori*, and the classification in [Basseville and Nikiforov, 1993] suggests to use a generalized likelihood ratio test (GLRT) for the detection. In the next section we briefly describe this method and its implementation upon a Kalman filter, as originally introduced in [Willsky and Jones, 1976].

Classical solution: the generalized likelihood ratio test

The Kalman filter presented in the first section is built under the hypothesis of no motion. We can monitor the residuals of this Kalman filter for each iteration, and test whether the hypothesis is still valid. As it has been shown in [Willsky and Jones, 1976], the prediction error after a change occurred at time θ for subsequent iterations can be decomposed as

$$\gamma[k] = \mathbf{G}(k, \theta)\mathbf{p} + \gamma_1[k] \tag{7.10}$$

where γ_1 is zero-mean Gaussian distributed with covariance $V[k]$, $\mathbf{G}(k, \theta)$ represents the propagation of a jump at time θ, to the prediction error at time k. This can be computed as in [Willsky and Jones, 1976],

$$\begin{cases} \mathbf{G}(k, \theta) = \mathbf{B}[k] \left(\mathbf{I} - \sum_{j=\theta}^{k-1} \mathbf{g}[j]\mathbf{G}(j, \theta) \right), \\ \mathbf{G}(k, k) = \mathbf{B}[k]. \end{cases} \tag{7.11}$$

The problem of a change detection is to discriminate between two hypotheses

- $(\mathcal{H}_0)$: no change in the state vector: $\gamma[j] = \gamma_1[j]$, $j = \theta_0 \dots k$,
- $(\mathcal{H}_1)$: at time θ_0, the state vector becomes $\mathbf{c} + \mathbf{p}_0$.

When $\mathbf{p}_0$ and θ_0 are known, a natural statistic for the detection is the likelihood ratio. Provided that the residuals are linearly related to the change (Eq. 7.10), the log-likelihood ratio is

$$l(k; \theta_0, \mathbf{p}_0) = \ln \frac{p_{\mathcal{H}_1}(\gamma[\theta_0 \dots k])}{p_{\mathcal{H}_0}(\gamma[\theta_0 \dots k])}. \tag{7.12}$$

Provided that the densities $p_{\mathcal{H}_0}$ and $p_{\mathcal{H}_1}$ are Gaussian, after simplification this rewrites as

$$l(k;\theta_0,\mathbf{p}_0) = \sum_{j=\theta_0}^{k} \gamma[j]V^{-1}[j]G(j,\theta_0)\mathbf{p}_0. \tag{7.13}$$

In our case, both $\mathbf{p}$ and θ are unknown. The generalisation of the likelihood ratio method suggests to replace θ_0 and $\mathbf{p}_0$ in Eq. 7.13 by their maximum likelihood estimates

$$\begin{aligned} \hat{\theta}(k) &= \arg\max_{\theta} l(k;\theta,\hat{\mathbf{p}}(k;\theta)) \\ \hat{\mathbf{p}}(k;\theta) &= \left(\sum_{j=\theta}^{k} G^T(j,\theta)V[j]^{-1}G(j,\theta)\right)^{-1} \sum_{j=\theta}^{k} G^T(j,\theta)V[j]^{-1}\gamma[j]. \end{aligned} \tag{7.14}$$

Finally, the decision is taken by comparing $l(k;\hat{\theta},\hat{\mathbf{p}})$ to a threshold ϵ.

This technique works fine, yet suffers from several drawbacks. First, the calculation of the maximum likelihood estimate of $\mathbf{p}$ involves the inversion of a matrix in Eq. 7.14 which has full rank only if $k-\theta > \dim(\mathbf{p})$. In other words, this implies a delay at least equal to the dimension of the problem. As an example, when the signal is fitted in the 4-th order symmetric spherical harmonic basis, this dimension is 15. In addition, the choice of a threshold ϵ was reported to be critical, and highly dependant on the delay [Basseville and Benveniste, 1983]. Finally, in our situation the state vector represents the diffusion signal locally, and GLRT does not say how to combine the statistics of different voxels to calculate a statistic which could be an indicator of motion for the whole volume at once. To address these weaknesses, we propose in the next section an original approach without delay, incorporating a statistical model of the image, in order to provide a more suitable detection algorithm.

Statistical Analysis of the Residuals

The reconstructed image is a vector field $\mathbf{c}(\mathbf{r})$, where $\mathbf{c}$ is a vector of spherical harmonic coefficients describing the diffusion signal at voxel position $\mathbf{r}$. We consider the difference $\mathbf{p}$ between two such vector fields $\mathbf{c}_1$ and $\mathbf{c}_2$, representing the same subject before and after a rigid transform. In what follows, we consider $\mathbf{p}(\mathbf{r})$ as a random variable, with unknown covariance matrix $\mathbf{C}$.

Hence if there is no motion, the residuals for the whole volume will be distributed as $\mathcal{N}(0,V[k])$, where $V[k]$ is the variance predicted by the Kalman filter. Otherwise the overall variance of the residuals will increase as $V[k]+\mathbf{G}(k,\theta)\mathbf{C}\mathbf{G}(k,\theta)^{\mathrm{T}}$, where $\mathbf{G}(k,\theta)$ is the matrix for the propagation of a jump at time θ to the prediction error at time k, and the covariance matrix $\mathbf{C}$ of $\mathbf{p}$ is unknown.

Based on the previous observations, we design a test for motion detection without delay. This means that based on measurements up to time k, we are able to decide whether a motion occurred at time k or not. Given a sample of M residuals at time k, at voxel positions $\mathbf{x}_1 \dots \mathbf{x}_M$ selected randomly within the brain, the hypotheses that a motion did occur at time θ or not are equivalent to:

- $(\mathcal{H}_0)$: $\gamma[k]$ has variance $V[k]$, as predicated by the Kalman filter.
- $(\mathcal{H}_1)$: $\gamma[k]$ has a variance $\sigma^2 > V[k]$.

This decision problem is commonly addressed with a one-sided χ^2-test [Snedecor and Cochran, 1989]. We first calculate the statistic

$$T = \frac{\sum_{j=1}^{M} \gamma^2(\mathbf{x}_j)[k] - (1/M \sum_{j=1}^{M} \gamma[k])^2}{V[k]}. \tag{7.15}$$

Under the hypothesis $(\mathcal{H}_0)$, T approximately follows a χ^2_{M-1} distribution. We want to reject the hypothesis with a significance level α: under the hypothesis $(\mathcal{H}_0)$, we compute p such that $\mathbb{P}(T > p) = \alpha$. The value of p is obtained from the inverse cumulative function of the χ^2_{M-1} distribution.

7.2.5 Validation methods

We implemented the incremental reconstruction using Kalman filtering, together with GLRT and STAR for motion detection. These techniques were tested on real data, and a quantitative analysis of both was performed on semi-artificial data, where the motion is simulated by a rigid transform. In this section, we describe how these images were synthesized.

The simulation is based on a tensor field reconstructed images of still subject, acquired on a 3T Siemens magnet at the Center for Magnetic Resonance Research, University of Minnesota Medical School, with 200 encoding directions computed following the optimal sampling scheme of [Deriche et al., 2009], $b = 1000\,\mathrm{s/mm^2}$, 2.0 mm isotropic resolution, 25 $b = 0$ images, 128×128 image matrix, 64 slices, $TE = 90\,\mathrm{ms}$ and $TR = 8500\,\mathrm{ms}$. We choose a series of diffusion gradient directions $\{\mathbf{g}[k], k = 1 \dots K\}$ and a b-value for synthesis. The rigid motion is specified by an instant θ, its rotation component $\mathbf{R}$ and its translation vector $\mathbf{t}$. Provided that the diffusion encoding gradients should be rotated accordingly [Rohde et al., 2004, Barmpoutis et al., 2007, Leemans and Jones, 2009], the gradient directions used for synthesis are $\{\mathbf{g}[1], \mathbf{g}[2], \dots, \mathbf{g}[\theta - 1], \mathbf{R}\mathbf{g}[\theta], \dots, \mathbf{R}\mathbf{g}[K]\}$. The synthetic diffusion weighted images $\theta, \dots, K$ are finally applied the rigid transform $(\mathbf{R}, \mathbf{t})$, and corrupted by Rician noise.

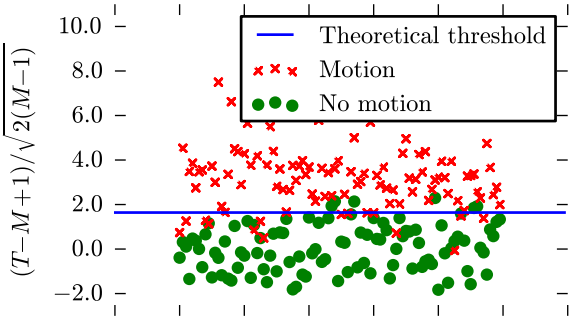

Figure 7.3: STAR statistics for simulations with and without motion. Each point represents a simulation; the theoretical threshold was calculated as explained in Section 7.2.4, so that the FPR does not exceed 5%.

7.3 Results and Discussion

We evaluate the general likelihood ratio, and the residual-based statistics computed for STAR as a motion detection criterion. We first investigate the accuracy of the theoretical threshold in STAR. Then we compare the sensitivity and specificity of GLRT and STAR, for different values of the experimental parameter. Within this section, we report the true positive rate (TPR), defined as TPR = #detected positives / #positives, and the false positive rate, define as FPR = #mislabeled negatives / #negatives.

7.3.1 Threshold selection in motion detection

One of the advantages of STAR outlined in the previous section is that the threshold for the detection can be deduced from the target false positive rate. In practice, as M becomes large, we approximate the χ^2_{M-1} distribution for the decision test described in Section 7.2.4 by a normal distribution: $(T-M+1)/\sqrt{2(M-1)} \sim \mathcal{N}(0,1)$, and p is given by the inverse normal cumulative density function. For a false positive rate fewer than 5%, the theoretical threshold is $(p-M+1)/\sqrt{2(M-1)} = 1.64$. This value is experimentally tested, and the results are presented in the next section.

We report in Fig. 7.3 the value of the statistics $(T-M+1)/\sqrt{2(M-1)}$, for a series of 100 experiments without motion, and a series of 100 experiments where the volume was rotated after 18 acquisitions by an angle of 2°. The threshold was taken as 1.64, for which the false positive probability is 5%. The empirical false positive rate we report for these 200 simulations is 4%, while the true positive rate is 90%.

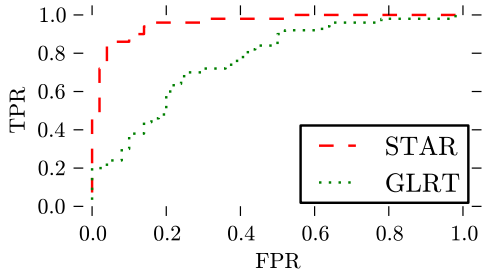

Figure 7.4: TPR versus FPR in motion detection. This experiment was done on 100 datasets without motion, and 100 acquisitions for which a rigid motion (rotation by an angle of 2°) occurred after 20 diffusion weighted images were acquired.

7.3.2 Motion detection: sensitivity and specificity

We computed both detection criteria on a series of 100 datasets without motion, and a series of 100 experiments with motion. We plot in Fig. 7.4 the curve TPR *versus* FPR obtained by choosing different threshold values.

We also evaluate the robustness of GLRT and STAR in various experimental conditions. For a fixed FPR = 5%, we plot the TPR score of both methods. The experimental conditions include the delay, instant of motion in the acquisition sequence, SNR and motion magnitude. Results of these simulations are reported in Fig. 7.5. The experimental conditions, unless explicitly modified, were a rotation around the left-right axis by an angle of 3°, SNR = 20, motion instant $\theta = 20$ and a delay $k - \theta = 3$ (for GLRT). The experiment includes 400 negatives (simulations without motion) and 100 positives (simulations with motion). The monitoring of residuals in STAR and in GLRT is limited to 500 voxels randomly selected within the brain to get a computational cost adequate for online treatment.

Experiment on a real data

We also validate our methods on a real dataset, with the same imaging parameters as above. During the acquisition, the subject was asked to slightly tilt his head after 80 images were acquired. The motion was *a posteriori* identified as a rotation of 20° about the z-axis (see Fig. 7.6). The detection algorithms could detect this motion: with a delay of 2 acquisitions for GLRT, and with no delay for STAR.

7.4 Discussion

Among the challenges of a motion detection algorithm, we have tested both GLRT and STAR in these conditions:

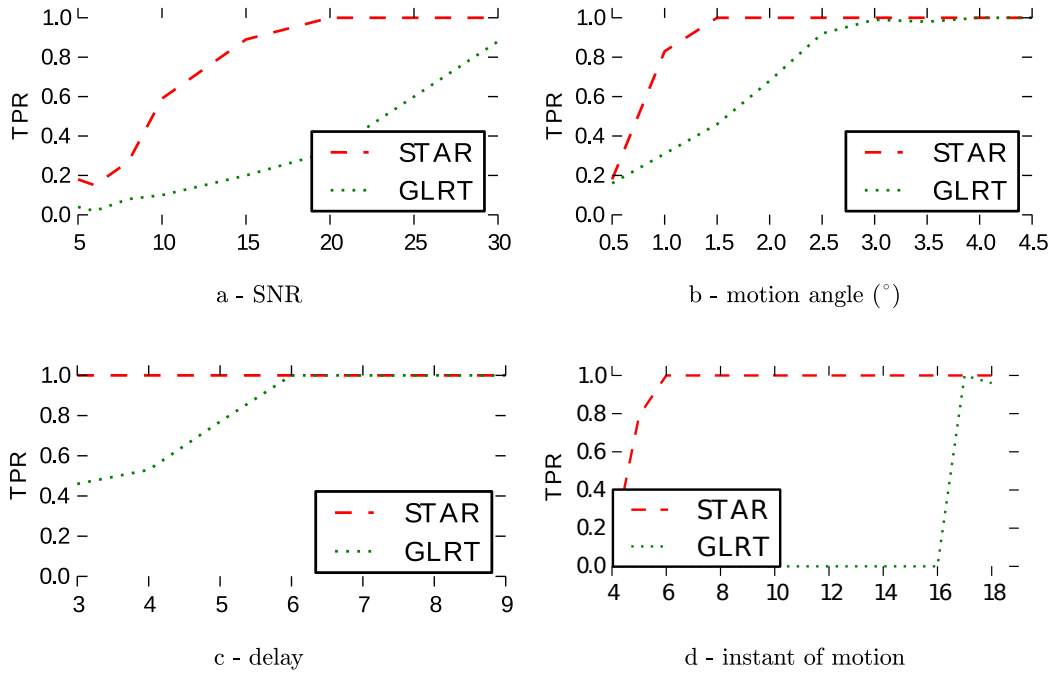

Figure 7.5: TPR: The threshold was chosen so that FPR = 5%. We compare the performance of GLRT and STAR. The dependency on several experimental conditions is tested: (a) SNR, (b) motion magnitude, (c) delay of the detection, (d) instant of motion.

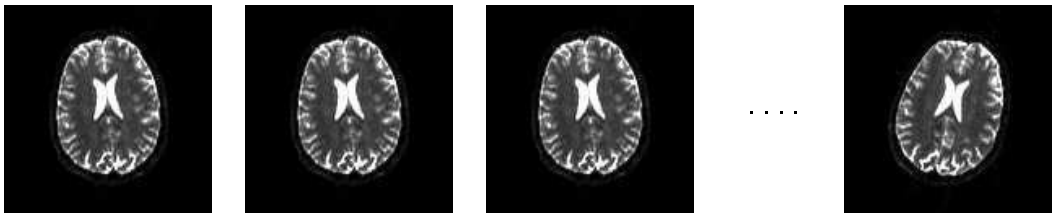

Figure 7.6: A real acquisition: the subject was asked to slightly move his head during the acquisition.

- small delay for the detection (ideally no delay);
- motion that occurred in the first few iterations of the Kalman filter;
- very noisy conditions (SNR down to 10);
- small motion.

Both criteria show good results in detecting motion, even in severe experimental conditions. As expected, STAR is more robust to noise (Fig. 7.5.a), and performs better in detecting small motion (Fig. 7.5.b), since it combines natively the residuals from different voxels.

In addition, GLRT cannot be computed if the number of acquired signal is lower than the dimension of the model, which is 15 in the case of 4^{th}-order real, symmetric spherical harmonics. This impacts the ability to detect motion occurring at the beginning of an acquisition sequence: they are detected by STAR, while GLRT cannot be computed (see Fig. 7.5.d). In addition, GLRT needs a delay greater than 6 to get similar sensitivity as STAR (Fig. 7.5.c). STAR does not need any delay in the decision.

7.5 Conclusions

In this chapter, we have proposed a method for the detection of motion in diffusion MRI. We have developed a Kalman filter solution for the estimation of the ODF in constant solid angle. The detection algorithm STAR is based on the analysis of the residuals of the Kalman filter, yet it is general and can be directly applied to any linear diffusion model reconstruction. Compared to other techniques for the prospective detection and correction of motion [Aksoy et al., 2011, Alhamud et al., 2011], our method does not require any camera or additional device. Once motion is detected by our technique, a decision could be taken by the scanner operator, or the protocol in [Alhamud et al., 2011] could be used for motion correction.

The proposed technique was tested on semi-artificial data as well as in a real data, and shows good results for the online detection of motion. Compared to GLRT, which is a classical solution for the detection of changes in dynamical systems, STAR combines the residuals at different voxel positions to compute a statistic, on which the decision is based. STAR performs better than GLRT in the detection of small motion, motion in noise, or motion occurring early in the acquisition protocol. Besides, STAR does not need any delay for the detection, which makes it very efficient in practical situations.

Summary of the contributions of this chapter

- We present an incremental reconstruction of the ODF in constant solid angle.

- A motion detection algorithm is proposed, on top of the Kalman filter, at no additional cost.
- The motion detection is evaluated on synthetic and real data.

Chapter 8

Design of Angular-Uniform Multiple q-Shell Sampling

Contents

Overview

How to place the sampling directions for a multiple q-shell acquisition? Can we generalize the geometrical approaches in q-ball imaging to several shells? We present in this chapter a method to optimize the angular coverage of a sampling protocol on multiple spheres in q-space. The main objective of this approach is that the sampling is uniform on each shell separately, and is also uniform when considered as a whole. This method can be seen as a generalization of the electrostatic analogy in q-ball imaging experiment design.

Keywords Multiple q-shell acquisition; Angular uniform; Acquisition design; q-space imaging; Angular resolution.

Organization of the chapter

We first present the motivations, along with the energy we minimize to construct angular uniform multiple q-shell acquisition schemes. Depending on the minimization procedure, we show that the same energy can produce incremental acquisition sequence, with an adapted minimization algorithm, compatible with prematurely aborted scans. In the experimental validation, we present some geometrical features of the multiple shell acquisition. Finally, the sampling sets are shown in action, for the reconstruction of diffusion tensor and HARDI models. The angular resolution is compared to other acquisition schemes.

8.1 Introduction

There are many degrees of freedom in the construction of a multiple shell design. If we try to determine all the parameters that fully describe a sampling protocol on several shells, we have: the total number of samples, K; the number of spheres in the q-space, S; the shell radii, q_s; the number of points on each shell, K_s, such that $\sum_{s\leq S} K_s = K$, the positions (directions) on each sampling shell, $\mathbf{u}_{s,k} \in \mathcal{S}^2$.

With the large and increasing number of reconstruction techniques in the literature [Khachaturian et al., 2007, Wu and Alexander, 2007, Assemlal et al., 2009b, Aganj et al., 2010a, Ye et al., 2012] (see Chapter 4, Section 4.2.3), it is not clear whether a preferred, unified strategy would fit the needs of every method. In particular we believe that the selection of parameters K, S, q_s and K_s should be driven by the needs of the reconstruction method, the time limit for the acquisition and the physical limitations of the imaging system. This chapter mainly deals with the choice of the sampling directions, once all other sampling parameters have been set.

8.2 Angular-uniform sampling on multiple shells

We present in this section an electrostatic repulsion energy for the construction of angular-uniform point sets on several shells. The energy is made of two terms: the first controls the angular repartition on each shell, while the second controls the angular uniformity of the set of directions as a whole. A point set minimizing this energy can be constructed by direct minimization, or incrementally. In the latter case, by providing a quasi-uniform distribution of points throughout the acquisition, the sampling sequence will be allow prematurely aborted scans to be processed anyway.

8.2.1 A generalization of electrostatic energy to multiple shell

In the design of q-ball imaging acquisition, the most popular approach is to spread out the sampling directions as uniformly as possible on the sphere (see Chapter 5, Section 5.2.1). Similarly, we propose to construct the sampling directions on each shell, with the following principles. For the sake of rotational invariance, it is desirable that the angular coverage of each sphere be as uniform as possible. Besides, we also require the whole set of directions (*i.e.* the set of all sampling points in q-space, reprojected onto the unit sphere) to be as uniform as possible.

Uniform on each shell

We propose the following electrostatic energy, which is a natural generalization of the method in Jones et al. [1999a], Jansons and Alexander [2003] to multiple q-shell,

$$V_1 = \frac{1}{S}\sum_{s=1}^{S}\frac{1}{K_s^2}\sum_{i\neq j} v(\mathbf{u}_{s,i},\mathbf{u}_{s,j}), \tag{8.1}$$

where the elementary electrostatic repulsion v is

$$v(\mathbf{u},\mathbf{v}) = \frac{1}{||\mathbf{u}-\mathbf{v}||^2} + \frac{1}{||\mathbf{u}+\mathbf{v}||^2}. \tag{8.2}$$

This energy, V_1, is the sum the electrostatic repulsion energy on each shell. The energy of shell s is weighted by $1/K_s^2$. Indeed, the energy increases as K^2 [Cook et al., 2007], and this weighting ensures equal importance of the uniformity for each shell.

Uniform as a whole

So that the whole set of sampling directions be uniform, we also consider this electrostatic energy,

$$V_2 = \frac{1}{K^2}\sum_{s\neq t}\sum_{i=1}^{K_s}\sum_{j=1}^{K_t} v(\mathbf{u}_{s,i},\mathbf{u}_{t,j}). \tag{8.3}$$

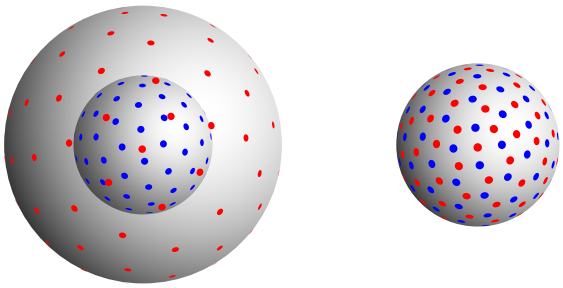

Figure 8.1: Optimal point set on 2 shells, $K_1 = K_2 = 50$ points per shell. The weighting parameter is set to $\alpha = 0.5$. (left) sample points in the q-space, (right) sampling directions, *i.e.* the sampling points reprojected onto the unit sphere.

This energy, V_2, is the sum of all elementary electrostatic repulsions between two pair of points on different shells.

Finally, we construct our set of points by minimizing the energy

$$V = \alpha V_1 + (1 - \alpha) V_2. \tag{8.4}$$

The minimization of V is a non-convex optimization problem. We implemented the minimization through sequential least squares quadratic programming, with analytically pre-calculated gradient, and equality constraints $||\mathbf{u}_{s,k}||^2 = 1$, $s = 1 \dots S$ and $k = 1 \dots K_s$. Our implementation, in Python$^{\text{TM}}$, makes use of the `fmin_slsqp` routine from the SciPy optimization package [Jones et al., 2001]. A solution found for $K_1 = K_2 = 50$ and $\alpha = 0.1$ is plotted on Fig. 8.1.

8.2.2 Balancing per-shell and global uniformity

The weighting parameter $\alpha \in [0, 1]$ in Eq. 8.4 balances the trade-off between uniformity on each shell (measured by energy V_1), and angular uniformity of the sampling scheme as a whole (measured by energy V_2). The case $\alpha = 0$ is somehow underdetermined, as any rotation of one shell with respect to the others does not change the energy. At the opposite, the case $\alpha = 1$ would put all the weight on global uniformity, but nothing would prevent poor angular coverage of each single shell. These two extremal cases are illustrated on Fig. 8.2.

We plot on Fig. 8.3 the value of both energies V_1 and V_2 for the configuration minimizing V, while the α parameter varies from 0 to 1. Except near these extremal values of α, the solution is not much sensitive to the choice of α. Since then, we chose $\alpha = 0.5$ throughout our experiments.

Figure 8.2: Extremal values of the weighting factor α: minimum energy configurations for $S = 2$ shells, $K_1 = K_2 = 50$ points per shell, points reprojected on the unit sphere. (left) $\alpha = 0$: all the importance is given to the uniformity of the configuration on each shell, independently of the other. As a result, the global coverage is non-uniform. (right) $\alpha = 1$: the global angular coverage is uniform, but if we consider the repartition of points on shell 1 (blue dots) or shell 2 (red dots) separately, the angular coverage is not uniform.

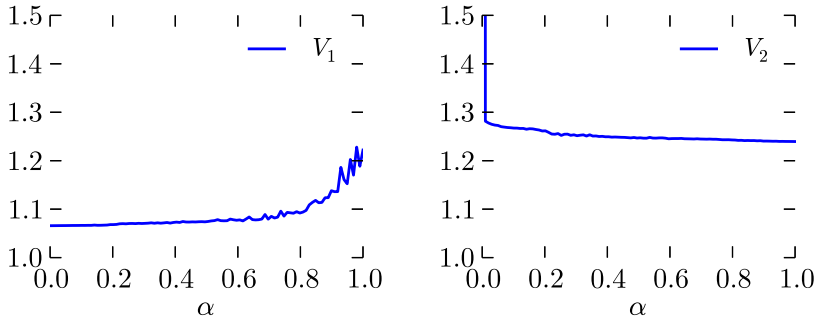

Figure 8.3: (left) Energy V_1, measuring uniformity on each shell, and (right) V_2, measuring uniformity of the set of directions as a whole. Energy evaluated for the optimum configurations, for various α. Except near 0 and 1, the solution does not much depend on the choice of α.

8.2.3 Incremental construction of an optimal arrangement

Some recent work on single shell acquisition design [Cook et al., 2007, Dubois et al., 2005, Deriche et al., 2009] are about the interest of incremental sampling sequences, for which an interruption at any point would result in an approximately optimal design. Such designs are useful to process data from prematurely aborted acquisitions, as well as to process data online (see Chapter 5, Section 5.2.2).

In the sequel we adapt the approach proposed in Deriche et al. [2009] to the problem of multiple q-shells design. To find a nearly optimal design for K points, we construct the point set incrementally: K iterations are required. At each iteration k, we first select the sphere s on which to add the k-th point. Then we find the direction $\mathbf{U}_{s,i}$ minimizing V, while the other directions remain fixed. The minimization at each iteration is done by an exhaustive search among a set of 10000 pseudo-random points uniformly distributed on each sphere. Therefore we construct a set of points, that remain nearly optimal throughout the acquisition sequence.

8.3 Geometrical properties of the multiple shell point sets

We present in this section some geometrical measures on the generated point sets, and compare to optimal configurations on the sphere. We also compare the incremental point sets configurations to the optimal configurations. The plots report the value of the electrostatic repulsion, per shell and as a whole. For an easier interpretation, we plot the so-called normalized electrostatic energy, which is the energy divided by the minimum electrostatic energy V^*, for the same number of points under consideration. In short, the closer to 1, the better.

8.3.1 Uniformity of each shell

We generated sampling protocols on $S = 2$, 3 and 4 shells, with the same number of points per shell, $K_s = 6 \dots 60$. We computed the average electrostatic energy on each shell V_1. We plot on Fig. 8.4 (right) the normalized energy V_1/V^*, where V^* is the electrostatic of the optimal configuration on a single sphere.

The ratio is very close to 1 for all considered values of s and K_s. This means that there is almost no price to pay on the uniformity per shell, to get a globally uniform configuration.

8.3.2 Uniformity of the sampling directions as a whole

With the same optimal sets of directions, we evaluate the angular uniformity of the sampling directions as a whole. We plot on Fig. 8.4 (right) the normalized energy V_2/V^*. Once again, the ratio is very close to 1. Surprisingly enough, as the number

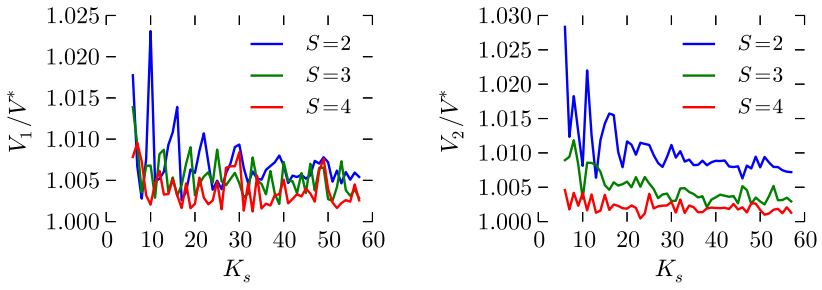

Figure 8.4: (left) normalized average energy per shell V_1. (right) normalized average energy of the sampling directions as a whole, V_2/V^*. The normalized energy are very close to 1 in all cases.

of shell increases, the constructed point sets becomes closer to the electrostatic optimum. This is somehow counter-intuitive, as the number of constraints increases with the number of shells.

8.3.3 Construction of incremental point sets

We also evaluate the geometrical properties of incrementally constructed multiple shell point sets. We report on Fig. 8.5 the normalized energy of the incremental configurations. We first note that the energy per shell remains very low, and close to the optimal. However, and in particular when the number of points per shell is moderate ($K_s \leq 20$), the energy as a whole is significantly higher, which is an index of a non-uniform configuration. We illustrate this on Fig. 8.6, where we plot the incrementally constructed point set and the optimal point set for $S = 2$ shells, and $K_s = 17$ points per shell. Therefore for a moderate sample size, it is probably better to start a scan with an optimal point sets. The scan can be further extended with the incremental construction.

With this method, we are therefore able to construct point set configurations on several spheres. The configuration on each shell, separately, is closely uniform and almost optimal with respect to the electrostatic repulsion criterion. Additionally, the set of directions, which is the set of all sampling points considered as a whole, is also uniform on the sphere, and almost optimal for the same energy. We now use these point sets as sampling protocols in q-space imaging, and compare their performance with radial sampling.

8.4 Experiments and results

We provide in this section an experimental validation of this approach. We test the sampling schemes in action, and evaluate the angular resolution of staggered

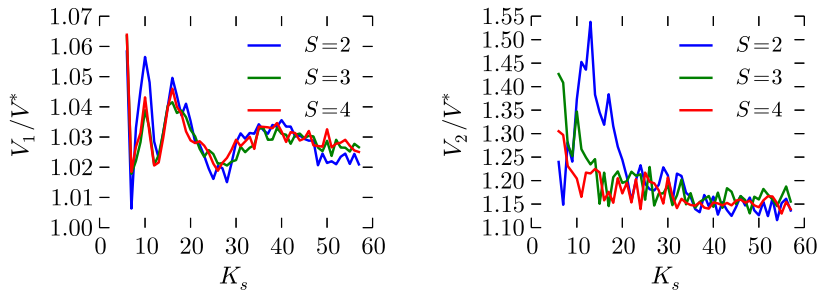

Figure 8.5: Geometrical properties of the incrementally constructed point sets on S shells. (left) Normalized average energy per shell V_1/V^*, of the incremental point set with K_s points per shell. (right) Normalize average energy of the sampling directions as a whole, V_2/V^*. The average energy per shell remains low, but the energy as a whole is significantly higher than for the optimal configurations.

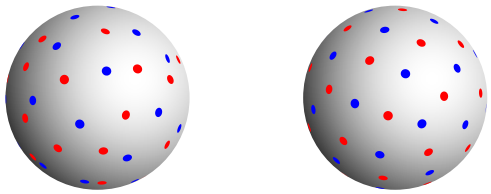

Figure 8.6: (left) incrementally constructed point set on $S = 2$ shells, $K_s = 17$ points per shell, and (right) optimal configuration for the same parameters. For such a small sample size, the incremental construction gives poorly uniform configurations.

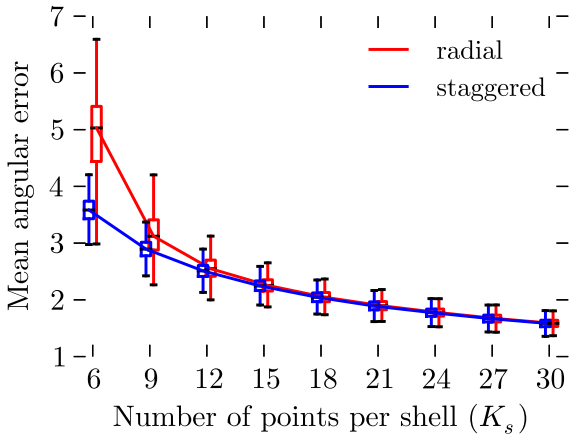

Figure 8.7: Average angular error between the principal direction of the estimated tensor and the axis of the cylinder. Signal simulation and reconstructed was repeated with 2000 different orientations, and 100 repetitions with random, Rician noise for each orientation. We plot here the median, first and third quartiles, and extremal values of the angular error (in degrees).

multiple q-shell, compared to radial sampling, for single fiber reconstruction and HARDI methods.

8.4.1 Single fiber compartment

We simulated a single fiber by a cylinder with impermeable wall. The diffusion signal was simulated following Soderman and Jonsson [1995]. The cylinder dimensions were set to $L = 5$ mm, and $\rho = 5$ µm; and the diffusion time is set to $\tau = 20.8$ ms. The signal is simulated for different acquisitions schemes, and corrupted by Rician noise, with corresponding SNR $= 25$ with respect to the baseline, non diffusion-weighted signal. From these noisy measurements, we fit a diffusion tensor model, using weighted linear least squares method (see Chapter 4, Section 4.2.2). This process is repeated 100 times for a given cylinder model, to get an estimate of the average angular error. Besides, to test the rotational invariance of acquisition schemes, this in turn is repeated 2000 times, for cylinders with different axis orientations. Acquisition protocols are defined on $S = 3$ shells in q-space, and the number of points per shell ranges from $K_s = 6$ to $K_s = 30$. Results of the average angular error are reported on Fig. 8.7.

As expected, the angular error decreases as the number of points per shell increases. The median angular error is smaller for the acquisition protocol we propose, as compared to radial sampling for the same total number of acquisitions. For a small number of points per shell, the angular error is decreased by 2°. Besides, the range of angular errors is smaller when considering tensors with different direc-

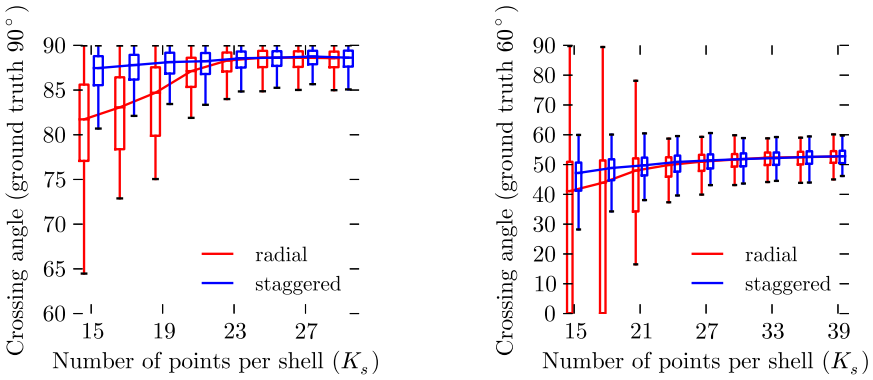

Figure 8.8: Crossing angle for a reconstructed fiber crossing. The q-space signal was reconstruction in the mSPF basis, with Laplace regularization as presented in Chapter 6, fixed regularization weight $\lambda = 0.5$. The ODF was further estimated using the SPFI method in Cheng et al. [2010a]. The boxplot represents min and max values, as well as the first and third quartiles.

tions on the sphere. This means that our proposed method gives a more precise reconstruction, and with a better rotational invariance than radial sampling.

8.4.2 Multi-fiber reconstruction

We also compare the accuracy of multiple fiber detection and discrimination with both sampling protocols. The signal is now simulated using a mixture of 2 Gaussian distributions, with equal compartment size. The corresponding diffusion tensors have a FA $= 0.7$ and a mean diffusivity $2.1 \cdot 10^{-3}\,\mathrm{mm \cdot s^{-1}}$. Two crossing angles are considered, for 90° and 60°. The signal is corrupted by Rician noise, with corresponding SNR $= 25$ with respect to the baseline, non diffusion-weighted signal. The signal is estimated in the mSPF basis (see Chapter 6), and the ODF in constant solid angle is estimated using the SPFI method in Cheng et al. [2010a]. The angular and radial truncation orders were set to $L = 6$ and $N = 2$, respectively. The maxima of the ODF are computed with a discrete search on a random set of 10000 points on the sphere, leading to an accuracy of 0.1°. The acquisition protocol was defined on $S = 3$ shells, and the number of points per shell K_s ranges from 15 to 40. Results of the reconstructed crossing angle are reported on Fig 8.8. When the number of maxima was not exactly 2 (in practice, either 1, 2 or 3 was observed), we set the angle to 0°. As for the previous experiments, the experiment was repeated 1000 times, with simulated Rician noise and random rotation of the fibers to test the rotational invariance of the reconstruction.

The accuracy of the reconstructed angle for fiber crossing increases with the number of acquisition directions. In particular, when the number of directions per

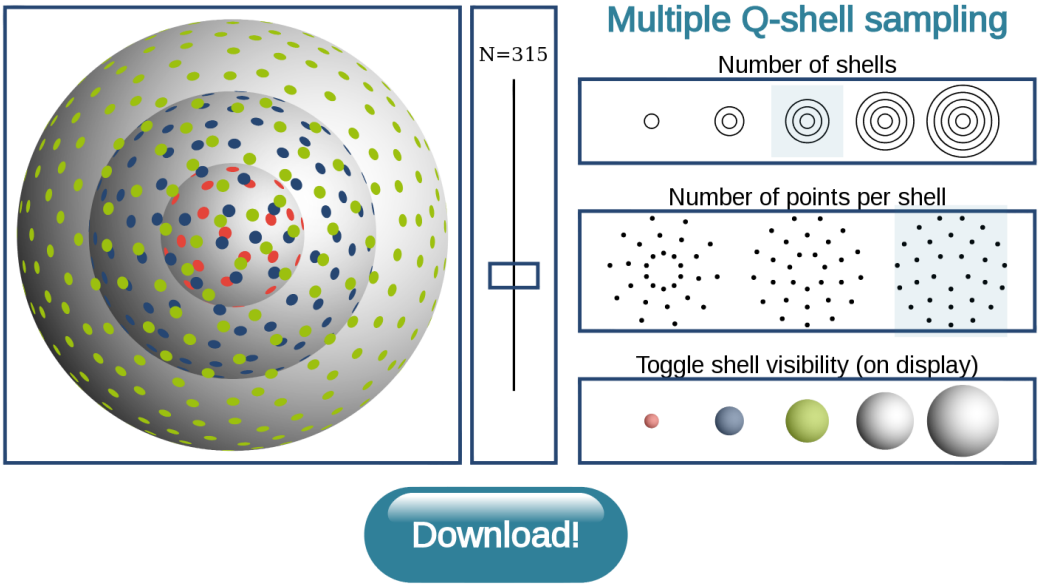

Figure 8.9: Web interface to download optimal configurations on several shells, available online here. The number of shells and number points per shell can be selected.

shell decreases, there is a clear advantage of our method with respect to radial sampling. Note that with both methods, the separation angle between fibers is slightly underestimated. This is a well-known limitation of most reconstruction techniques [Tournier et al., 2004, Schultz and Seidel, 2008, Jiao et al., 2011].

Software

The generated points sets can be generated and downloaded through an online web application, available on my website (see Fig. 8.9).

8.5 Conclusions

We have proposed a novel method to generate sampling schemes for multiple q-shell acquisitions. Our method is dedicated to the placement of acquisition directions on each sphere, with a good angular coverage per shell and as a whole. This is done through an energy minimization, which is an extension of the electrostatic repulsion to multiple shells. With an adequate minimization algorithm, we show that this energy can be used to create acquisition sequence with incremental angular coverage, that are compatible with aborted scans.

The geometrical properties of the generated point sets are satisfactory: the

angular coverage per shell is indeed very close to the optimal arrangements in q-ball imaging. This is also the case for the angular coverage as a whole. Tested in practice, for the reconstruction of single and multiple fiber compartments, this sampling strategies gives a better angular precision. Single fiber orientation is determined with a lower angular error, and the crossing angle in two fibers case is also more accurate.

Summary of the contributions of this chapter

- We present a novel method to generate sampling directions for multiple shells acquisition.
- The sampling protocols offers nearly optimal angular coverage per shell and globally.
- The angular reconstruction accuracy is improved with respect to radial sampling.
- The discrimination of fiber crossings is also improved.

Chapter 9

A Unified Approach to Experimental Design in parametric Diffusion MRI

Contents

Overview

Given a basis of functions to describe the diffusion signal, what is the best sampling strategy for an accurate estimation of the coefficients? Is there a means to minimize the condition number corresponding to the linear estimation system of coefficients in an orthonormal basis? Is this compatible with the previous chapter, where the motivation was purely geometrical? We propose a general method to design acquisition schemes with minimal condition number, for the reconstruction of coefficients in a given orthonormal basis. This method is detailed for the spherical harmonics in q-ball imaging, and related to the sampling theorems about sampling on the spheres. We also derive a method for quasi-optimal sampling in multiple q-shell, for the reconstruction in the mSPF basis, presented in this thesis.

Keywords Acquisition design; Condition number; Multiple q-shell acquisition; q-space imaging; q-ball imaging; harmonic analysis on the sphere.

9.1 Introduction

In the introduction of the previous chapter (see Chapter 8, Section 8.1), we have listed the various parameters that specify a multiple q-shell protocol. The remaining of the chapter was the description of a method to arrange sampling directions so that the angular coverage be uniform. In this chapter, we are interested in the relationship between the acquisition strategy, and the choice of a basis in parametric signal reconstruction.

The question of sampling efficiency has already been studied for parametric estimation in diffusion MRI. Beyond the geometrical approaches, for the reconstruction of diffusion tensor MRI, the noise performance has been studied through the minimization of the condition number [Papadakis et al., 1999, Skare et al., 2000]. In q-space MRI, several studies on multiple shell sampling [Caruyer et al., 2011a, Assemlal et al., 2009a, Ye et al., 2012, Daducci et al., 2011] focused on the efficiency of various sampling strategies. In particular, Assemlal et al. [2009a] studies the impact of radial and angular sampling on the condition number of the reconstruction problem in SPF basis, but they do not provide a method to systematically improve the noise performance. In Daducci et al. [2011], the sampling on several shells is investigated under the light of the novel sampling theorem on the sphere in McEwen and Wiaux [2011], which gives a minimum sampling rate to avoid aliasing in harmonic analysis on the sphere. However, as we show in this chapter, the number of points of the spherical sampling proposed in McEwen and Wiaux [2011] (and presented earlier in this thesis, in Chapter 5, Section 5.2.4) can be reduced for a given truncation order. Besides, as they use sampling on equiangular grids, there is no clue on angular uniformity of the proposed schemes.

In this chapter, we give a general method for optimal design of experiment in parametric signal reconstruction. We apply this to the optimal design in q-ball imaging, for the reconstruction in the truncated spherical harmonics basis, and compare to sampling theorem on the sphere. We also apply this to multiple q-shell experimental design, for the reconstruction in the mSPF basis we presented in this thesis (see Chapter 6). We compare each novel sampling strategy to state-of-the-art sampling, in terms of condition number and noise performance for the reconstruction.

9.2 Theory

In this section, we outline the general pipeline in parametric reconstruction of the diffusion signal, for 1D q-space, q-ball and 3D q-space diffusion MRI. Within this framework, we present a method based on the notion of cubature formula (the extension of quadrature formula to higher dimension) to create optimal design of experiments, with respect to the condition number associated to the problem of parameters estimation.

9.2.1 Parametric estimation of the diffusion signal

The quantity of interest in diffusion MRI is the ensemble average propagator (EAP) or the orientation distribution function (ODF), which are both related to the diffusion signal through linear continuous transforms (Fourier transform, Radon transform, etc.). Since then, a common approach is to first reconstruct the diffusion signal in a continuous basis of functions, then apply the transform of interest to each component of the signal to get the quantity of interest. Therefore the diffusion signal is approximated in a finite, orthonormal basis of functions

$$\forall \mathbf{q} \in \Omega, \qquad E(\mathbf{q}) = \sum_{i=1}^{R} c_i f_i(\mathbf{q}), \tag{9.1}$$

where $\Omega \subset \mathbb{R}^3$. Depending on the application, we have $\Omega = \mathbb{R}$ (1D diffusion signal), $\Omega = \mathcal{S}^2$ (q-ball imaging) or $\Omega = \mathbb{R}^3$ (q-space imaging).

Provided K measurements $y_k = E(\mathbf{q}_k)$ of the signal at wavevectors $\mathbf{q}_k$, the coefficients $\hat{c}_i$ are estimated by least squares. Put in matrix form, we write

$$\hat{\mathbf{c}} = (\mathbf{H}^{\mathrm{T}}\mathbf{H})^{-1}\mathbf{H}^{\mathrm{T}}\mathbf{y}. \tag{9.2}$$

$\mathbf{H}$ is the design matrix, and has entries $H_{ki} = f_i(\mathbf{q}_k)$.

9.2.2 Condition number

We present a general method to choose the sampling points $\mathbf{q}_k$ to optimize the noise performance. When the parameters are estimated through linear least squares, the

covariance matrix of the estimate is approximately equal to $\sigma^2(\mathbf{H}^{\mathrm{T}}\mathbf{H}))^{-1}$, where σ^2 is the variance of the measurements. The problem of optimal design is recast as an optimization problem, where we try to minimize a function of the covariance matrix, or equivalently of the information matrix $\mathbf{M} = 1/K\ \mathbf{H}^{\mathrm{T}}\mathbf{H}$, where K is the number of measurements.

A useful index for noise performance and stability of the reconstruction is the condition number $\kappa(\mathbf{M}) = \lambda_{\max}(\mathbf{M})/\lambda_{\min}(\mathbf{M})$ of the information matrix. The condition number is an upper bound to the relative error propagation from the measurements to the coefficients estimates,

$$\frac{||\Delta\mathbf{c}||/||\mathbf{c}||}{||\Delta\mathbf{y}||/||\mathbf{y}||} \leq \kappa(\mathbf{M}).$$

The optimal value of $\kappa(\mathbf{M})$ is 1, in which case the information matrix is proportional to the identity $\mathbf{I}_R$. We present here a systematic method to find a sampling scheme with minimal condition number.

9.2.3 Condition number and cubature formula

The coefficients of the information matrix M_{ij} can be interpreted as the approximation of the continuous dot product $\langle f_i, f_j \rangle$

$$M_{ij} = \frac{1}{K}\sum_{k=1}^{K} f_i(\mathbf{q}_k) f_j(\mathbf{q}_k) \approx \int_{\Omega} f_i(\mathbf{q}) f_j(\mathbf{q}) \mathrm{d}\Omega(\mathbf{q}) = \delta_{ij} \tag{9.3}$$

The basis is orthonormal, hence if this approximation is exact, $\mathbf{M} = \mathbf{I}_R$, and the associated condition number equals 1. This naturally introduces the notion of quadrature formula, and its generalization to higher dimension, called the cubature formula.

Definition 2. *A cubature formula for the integral* $\mathcal{I} = \int_{\Omega} g(\mathbf{q})\mathrm{d}\Omega(\mathbf{q})$ *is a collection of nodes* $\mathbf{q}_s$ *and weights* ω_s *such that*

$$\mathcal{I} = \sum_{s=1}^{S} \omega_s g(\mathbf{q}_s) \tag{9.4}$$

If such a cubature formula exists for the integral in Eq. 9.3, then we place the sampling points at nodes $\mathbf{q}_s$, and the number of repetitions K_s at node $\mathbf{q}_s$ is proportional to the weight ω_s. In the two next section, we present a method to generate sampling schemes with minimal condition number in parametric q-ball imaging (for reconstruction in spherical harmonics) and q-space imaging, for the reconstruction in mSPF basis.

9.3 Optimal design in q-ball imaging

In this section, we present a method to generate cubature formula for the spherical harmonic basis. We introduce the notion of spherical design, and present a method to generate spherical design with a uniform coverage on the sphere. We compare our approach to the sampling theorems on the sphere (see Chapter 5, Section 5.2.4), in terms of minimum number of points K for a given truncation order L of the spherical harmonics basis, and in terms of rotational invariance of the proposed schemes.

The real, symmetric spherical harmonic basis $\{Y_{lm}\}$ truncated to order L has dimension $R = (L+1)\cdot(L+2)/2$. Put back into the general framework presented in Section 9.2.2, we have $\Omega = \mathcal{S}^2$, and the basis functions are $f_i = Y_i$, where $i(l,m) = 1, 2, \ldots, R$ for $(l,m) = (0,0), (2,-2), \ldots, (L,L)$. The spherical harmonic basis is equivalent to the basis of harmonic polynomial of degree L on $\mathcal{S}^2$, for which cubature formulae exist and are called spherical design.

9.3.1 Spherical design

Definition 3. *A* spherical t-design *[Delsarte et al., 1977] is a sequence of K points $\mathcal{X} = (\mathbf{u}_k)$, $k = 1 \ldots K$ on the unit sphere, such that the integral of any polynomial $p(x,y,z)$ of degree at most t over the sphere is equal to the average value of the polynomial on $\mathcal{X}$:*

$$\frac{1}{K}\sum_{k=1}^{K} p(u_{k\mathrm{x}}, u_{k\mathrm{y}}, u_{k\mathrm{z}}) = \int_{\mathcal{S}^2} p(\omega)\mathrm{d}^2\omega. \tag{9.5}$$

As the diffusion signal is symmetric, a design $\mathcal{X}$ is optimal for the reconstruction in the truncated SH basis to order L if $\mathcal{X} \cup -\mathcal{X}$ is a spherical $2L$-design. Then the approximation in Eq. 9.3 is exact and $\kappa(\mathbf{M}) = 1$. In what follows, we explain how to construct such a sequence of points on the sphere.

9.3.2 Necessary conditions for a spherical design

For the construction of a spherical $2L$-design with antipodal symmetry, we rely here on the equivalence criterion in [Goethals and Seidel, 1981].

Theorem 2. *A set $\mathcal{X} = (\mathbf{u}_k)_{k=1\ldots N}$ is a spherical $2L$-design iff it verifies*

$$\forall \mathbf{x} \in \mathbb{R}^3,\ \frac{1}{K}\sum_{k=1}^{K}\langle \mathbf{x}, \mathbf{u}_k\rangle^{2L} = \left(\prod_{\ell=0}^{L-1}\frac{1+2\ell}{3+2\ell}\right)||\mathbf{x}||^{2L} \tag{9.6}$$

In the above theorem, Eq. 9.6 is a multivariate polynomial equality. This rewrites as a system of $(2L+1)\cdot(2L+2)/2$ non-linear, polynomial equations in

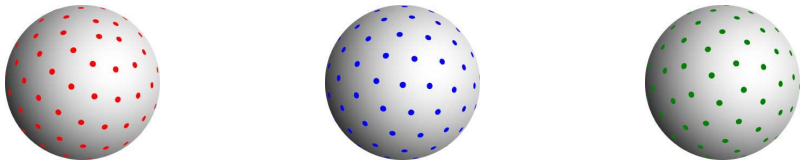

Geometric Electrostatic Optimal ($L = 4$)

Figure 9.1: Arrangements of $K = 50$ points on the unit sphere, (from left to right) geometric construction as in Koay [2011], minimum electrostatic configuration as in Jones et al. [1999b] and spherical design.

$(\mathbf{u}_k)_{k=1...K}$ to ensure coefficients equality of the left-hand and right-hand polynomials: $\forall a, b, c \in \mathbb{N}$ such that $a + b + c = 2K$,

$$\frac{(2L)!(1+2L)}{a!b!c!} \sum_{k=1}^{K} u_{kx}^a u_{ky}^b u_{kz}^c = \begin{cases} \dfrac{L!}{(a/2)!(b/2)!(c/2)!} & a,\ b \text{ and } c \text{ even}, \\ 0 & \text{otherwise.} \end{cases} \tag{9.7}$$

For a given order L, and a given number of samples K, we note by $\Omega_L^K \subset (\mathcal{S}^2)^K$ the feasible set $\{(\mathbf{u}_k)_{k=1...K}$ s.t. (9.7) is satisfied$\}$. As K increases, this set becomes a non-empty set, and infinitely many spherical designs exist. To constrain the sampling scheme to have a uniform coverage, we propose to minimize the electrostatic energy, while constraining the solution in Ω_L^K.

9.3.3 Spherical design with uniform density

In order to have a good rotational invariance, together with minimum condition number, we propose to minimize the modified electrostatic energy, under the constraint of being a spherical $2L$-design. The optimal point set is given by

$$\arg \min_{(\mathbf{u}_k) \in \Omega_L^N} \sum_{i \neq j} \frac{1}{||\mathbf{u}_i - \mathbf{u}_j||^2} + \frac{1}{||\mathbf{u}_i + \mathbf{u}_j||^2}. \tag{9.8}$$

This is a nonlinear optimization problem, with nonlinear equality constraints. However, both the objective function and the constraints are differentiable, and the derivatives have algebraic expressions. Therefore, we solve this problem by sequential quadratic programming, initialized with a uniform random population of points on the unit sphere. This method guarantees to find a local minimizer, provided that the feasibility set is not empty. By repeating the optimization several times, we increase the probability of finding a global optimum.

An example of optimal direction set for order $L = 4$ is presented on Fig. 9.1, and compared to a geometric [Koay, 2011] and an electrostatic [Jones et al., 1999b, Jansons and Alexander, 2003] arrangements of points.

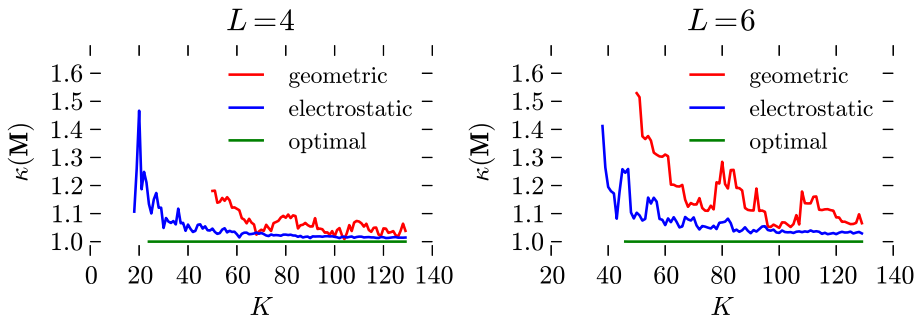

Figure 9.2: q-ball imaging: condition number of the information matrix corresponding to the truncated SH up to order $L = 4$ (left) and $L = 6$ (right), of the electrostatic, geometric and optimal point sets. The geometric configurations are only provided for $K \geq 50$, as this method is reported to be dedicated to large K by the author in [Koay, 2011]. Our proposed, optimal design is based on spherical design, and therefore exists for $K \geq 24$ at order $L = 4$, and for $K \geq 46$ at order $L = 6$ [Goethals and Seidel, 1981]. By construction, the condition number associated is exactly 1.

9.3.4 Comparison to conventional schemes in q-ball imaging

We first compare to conventional sampling strategies in q-ball, in terms of the condition number of the proposed scheme. Then we compare our approach more specifically to the sampling theorem on the sphere, putting the emphasis on the differences between the two approaches.

Condition number

We evaluate and report on Fig. 9.2 the noise performance of point sets generated with electrostatic analogy [Jones et al., 1999b, Jansons and Alexander, 2003] and by geometrical construction [Koay, 2011], for the reconstruction of SH coefficients of the diffusion signal. We compare these sampling methods to the proposed, optimal point set based on spherical design.

Sampling theorem on the sphere

Our approach, even derived with different motivations, is closely related to the sampling theorem on the sphere [McEwen and Wiaux, 2011]. This theorem gives an explicit construction of a sampling scheme on equiangular grid for an exact reconstruction of of band limited signals on the sphere. The sampling points are

Truncation order	Number of samples	
L	Sampling theorem	Spherical design
4	22	24
6	56	47
8	106	78
10	172	120

Table 9.1: Number of samples for an exact reconstruction of a band-limited signal on the sphere. We compare the novel sampling theorem in McEwen and Wiaux [2011] and our approach based on spherical designs.

defined by colatitude and longitude angles

$$\begin{aligned} \vartheta_t &= \frac{\pi(2t+1)}{2L-1}, \qquad t = 0, 1, \ldots, L-1 \\ \varphi_p &= \frac{2\pi p}{2L-1}, \qquad p = 0, 1, \ldots, 2L-2. \end{aligned}$$

The associated quadrature weights are derived in the article. The first comment on this method is that, being aligned on equiangular grid, the sample points form a poorly uniform coverage of the sphere. In particular, the sampling is sparser along the equator of the sphere, than about the poles. This is not desirable, as the true signal is in general not band-limited, and there exists a systematic approximation error when the signal is represented in the spherical harmonic basis. With no prior on this approximation error, it is better to place the points in a uniform fashion, for a better rotational invariance.

Besides, the number of points in this sampling theorem is $K = 2L^2 - 3L + 2$. This new result in McEwen and Wiaux [2011] improve on the previous findings of Driscoll and Healy [1994], in that they reduce the number of samples required for exact reconstruction. Concerning the spherical design, there is no general formula giving the minimum number of sampling points for a given truncation order. However, for several orders, spherical designs have been constructed (see for instance [Hardin and Sloane, 1996] and the authors' website.) and we report on Table 9.1 the associated number of measurements, as compared to the number of measurements of the sampling theorem. Except for the smallest truncation order $L = 4$, the method based on spherical designs gives sample schemes with significantly fewer measurements than this novel sampling theorem. We would like to mention that these approaches on sampling theorems also provide efficient methods for the computation of the spherical harmonic coefficients, as they target very high truncation orders (up to $L = 1024$). In diffusion MRI, as the truncation order is moderate (up

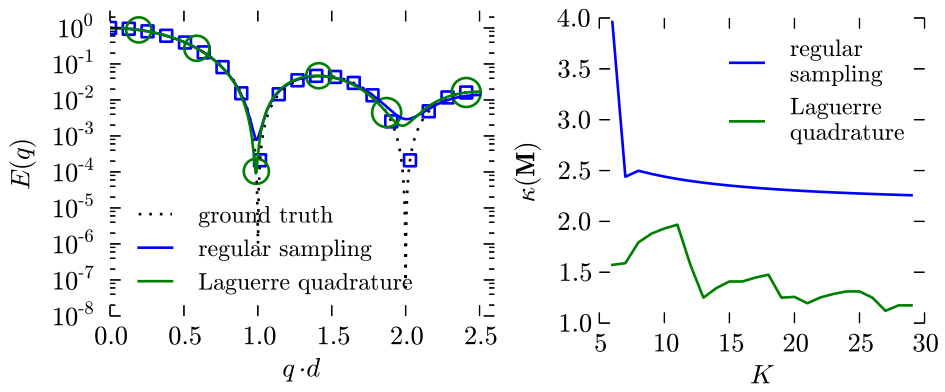

Figure 9.3: Evaluation of Gauss-Laguerre quadrature for one dimensional q-space. (Left) An example of signal and its reconstruction. The blue squares and the green circles represent the regular and quadrature samples respectively. The radii of the circles are proportional to the number of repeated acquisitions. (Right) Condition number of the information matrix.

to $L = 10$ reported in the literature), the reconstruction using the classical design matrix is efficient enough, and we are more concerned with the acquisition time, and therefore the number of measurements.

9.4 Optimal design in q-space imaging

Chapter 8 presents a method to place the sampling directions in a uniform fashion. We already pointed out the numerous parameters to be determined in a multiple q-shell protocol design (see Chapter 8, Section 8.1). Here we specify what should be the number of shells S, shell radii q_s, and the number of points per shell K_s, to minimize the condition number associated to the problem of estimating the coefficients in mSPF basis. To introduce the method, we first present a method for optimal design in one dimensional q-space MRI, for the reconstruction in a closely related basis.

9.4.1 Optimal design in one dimensional q-space MRI

The simple harmonic oscillator basis for the reconstruction of real diffusion signal in one dimension [Ozarslan et al., 2008] is given by $\Phi_i(q,u) = \kappa_i(u)\exp(-2\pi^2q^2u^2)L_i^{-1/2}(4\pi^2q^2u^2)$, where u is a characteristic length, $L_i^{-1/2}$ the generalized Laguerre polynomial of degree i and $\kappa_i(u)$ a normalization constant.

Put back into the general framework presented in Section 9.2.2, we have $\Omega = \mathbb{R}$, and the basis functions are $f_i = \Phi_i$. For the evaluation of the dot product in Eq. 9.3,

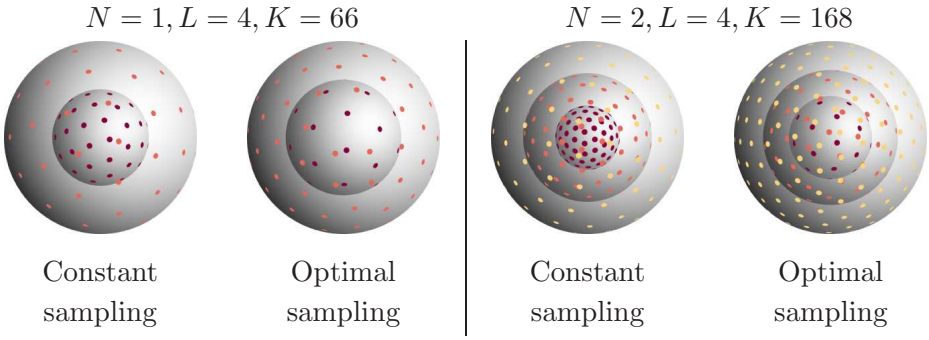

Figure 9.4: 2-shell (left) and 3-shell (right) acquisition protocols: regular multiple q-shell with constant number of points per shell, and optimal arrangement with minimal condition number for reconstruction in SPF basis.

we use the substitution $x = 4\pi^2 q^2 u^2$, so that

$$\langle \Phi_i, \Phi_j \rangle = 2\pi u \kappa_i(u) \kappa_j(u) \int_0^\infty L_i^{-1/2}(x) L_j^{-1/2}(x) x^{-1/2} e^{-x} \mathrm{d}x. \tag{9.9}$$

When the basis is truncated to order N, the evaluation of Eq. 9.9 reduces to the problem of Gauss-Laguerre quadrature [Abramowitz and Stegun, 1970]. The optimal samples are $q_s = \sqrt{x_s}/2\pi u$, with K_s repetitions, where K_s is proportional to $x_s e^{x_s}/[L_N^{-1/2}(x_s)]^2$ and the nodes $x_s, s = 1 \ldots N+1$ are the roots of $L_{N+1}^{-1/2}$.

To show the feasibility of one dimensional q-space signal reconstruction from a set of measurements on a limited support size, we compare the Gauss-Laguerre quadrature to a regular sampling on the range $[0, q_{\max}]$. We plot on Fig. 9.3 an example of reconstruction of a diffusion signal corresponding to the restricted diffusion between two parallel planes, separated by distance d [Ozarslan et al., 2008]. The truncation order in the basis was set to $N = 5$, and the corresponding Gauss-Laguerre quadrature works on 6 nodes. The result for a total of 20 acquisitions is visually identical to the reconstruction from a regular sampling. Besides, the associated information matrix is better conditioned for the quadrature sampling. The reason why the condition number is not exactly 1 in this case is that the quadrature weight ω_s is approximated by the number of repetitions at node q_s, which is an integer.

9.4.2 Optimal design in q-space imaging

The truncated spherical polar Fourier (SPF) basis [Assemlal et al., 2009b] is able to represent the diffusion signal in the whole q-space. To represent a continuous signal, which verifies $E(\mathbf{0}) = 1$, we have proposed in this thesis a modified version of the SPF basis (see Chapter 6). We reconstruct the signal as $E(q \cdot \mathbf{u}) = \exp(-q^2/2\zeta) +$

$\sum_{nlm} a_{nlm} C_{nlm}(q \cdot \mathbf{u})$. The basis functions are $C_{nlm}(q \cdot \mathbf{u}) = F_n(q) Y_{lm}(\mathbf{u})$, with

$$F_n(q) = \chi_n \frac{q^2}{\zeta} \exp\left(-\frac{q^2}{2\zeta}\right) L_n^{5/2}\left(\frac{q^2}{\zeta}\right), \tag{9.10}$$

ζ is a scale factor, χ_n a normalization constant, and Y_{lm} is the real spherical harmonic function. When the radial and angular truncation orders are N and L, respectively, this basis has dimension $R = N \cdot (L+1) \cdot (L+2)/2$. Put back into the general framework presented in Section 9.2.2, we have $\Omega = \mathbb{R}^3$, and the basis functions are $f_i = C_i$, where $i(n,l,m) = 1, 2, \ldots, R$ for $(n,l,m) = (0,0,0), (0,2,-2), \ldots, (N,L,L)$.

For the construction of an optimal design for this basis, we build on the findings of the previous two sections. We show that the radial part of the integral in Eq. 9.3 reduces to a Gauss-Laguerre quadrature problem, while the angular part reduces to a spherical design problem.

Therefore we propose a design on $N+1$ spheres in the q-space. The shell s has radius $q_s = \sqrt{\zeta x_s}$, where x_s is the s^{th} root of $L_{N+1}^{5/2}$. The number of points K_s on shell s should be proportional to $\omega_s = \exp(-x_s)/[x_s (L_N^{5/2}(x_s))^2]$ Finally, the points on each sphere should form a spherical $2L$-design. Example of points sets generated with this method are depicted on Fig. 9.4. They are compared to multiple shell sampling where the shell radii are evenly spaced, and the number of points equal on each shell, as suggested in [Assemlal et al., 2009a].

9.4.3 Multiple q-shell and three dimensional signal reconstruction

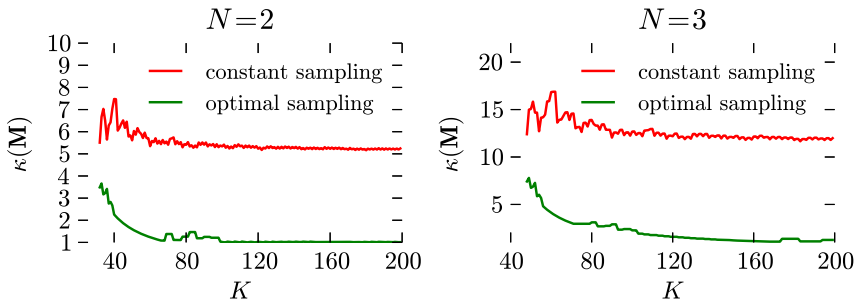

Figure 9.5: Condition number of multiple shell sampling, corresponding to the mSPF basis.

Using the results on Gauss-Laguerre quadrature and spherical designs, we generated optimal sampling schemes on multiple shells for the reconstruction in the SPF basis. We compare this to the sampling strategy with shell radii evenly spaced and constant number of points per shell proposed in [Assemlal et al., 2009a]. The condition number for the reconstruction in SPF basis is reported on Fig. 9.5.

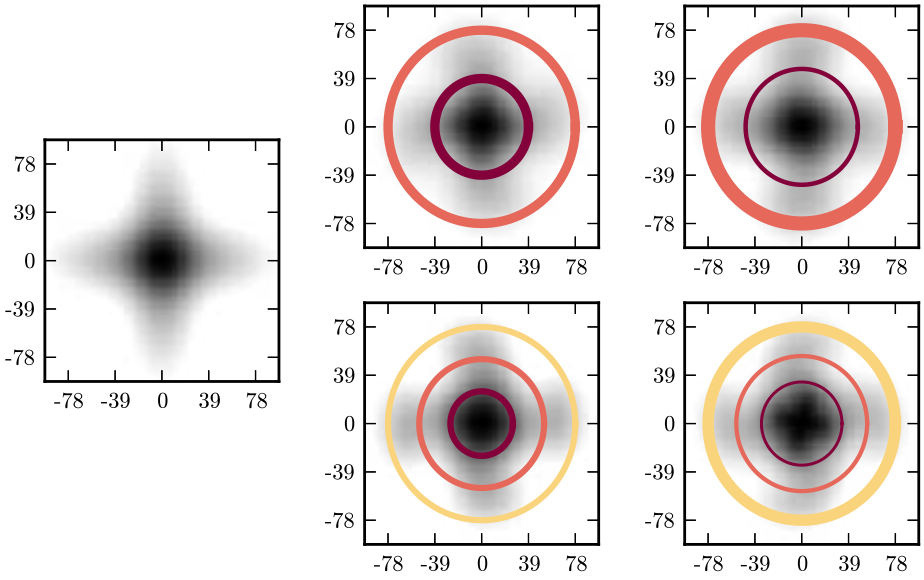

Figure 9.6: 2 shell (top) and 3 shell (bottom) sampling in action, for the reconstruction of a synthetic diffusion signal corresponding to a mixture of Gaussian, simulating fiber crossing. The circles represent the sampling shells, and the line widths are proportional to the number of points per shell.

We also simulate both methods, for the sampling and reconstruction of a synthetic diffusion signal corresponding to a mixture of Gaussian. Visual reconstruction is reported on Fig. 9.6, and quantitative comparison on Fig. 9.7.

9.5 Conclusion

In this chapter, we develop a computational framework for optimal design of experiment in diffusion MRI. For the reconstruction of a signal on a sphere, and a 3D signal, we propose sampling scheme with minimal condition number, for the parametric estimation of the signal in the spherical harmonic basis, and in the modified spherical polar Fourier basis. The angular uniform approach presented in the previous chapter is used to further constrain the solution to the condition number minimization problem. In this way, among all sampling configurations with minimum condition number, we retain the one that is most uniform. These sampling schemes also allow exact reconstruction of band-limited signals in these bases. Monte-Carlo simulations show that the signal to noise ratio of the parameters estimated from our optimal sampling scheme is improved with respect to conventional sampling scheme, for the same number of acquisitions.

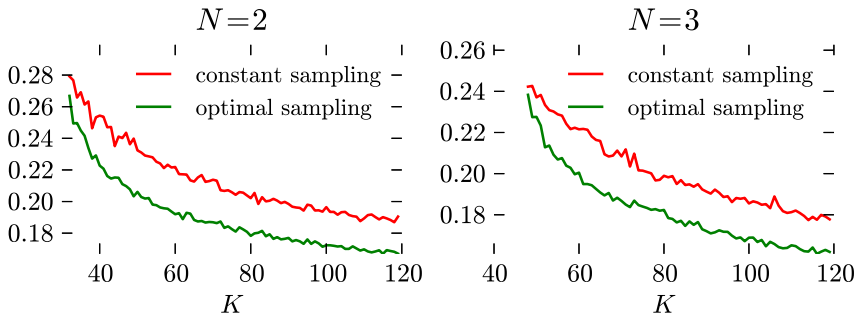

Figure 9.7: Mean squared error for a synthetic diffusion signal corresponding to a mixture of Gaussian, with Rician noise (SNR=25).

As a conclusion to this study, we claim that a sampling method is optimal for a reconstruction in a given basis and a given order. This means that in addition to the technical and physical limitations of the imaging system, the choice of the type of reconstruction and the angular uniformity of the sampling scheme must be taken into account when designing the acquisition protocol.

Summary of the contributions of this chapter

- We present a method to generate sampling directions that minimize the condition number for the parametric estimation problem in spherical harmonics and modified spherical polar Fourier bases.
- Provided that the number of measurements is large enough, we have an exact reconstruction of band-limited signals in the spherical harmonics and spherical polar Fourier bases.
- In the case of spherical harmonics, the minimum number of measurements is reduced with respect to conventional sampling theorems on the sphere on equiangular grids.
- This method, combined with the angular uniform approach of the previous chapter, provides sampling schemes that are also nearly uniform.

Part IV

Conclusion

Chapter 10

Conclusions and Perspectives

Contents

10.1 General conclusion

We have presented in this thesis several contributions related to the signal acquisition in diffusion MRI, and the estimation of local diffusion information from the MR signal attenuation in PGSE experiments. This work brings new mathematical methods for the parametric representation of the signal in a basis of continuous functions, and its reconstruction from noisy, discrete measurements. The method for discrete sampling is also investigated, in relation to this parametric estimation problem to gain maximum information from a given number of samples, to achieve the best possible reconstruction. Therefore we have covered the whole pipeline, from acquisition sequence design, to the reconstruction of the diffusion propagator and its derived characteristics.

10.1.1 Local diffusion estimation: evil is in the details

In conclusion to the estimation and reconstruction contributions, we would like to emphasize how the mathematical formulation of the problem is important, from a theoretical and a practical point of view. The definition of a basis of continuous functions in Chapter 6 has permitted the estimation of a continuous signal directly from the measurements, with no additional constraint to impose. We are also able to represent the Laplace regularization penalty in a simple quadratic form, and therefore this leads to an efficient estimation scheme with analytical solution. In practice, this has also significantly reduced the dimension of the basis, and therefore the computational cost and the demand in storage capacity, for the same power of description.

10.1.2 Guidelines for multiple q-shell experiment design

In this general conclusion, we would also like to come back to the two contributions related to multiple q-shell sampling. These contributions have been presented in two separate chapters: Chapter 8 presents a general-purpose method to define sampling schemes on several shells, that uniformly span the space of directions; Chapter 9 presents an approach to get sampling schemes that minimize the condition number for the reconstruction in a given parameterization. We would like to emphasize that these two contributions are directed towards the same goal, achieving the best possible reconstruction for a given acquisition time, and they are complementary to each other. Indeed, the optimal design problem, when trying to minimize the condition number, often leads to an under-constrained optimization and possibly many optimal configurations. Among all these configurations, we are interested in the one that has best angular coverage, and this is possible please to the approach in Chapter 8, in conjunction with this minimal condition number criterion.

10.2 Applications and Collaborations

The findings and contributions of this thesis have already opened the way to fruitful contributions in the Athena team and with our partners. We would like to mention some of these contributions, or application of our methods.

10.2.1 Angular-uniform multiple q-shell design

The contribution on the angular-uniform multiple q-shell has been used and compared to other approaches in Merlet et al. [2011] for the reconstruction of the diffusion signal under sparse constraints, using the so-called compressed sensing technique. Merlet et al. concluded that the uniform-angular sampling was useful and performed better than other sampling strategies for the reconstruction of the MR signal with under-sampled measurements, under a sparsity constraint. Besides, the script to generate and download the sampling schemes has been online on my website for a year, and is used by several groups, in particular our partners at the Center for Magnetic Resonance Research, University of Minnesota, for their routine acquisitions.

10.2.2 Parametric dictionary learning

The modified spherical polar Fourier basis (see Chapter 6) has been used to learn and design a novel parametric dictionary from a training set of samples. This is an ongoing work, which has been used in a proposal for the recent HARDI Contest, organized at the International Symposium on Biomedical Imaging, 2012 [Merlet et al., 2012]. The dictionary was used to reconstruct the ODF from a q-ball sampling on 15 points. The results are pretty good and promising, and comparable to other approaches taking much more samples.

10.3 Future work

In continuation to the work we have done during this thesis, we would like to continue developing acquisition methods and investigate the link between diffusion signal and tissue microstructure. In particular, the fine characterization of tissue microstructure information, such as axon diameters or axon density, is a topic that we have not explored during this thesis, but would like to work on in the near future. One of the physical aspect of the acquisition sequence that can help is the form and length of the diffusion gradient pulses. In particular, considering the true relationship between the diffusion signal attenuation and the diffusion propagator, which is no longer a Fourier transform when the narrow-pulse condition is not met, can help in designing novel acquisition methods.

At the same time, we are also interested in the clinical applications and clinical research in diffusion MRI. We believe, from the discussions with our colleagues in strong interaction with medical doctors, and from our readings, that there is still a huge gap between the state-of-the-art methodological approaches in estimation, modelling, reconstruction and analysis in one hand, and clinical applications *in situ* in the other hand. This is because clinical scanners have their limitations, because children and patients with severe neurological disorders can barely sustain acquisitions for a long time. These are probably the constraints we should take into account first in developing new methods to help diagnosis. Therefore all the theoretical aspects to reduce acquisition time, to simplify data processing, and finally ease the diagnosis are of utmost interest to us.

Chapter 11

Conclusions (en français)

Contents

11.1 Conclusion générale

Nous avons présenté dans cette thèse plusieurs contributions pour l'acquisition et la reconstruction du signal en IRM de diffusion, et pour l'estimation des paramètres locaux de diffusion à partir de l'atténuation du signal dans une séquence à écho de spin et impulsion de gradients. Cette thèse apporte des méthodes mathématiques innovantes pour la représentation paramétrique du signal dans une base de fonctions continues, et sa reconstruction à partir de mesures discrètes et bruitées. Le protocole d'échantillonnage est également étudié, en relation avec cette approche paramétrique, afin d'obtenir le maximum d'information possible des mesures, pour un temps d'acquisition donné, et ainsi obtenir la meilleure reconstruction possible. Nous pensons avoir exploré les principales étapes du processus d'acquisition et de reconstruction, présenté dans l'introduction (Fig. 2.1) : depuis l'élaboration des protocoles d'acquisition, à la reconstruction du propagateur moyen de diffusion et ses caractéristiques dérivées.

11.1.1 Estimation locale de la diffusion: le diable se cache dans les détails

En conclusion de nos contributions sur l'estimation et la reconstruction locale, nous aimerions souligner combien la modélisation et le choix des outils mathématiques est important, aussi bien d'un point de vue théorique qu'en pratique. La définition d'une base de fonctions continue dans le Chapitre 6 a permis d'estimer un signal continu, directement depuis les mesures discrètes, bruitées, sans avoir à imposer de contrainte supplémentaire. Nous pouvons également dériver l'opérateur de régularisation basé sur le Laplacien du signal, qui s'exprime en fonction des coefficients comme une simple forme quadratique. Ceci permet de résoudre le problème d'estimation sous contrainte de régularité de façon analytique. En pratique, cette nouvelle base a également permis de réduire de façon significative la dimension de l'espace des paramètres, et ainsi de diminuer la complexité des algorithmes de reconstruction, et de compresser les données, pour décrire exactement la même famille de signaux.

11.1.2 Mode d'emploi de l'échantillonnage en Fourier

Nous aimerions également revenir dans cette conclusion générale sur nos contributions liées aux protocoles d'acquisition sur plusieurs sphères dans l'espace de Fourier. Nous avons présenté ces deux contributions dans deux chapitres séparés : le Chapitre 8 présente une méthode générale pour élaborer des protocoles d'échantillonnage sur plusieurs sphères, en faisant en sorte d'optimiser la couverture angulaire ; par ailleurs, le Chapitre 9 présente une méthode systématique de minimisation du nombre de conditionnement, associé au problème de l'estimation

paramétrique dans une base donnée. Nous voudrions souligner encore une fois que ces deux contributions sont complémentaires, mais surtout répondent à un objectif unique, celui d'obtenir la meilleure reconstruction possible, pour un temps d'acquisition donné. En effet, le problème de minimisation du nombre de conditionnement admet généralement une infinité de solutions. Parmi toutes ces solutions, nous proposons de retenir celle qui offre la meilleure couverture angulaire, à la lumière des résultats que nous avons montrés dans le Chapitre 8. Comme nous l'avons présenté, cela est rendu possible en minimisant l'énergie électrostatique généralisée à plusieurs sphères, sous contrainte de vérifier les conditions pour minimiser le nombre de conditionnement.

11.2 Applications des méthodes, et collaborations

les contributions présentées dans cette thèse ont permis d'ouvrir la voie à plusieurs travaux en collaboration avec nos collègues de l'équipe-projet Athéna, ainsi que avec nos partenaires. Nous aimerions présenter deux de ces travaux en commun, ainsi que des applications de nos méthodes.

11.2.1 Échantillonnage à répartition angulaire uniforme

L'approche permettant de générer des schémas d'échantillonnage à couverture angulaire uniforme a été utilisée et comparée à d'autres approches dans Merlet et al. [2011], pour la reconstruction du signal de diffusion sous contrainte de parcimonie, en utilisant le *compressed sensing*. Merlet et al. concluent que la méthode répartissant les points de façon uniforme donne de meilleurs résultats que d'autres stratégies d'échantillonnage. Par ailleurs, le script permettant de générer et de télécharger des schémas d'échantillonnage suivant notre méthode est en ligne depuis un an maintenant, et est régulièrement utilisé par plusieurs groupes, notamment par nos partenaires au *Center for Magnetic Resonance Research*, à l'Université du Minnesota, pour leurs acquisitions en IRM de diffusion.

11.2.2 Apprentissage de dictionnaire paramétrique

La basee de Fourier sphérique modifiée, présentée dans le Chapitre 6, a été utilisée pour créer un dictionnaire par apprentissage sur un jeu de données. C'est un travail en cours, que nous avons utilisé pour participer au concours de reconstruction de modèles de diffusion à haute résolution angulaire, organisé à l'occasion de la conférence *International Symposium on Biomedical Imaging*, 2012 [Merlet et al., 2012]. Nous avons utilisé le dictionnaire pour reconstruire la fonction de distribution d'orientation à partir d'un échantillonnage sphérique sur seulement 15 points.

Les résultats sont plutôt encourageants, et se comparent bien aux autres approches, qui travaillent avec beaucoup plus d'échantillons.

11.3 Perspectives

Nous envisageons de poursuivre ce travail que nous avons fait et présenté dans cette thèse, et continuerons à développer des méthodes d'acquisition pour étudier le lien entre le signal de diffusion et la microstructure des tissus. En particulier, nous sommes intéressés à la possibilité de pouvoir remonter à des informations détaillées sur la structure fine des tissus dans la matière blanche, en particulier le diamètre des axones ou encore la densité des fibres au sein d'un faisceau. Nous pensons qu'un des paramètres des séquences d'acquisition pouvant aider à cela est la forme et la durée des impulsions de gradients. Prendre en compte un modèle plus précis du lien entre signal de diffusion et propagateur, qui n'est pas exactement une relation de Fourier, pourrait permettre de créer de nouvelles techniques d'acquisition.

Nous sommes également fortement intéressés par les applications cliniques de l'IRM de diffusion. Pour avoir longuement discuté de ces problèmes avec d'autres collègues, en relation directe avec des médecins et partenaires hospitaliers, nous croyons qu'il y a encore un fossé (voire un canyon !) à combler entre les nouvelles approches méthodologiques pour l'estimation, la modélisation, la reconstruction et l'analyse d'une part, et les applications cliniques *in situ* d'autre part. Les scanners cliniques ont malheureusement leurs limitations, mais aussi les patients et les enfants qui souffrent de maladies neurologiques peuvent difficilement rester longtemps dans le scanner sans bouger. Ce sont probablement ces contraintes qu'il faut considérer en priorité lorsqu'il s'agit de développer de nouvelles méthodes pour l'aide au diagnostique. En ce sens, toutes les approches théoriques qui permettent de réduire les temps d'acquisitions, de simplifier le traitement des données et finalement d'apporter de nouveaux outils pour le diagnostique vont dans le bon sens, et sont les directions vers lesquelles nous souhaitons nous diriger.

Appendix A

Publications of the author

Journal Publications

Emmanuel Caruyer, Rachid Deriche. Diffusion MRI Signal Reconstruction with Continuity Constraint and Optimal Regularization. *Medical Image Analysis*. Elsevier, 2012, In press.

Emmanuel Caruyer, Iman Aganj, Christophe Lenglet, Guillermo Sapiro, Rachid Deriche. Motion detection in diffusion MRI via online ODF estimation. *International Journal of Biomedical Imaging*, Hindawi, 2012, submitted.

Emmanuel Caruyer, Christophe Lenglet, Guillermo Sapiro, Rachid Deriche. Design of multi-shell sampling schemes with uniform coverage in diffusion MRI. *Magnetic Resonance in Medicine*, Wiley, 2012, submitted.

Conferences and Workshops with Proceedings

Emmanuel Caruyer, Rachid Deriche. Optimal Regularization for MR Diffusion Signal Reconstruction. *ISBI - 9th IEEE International Symposium on Biomedical Imaging*, May 2012, Barcelona, Spain.

Emmanuel Caruyer, Jian Cheng, Christophe Lenglet, Guillermo Sapiro, Tianzi Jiang, Rachid Deriche. Optimal Design of Multiple Q-shells experiments for Diffusion MRI. *MICCAI Workshop on Computational Diffusion MRI - CDMRI'11*, Sep 2011, Toronto, Canada.

Emmanuel Caruyer, Iman Aganj, Christophe Lenglet, Guillermo Sapiro, Rachid Deriche. On Line Reconstruction and Motion Detection in HARDI, *19th ISMRM annual meeting*, May 2011, Montréal, Canada.

Emmanuel Caruyer, Iman Aganj, Ryan Muetzel, Christophe Lenglet, Guillermo Sapiro, Rachid Deriche. Online orientation distribution function reconstruction in constant solid angle and its application to motion detection in HARDI. *ISBI - International Symposium on Biomedical Imaging: From Nano to Macro*, Apr 2010, Rotterdam, Netherlands.

Emmanuel Caruyer, Rachid Deriche. Adaptive Design of Sampling Directions in Diffusion Tensor MRI and Validation on Human Brain Images. *MICCAI Workshop on Diffusion Modelling and the Fiber Cup*, Sep 2009, Londres, United Kingdom.

Sylvain Merlet, **Emmanuel Caruyer**, Rachid Deriche. Parametric Dictionary Learning for Modeling EAP and ODF in Diffusion MRI *MICCAI 2011*, Sep 2011, Toronto, Canada. Springer, 6891, pp. 113-121, Lecture Notes in Computer Science.

Bibliography

Milton Abramowitz and Irene A. Stegun. *Handbook of mathematical functions*. Dover, 1970.

I. Aganj, C. Lenglet, G. Sapiro, E. Yacoub, K. Ugurbil, and N. Harel. Reconstruction of the ODF in single and multiple shell q-ball imaging within constant solid angle. *Magn. Reson. Med.*, 64(2):554–566, 2010a.

I. Aganj, C. Lenglet, G. Sapiro, E. Yacoub, K. Ugurbil, and N. Harel. Reconstruction of the ODF in single and multiple shell q-ball imaging within constant solid angle. *Magn. Reson. Med.*, 64(2):554–566, 2010b.

M Aksoy, C Forman, M Straka, S Skare, S Holdsworth, J Hornegger, and R Bammer. Real-time optical motion correction for diffusion tensor imaging. *Magn. Reson. Med.*, 2011. in press, DOI:10.1002/mrm.22787.

D.C. Alexander, G.J. Barker, and S.R. Arridge. Detection and modeling of non-gaussian apparent diffusion coefficient profiles in human brain data. *Magnetic Resonance in Medicine*, 48(2):331–340, 2002.

A. A. Alhamud, A. Hess, M. D. Tisdall, E. M. Meintjes, and A. J. van der Kouwe. Implementation of real time motion correction in diffusion tensor imaging. In *19th ISMRM*, Montréal, Canada., May 2011.

A.W. Anderson. Measurements of fiber orientation distributions using high angular resolution diffusion imaging. *Magnetic Resonance in Medicine*, 54:1194–1206, 2005.

Yaniv Assaf, Tamar Blumenfeld-Katzir, Yossi Yovel, and Peter J Basser. Axcaliber: a method for measuring axon diameter distribution from diffusion mri. *Magnetic Resonance in Medicine*, 59(6):1347–54, 2008.

H.-E. Assemlal, D. Tschumperlé, and L. Brun. Efficient computation of pdf-based characteristics from diffusion mr signal. In *MICCAI*, pages 70–78, Berlin, Heidelberg, 2008. Springer-Verlag. ISBN 978-3-540-85989-5.

H-E. Assemlal, David Tschumperlé, and Luc Brun. Evaluation of q-space sampling strategies for the diffusion magnetic resonance imaging. In *MICCAI*, London/England, 2009a.

Haz-Edine Assemlal, Jennifer Campbell, Bruce Pike, and Kaleem Siddiqi. Apparent intravoxel fibre population dispersion (fpd) using spherical harmonics. In Gabor

Fichtinger, Anne Martel, and Terry Peters, editors, *Medical Image Computing and Computer-Assisted Intervention – MICCAI 2011*, volume 6892 of *Lecture Notes in Computer Science*, pages 157–165. Springer Berlin / Heidelberg, 2011.

H.E. Assemlal, D. Tschumperlé, and L. Brun. Efficient and robust computation of pdf features from diffusion MR signal. *Medical Image Analysis*, 13(5):715–729, 2009b.

A. Barmpoutis, B. C. Vemuri, and J. R. Forder. Registration of high angular resolution diffusion MRI images using 4th order tensors. In *MICCAI*, pages 908–915, Berlin, Heidelberg, 2007. Springer-Verlag. ISBN 3-540-75756-2, 978-3-540-75756-6.

Peter J. Basser, James Mattiello, and Denis Lebihan. MR Diffusion Tensor Spectroscopy and Imaging. *Biophysical Journal*, 66:259–267, 1994a.

Peter J. Basser, Jim Mattiello, and Denis Le Bihan. Estimation of the effective self-diffusion tensor from the nmr spin echo. *Journal of Magnetic Resonance*, B (103):247–254, 1994b.

P.J. Basser, S. Pajevic, C. Pierpaoli, J. Duda, and A. Aldroubi. In vivo fiber tractography using DT-MRI data. *Magnetic Resonance in Medicine*, 44:625–632, 2000.

M. Basseville and A. Benveniste. Design and comparative study of some sequential jump detection algorithms for digital signals. *ASSP*, 31:521–535, 1983.

M. Basseville and A. Benveniste. *Detection of abrupt changes in signals and dynamical systems*. Lecture Notes in Control and Information Sciences. Springer-Verlag, 1984.

M. Basseville and I. V. Nikiforov. *Detection of abrupt changes: theory and application*. Prentice-Hall, Inc., Upper Saddle River, NJ, USA, 1993.

S Basu, P T Fletcher, and R T Whitaker. Rician noise removal in diffusion tensor mri. In *MICCAI*, pages 117–125, 2006.

F. Bloch. Nuclear induction. *Physical Review*, 70:460–474, 1946.

P. T. Callaghan. *Principles of Nuclear Magnetic Resonance Microscopy*. Oxford: Clarendon, 1991a.

P. T. Callaghan. *Principles of nuclear magnetic resonance microscopy*. Oxford University Press, Oxford, 1991b.

Herman Y. Carr. Field gradients in early mri. *Physics Today*, 57(7), July 2004.

Emmanuel Caruyer, Jian Cheng, Christophe Lenglet, Guillermo Sapiro, Tianzi Jiang, and Rachid Deriche. Optimal design of multiple q-shells experiments for diffusion mri. In *MICCAI Workshop on Computational Diffusion MRI - CDMRI'11*, Toronto, Canada, September 2011a.

Emmanuel Caruyer, Christophe Lenglet, Guillermo Sapiro, and Rachid Deriche. Incremental gradient table for multiple q-shells diffusion mri. In *HBM 17th Annual Meeting*, Québec, Canada, June 2011b.

T.F. Chan and J. Shen. *Image Processing and Analysis - Variational, PDE, wavelet, and stochastic methods*. SIAM, Philadelphia, 2005.

Jian Cheng, Aurobrata Ghosh, Tianzi Jiang, and Rachid Deriche. A riemannian framework for orientation distribution function computing. In *Medical Image Computing and Computer Assisted Intervention (MICCAI)*, September 2009.

Jian Cheng, Aurobrata Ghosh, Rachid Deriche, and Tianzi Jiang. Model-free, regularized, fast, and robust analytical orientation distribution function estimation. In *Medical Image Computing and Computer-Assisted Intervention - MICCAI*, volume 6361 of *Lecture Notes in Computer Science*, pages 648–656. Springer, 2010a.

Jian Cheng, Aurobrata Ghosh, Tianzi Jiang, and Rachid Deriche. Model-free and analytical eap reconstruction via spherical polar fourier diffusion mri. In *Medical Image Computing and Computer-Assisted Intervention - MICCAI*, volume 6361, pages 590–597, 2010b.

Jian Cheng, Tianzi Jiang, and Rachid Deriche, Dr. Theoretical analysis and practical insights on eap estimation via a unified hardi framework. In *MICCAI Workshop on Computational Diffusion MRI*, Toronto, Canada, September 2011.

S Cluskey and D B Ramsden. Mechanisms of neurodegeneration in amyotrophic lateral sclerosis. *Mol Pathol*, 54(6):386–392, 2001.

J. H. Conway, R. H. Hardin, and N. J. A. Sloane. Packing lines, planes, etc.: Packings in grassmannian space. *Experimental Mathematics*, 5:139–159, August 1996.

P. A. Cook, Y. Bai, S. Nedjati-Gilani, K. K. Seunarine, M. G. Hall, G. J. Parker, and D. C. Alexander. Camino: Open-source diffusion-mri reconstruction and processing. In *14th ISMRM*, Seattle, USA, 2006.

P.A. Cook, M. Symms, P.A. Boulby, and D.C. Alexander. Optimal acquisition orders of diffusion-weighted mri measurements. *Journal of magnetic resonance imaging*, 25(5):1051–8, 2007.

P Craven and G Wahba. Smoothing noisy data with spline functions. *Numerische Mathematik*, 31(4):377–403, 1985.

Alessandro Daducci, Jason McEwen, Dimitri Van De Ville, Jean-Philippe Thiran, and Yves Wiaux. Harmonic analysis of spherical sampling in diffusion MRI. In *International Soc. for Magn. Reson. Med. (ISMRM) conference*, page 3929, 2011.

P. Delsarte, J. Goethals, and J. Seidel. Spherical codes and designs. *Geometriae Dedicata*, 6:363–388, 1977. 10.1007/BF03187604.

R. Deriche, J. Calder, and M. Descoteaux. Optimal real-time q-ball imaging using regularized Kalman filtering with incremental orientation sets. *Med. Image Anal.*, 13(4):564–579, August 2009.

M. Descoteaux, E. Angelino, S. Fitzgibbons, and R. Deriche. Regularized, fast, and robust analytical q-ball imaging. *Magn. Res. Med.*, 58(3):497–510, 2007a.

M. Descôteaux, R. Deriche, D. LeBihan, J.-F. Mangin, and C. Poupon. Diffusion propagator imaging: Using laplace's equation and multiple shell acquisitions to reconstruct the diffusion propagator. In *IPMI*, LNCS 5636, page 1–13, 2009.

Maxime Descoteaux, Elaine Angelino, Shaun Fitzgibbons, and Rachid Deriche. Apparent diffusion coefficients from high angular resolution diffusion imaging: Estimation and applications. *Magnetic Resonance in Medicine*, 56:395–410, 2006.

Maxime Descoteaux, Elaine Angelino, Shaun Fitzgibbons, and Rachid Deriche. Regularized, fast, and robust analytical q-ball imaging. *Magnetic Resonance in Medicine*, 58(3):497–510, 2007b.

Maxime Descoteaux, Nicolas Wiest-Daesslé, Sylvain Prima, Christian Barillot, and Rachid Deriche. Impact of rician adapted non-local means filtering on hardi. In Dimitris N. Metaxas, Leon Axel, Gabor Fichtinger, and Gábor Széke, editors, *MICCAI*, volume 5242 of *Lecture Notes in Computer Science*. Springer, September 2008.

Maxime Descoteaux, Cheng Guan Koay, Peter J. Basser, and Rachid Deriche. Analytical q-ball imaging with optimal regularization. In *ISMRM 18th Scientific Meeting and Exhibition*, May 2010.

Maxime Descoteaux, Rachid Deriche, Denis Le Bihan, Jean-Francois Mangin, and Cyril Poupon. Multiple q-shell diffusion propagator imaging. *Medical Image Analysis*, 15:603–621, 2011.

J. R. Driscoll and D. M. J. Healy. Computing fourier transforms and convolutions on the sphere. *Advances in Applied Mathematics*, 15:202–250, 1994.

J. Dubois, C. Poupon, F. Lethimonnier, and D. Le Bihan. Optimized diffusion gradient orientation schemes for corrupted clinical dti data sets. *MAGMA Magnetic Resonance Materials in Physics, Biology and Medicine,*, 19(3):134–143(10), 2005.

A. Einstein. *Investigations on the Theory of the Brownian Movement*. Dover Pubns, 1956.

László Fejes-Tóth. On covering a spherical surface with equal spherical caps. *Matematikai és fizikai lapok*, 50:40–46, 1943.

Pierre Fillard, Xavier Pennec, Vincent Arsigny, and Nicholas Ayache. Clinical DT-MRI estimation, smoothing, and fiber tracking with log-Euclidean metrics. *IEEE Transactions on Medical Imaging*, 26(11):1472–82, November 2007.

Pierre Fillard, Maxime Descoteaux, Alvina Goh, Sylvain Gouttard, Ben Jeurissen, James Malcolm, Alonso Ramirez-Manzanares, Marco Reisert, Ken Sakaie, Fatima Tensaouti, Ting Yo, Jean-François Mangin, and Cyril Poupon. Quantitative analysis of 10 tractography algorithms on a realistic diffusion MR phantom. *Neuroimage*, 56(1):220–234, 2011.

Wei Gao, Hongtu Zhu, and Weili Lin. A unified optimization approach for diffusion tensor imaging technique. *NeuroImage*, 44(3):729–741, 2009.

J. M. Goethals and J. J. Seidel. Cubature formulae, polytopes and spherical designs. In H.S.M. Coxeter, C. Davis, B. Grünbaum, and F.A. Sherk, editors, *The Geometric vein: the Coxeter festschrift*, page 203–218. Springer-Verlag, New York, 1981.

Alvina Goh, Christophe Lenglet, Paul M. Thompson, and René Vidal. A nonparametric riemannian framework for processing high angular resolution diffusion images and its applications to odf-based morphometry. *NeuroImage*, 56(3):1181 – 1201, 2011.

C. Golgi, M. Bentivoglio, and L. Swanson. On the fine structure of the pes Hippocampi major (with plates XIII-XXIII). 1886. *Brain research bulletin*, 54(5): 461–483, March 2001. ISSN 0361-9230.

Gene H. Golub and Charles F. Van Loan. *Matrix computations*. The John Hopkins University Press, Baltimore, Maryland, 1983.

Henry. Gray. *Gray's Anatomy of the Human Body*. LEA and FEBIGER, 1918, 1918.

P. C. Hansen. The l-curve and its use in the numerical treatment of inverse problems. In *in Computational Inverse Problems in Electrocardiology, ed. P. Johnston, Advances in Computational Bioengineering*, pages 119–142. WIT Press, 2000.

R. H. Hardin and N. J. A. Sloane. Mclaren's improved snub cube and other new spherical designs in three dimensions. *Discrete and Computational Geometry*, 15: 429–441, 1996.

C.P. Hess, P. Mukherjee, E.T. Han, D. Xu, and D.B. Vigneron. Q-ball reconstruction of multimodal fiber orientations using the spherical harmonic basis. *Magnetic Resonance in Medicine*, 56:104–117, 2006.

Martin D. Hürlimann, Lawrence M. Schwartz, and Pabitra N. Sen. Probability of return to the origin at short times: A probe of microstructure in porous media. *Phys. Rev. B*, 51:14936–14940, 1995.

K. M. Jansons and D. C. Alexander. Persistent angular structure: new insights fom diffusion magnetic resonance imaging data. *Inverse Problems*, 19:1031–1046, 2003.

Bing Jian, Baba C. Vemuri, Evren Özarslan, Paul R. Carney, and Thomas H. Mareci. A novel tensor distribution model for the diffusion-weighted mr signal. *NeuroImage*, 37(1):164 – 176, 2007.

Fangxiang Jiao, Yaniv Gur, Chris R. Johnson, and Sarang Joshi. Detection of crossing white matter fibers with high-order tensors and rank-k decompositions. In *IPMI*, IPMI'11, page 538–549, Berlin, Heidelberg, 2011. Springer-Verlag.

Heidi Johansen-Berg and Timothy E.J. Behrens, editors. *Diffusion MRI: From quantitative measurement to in-vivo neuroanatomy*. Academic Press, 2009.

D. K. Jones, M. A. Horsfield, and A. Simmons. Optimal strategies for measuring diffusion in anisotropic systems by magnetic resonance imaging. *Magn. Reson. Med.*, 42(3):515–525, September 1999a.

Derek K. Jones, editor. *Diffusion MRI: Theory, Methods, and Applications*. Oxford University Press, 2010a.

Derek K Jones, editor. *Diffusion MRI: Theory, Methods, and Applications*. Oxford University Press, 2010b.

D.K. Jones, M.A. Horsfield, and A. Simmons. Optimal strategies for measuring diffusion in anisotropic systems by magnetic resonance imaging. *Magnetic Resonance in Medicine*, 42(39):515 – 525, August 1999b.

E. Jones, T. Oliphant, P. Peterson, et al. SciPy: Open source scientific tools for Python, 2001. URL `http://www.scipy.org/`.

Steven M. Kay. *Fundamentals of statistical signal processing: estimation theory*. Prentice-Hall, Inc., Upper Saddle River, NJ, USA, 1993.

M.H. Khachaturian, J.J. Wisco, and D.S. Tuch. Boosting the sampling efficiency of q-ball imaging using multiple wavevector fusion. *Magnetic Resonance in Medicine*, 57(2):289–296, 2007.

C. G. Koay, E. Özarslan, and C. Pierpaoli. Probabilistic identification and estimation of noise (piesno): A self-consistent approach and its applications in mri. *Journal of Magnetic Resonance*, 199:94–103, 2009a.

Cheng G. Koay, Evren Özarslan, and Peter J. Basser. A signal transformational framework for breaking the noise floor and its applications in mri. *Journal of Magnetic Resonance*, 197(2):108–119, April 2009b.

Cheng Guan Koay. A simple scheme for generating nearly uniform distribution of antipodally symmetric points on the unit sphere. *J. Comput. Science*, 2(4): 377–381, 2011.

B. Landman, P.-L. Bazin, and J. Prince. Diffusion tensor estimation by maximizing rician likelihood. In *Computer Vision, 2007. ICCV 2007. IEEE 11th International Conference on*, pages 1 –8, 2007.

P.C. Lauterbur. Image formation by induced local interactions: examples employing nuclear magnetic resonance. *Nature*, 242:190–191, 1973.

Denis Le Bihan and E. Breton. Imagerie de diffusion it in vivo par résonnance magnétique nucléaire. *CR Académie des Sciences*, (301):1109–1112, 1985.

A Leemans and D K Jones. The b-matrix must be rotated when correcting for subject motion in dti data. *Magn Reson Med*, 61(6):1336–49, 2009.

C. Lenglet. *Geometric and Variational Methods for Diffusion Tensor MRI Processing*. PhD thesis, University of Nice-Sophia Antipolis, 2006.

Jason D. McEwen and Yves Wiaux. A novel sampling theorem on the sphere. *IEEE Transactions on Signal Processing*, 59(12):5876–5887, 2011.

K.D. Merboldt, W. Hanicke, and J. Frahm. Self-diffusion nmr imaging using stimulated echoes. *J. Magn. Reson.*, 64:479–486, 1985.

Sylvain Merlet, Emmanuel Caruyer, and Rachid Deriche. Impact of radial and angular sampling on multiple shells acquisition in diffusion mri. In *MICCAI*, volume 6891, pages 113–121. Springer, 2011. URL `http://hal.archives-ouvertes.fr/hal-00614387/en/`.

Sylvain Merlet, Emmanuel Caruyer, Aurobrata Ghosh, and Rachid Deriche. Parametric dictionary learning in diffusion mri. In *HARDI Contest, ISBI - Internation Symposium on Biomedical Imaging*, Barcelona, Spain, May 2012. Alessandro Daducci and Jean-Philippe Thiran and Yves Wiaux.

P.P. Mitra, L.L. Latour, R.L. Kleinberg, and C.H. Sotak. Pulsed-field-gradient nmr measurements of restricted diffusion and the return-to-the-origin probability. *Journal of Magnetic Resonance, Series A*, 114(1):47 – 58, 1995.

S. Mori, B.J. Crain, V.P. Chacko, and P.C.M. Van Zijl. Three-dimensional tracking of axonal projections in the brain by Magnetic Resonance Imaging. *Annals of Neurology*, 45(2):265–269, February 1999.

Lauren J. O'Donnell and Carl-Fredrik Westin. Automatic tractography segmentation using a high-dimensional white matter atlas. *IEEE Transactions on Medical Imaging*, 26(11):1562–1575, 2007.

E. Ozarslan, C.G. Koay, and P.J. Basser. Simple harmonic oscillator based estimation and reconstruction for one-dimensional q-space mr. In *Proc. Intl. Soc. Mag. Reson. Med.*, volume 16, page 35, 2008.

E. Ozarslan, C. G. Koay, T. M. Shepherd, and P. J. Blackband, S. J. and-Basser. Simple harmonic oscillator based reconstruction and estimation for three-dimensional q-space mri. In *17th ISMRM*, Hawai, USA, April 2009.

Evren Özarslan and Thomas H. Mareci. Generalized diffusion tensor imaging and analytical relationships between diffusion tensor imaging and high angular resolution imaging. *Magnetic Resonance in Medicine*, 50:955–965, 2003.

Evren Özarslan, Noam Shemesh, Chen Guan Koay, Yoram Cohen, and Peter J Basser. Nmr characterization of general compartment size distributions. *New Journal of Physics*, 13, 2011.

N G Papadakis, D Xing, C L Huang, L D Hall, and T A Carpenter. A comparative study of acquisition schemes for diffusion tensor imaging using mri. *Journal of Magnetic Resonance*, 137(1):67–82, 1999.

N G Papadakis, C D Murrills, L D Hall, C L Huang, and T Adrian Carpenter. Minimal gradient encoding for robust estimation of diffusion anisotropy. *Magn Reson Imaging*, 18(6):671–9, 2000.

Huiling Peng and Konstantinos Arfanakis. Diffusion tensor encoding schemes optimized for white matter fibers with selected orientations. *Magnetic Resonance Imaging*, 25(2):147–53, 2007.

A Pfefferbaum, EV Sullivan, M Hedehus, KO Lim, E Adalsteinsson, and M Moseley. Age-related decline in brain white matter anisotropy measured with spatially corrected echo-planar diffusion tensor imaging. *Magn Reson Med*, 44(2):259–68, 2000.

C. Pierpaoli and P.J. Basser. Toward a quantitative assessment of diffusion anisotropy. *Magn. Res. Med.*, 36:893–906, 1999.

J Piven, J Bailey, BJ Ranson, and S Arndt. An mri study of the corpus callosum in autism. *Am J Psychiatry*, 154:1051–1056, 1997.

C. Poupon, B. Rieul, I. Kezele, M. Perrin, F. Poupon, and J-F. Mangin. New diffusion phantoms dedicated to the study and validation of hardi models. *Magnetic Resonance in Medicine*, 60:1276–1283, 2008a.

C. Poupon, A. Roche, J. Dubois, J.-F. Mangin, and F. Poupon. Real-time MR diffusion tensor and q-ball imaging using Kalman filtering. *Med. Image Anal.*, 12(5):527–534, 2008b. Special issue on the 10th International Conference on MICCAI 2007.

Cyril Poupon. *Détection des faisceaux de fibres de la substance blanche pour l'étude de la connectivité anatomique cérébrale.* PhD thesis, Ecole Nationale Supérieure des Télécommunications, December 1999.

E.M. Purcell, H.C. Torrey, and R.V. Pound. Resonance absorption by nuclear magnetic moments in a solid. *Physical Review*, 69:37–38, 1946.

S. Ramon y Cajal. *A new concept of the histology of the central nervous system*, pages 7—-29. Hafner Press, 1892.

G. K. Rohde, A. S. Barnett, P. J. Basser, S. Marenco, and C. Pierpaoli. Comprehensive approach for correction of motion and distortion in diffusion-weighted MRI. *Magn. Reson. Med.*, 51(1):103–114, January 2004.

G. K. Rohde, A. S. Barnett, P. J. Basser, and C. Pierpaoli. Estimating intensity variance due to noise in registered images: applications to diffusion tensor MRI. *NeuroImage*, 26(3):673–684, July 2005.

Robert Sadourny, Akio Arakawa, and Yale Mintz. Integration of the nondivergent barotropic vorticity equation with an icosahedral-hexagonal grid for the sphere. *Monthly Weather Review*, 96(6):351, 1968.

R. Salvador, A. Pena, D.K.. Menon, T..A. Carpenter, J.D.. Pickard, and E.T.. Bullmore. Formal characterization and extension of the linearized diffusion tensor model. *Human Brain Mapping*, 24(2):144–155, February 2005.

Thomas Schultz and Hans-Peter Seidel. Estimating crossing fibers: A tensor decomposition approach. *IEEE Transactions on Visualization and Computer Graphics*, 14(6):1635–1642, November 2008.

Wladimir Shukowsky. A quadrature formula over the sphere with application to high resolution spherical harmonic analysis. *Journal of geodesy*, 60(1):1–14, 1986.

J. Sijbers, A. J. den Dekker, J. Van Audekerke, M. Verhoye, and D. Van Dyck. Estimation of the noise in magnitude mr images. *Magnetic Resonance Imaging*, 16(1):87–90, 1998.

Jan Sijbers. *Signal and Noise Estimation from Magnetic Resonance Images*. PhD thesis, Universiteit Antwerpen, 1998.

S. Skare, M. Hedehus, M. E. Moseley, and T. Q. Li. Condition number as a measure of noise performance of diffusion tensor data acquisition schemes with MRI. *J Magn Reson*, 147(2):340–352, December 2000.

George W. Snedecor and William G. Cochran. *Statistical Methods*. Iowa State University Press, 1989.

John M. Snyder and Alan H. Barr. Ray tracing complex models containing surface tessellations. *SIGGRAPH Comput. Graph.*, 21(4):119–128, August 1987.

O. Soderman and B. Jonsson. Restricted Diffusion in Cylindrical Geometry. *Journal of Magnetic Resonance, Series A*, 117(1):94–97, nov 1995.

E.O. Stejskal and J.E. Tanner. Spin diffusion measurements: spin echoes in the presence of a time-dependent field gradient. *Journal of Chemical Physics*, 42: 288–292, 1965.

P.M.L. Tammes. *On the origin of number and arrangement of the places of exit on the surface of pollen-grains*. J. H. de Bussy, 1930.

D.G. Taylor and M.C. Bushell. The spatial mapping of translational diffusion coefficients by the nmr imaging technique. *Phys. Med. Biol.*, 30:345–349, 1985.

J. J. Thomson. On the structure of the atom: an investigation of the stability and periods of oscillation of a number of corpuscles arranged at equal intervals around the circumference of a circle; with application of the results to the theory of atomic structure. *Philosophical Magazine*, 7(39):237–265, March 1904.

J.-D. Tournier, F. Calamante, D.G. Gadian, and A. Connelly. Direct estimation of the fiber orientation density function from diffusion-weighted mri data using spherical deconvolution. *NeuroImage*, 23:1176–1185, 2004.

A. Tristán-Vega, C.-F. Westin, and S. Aja-Fernández. Estimation of fiber orientation probability density functions in high angular resolution diffusion imaging. *NeuroImage*, 47(2):638–650, 2009.

D. Tuch. Q-ball imaging. *Magnetic Resonance in Medicine*, 52(6):1358–1372, 2004a.

D. S. Tuch. Q-ball imaging. *Magn. Reson. Med.*, 52(6):1358–1372, 2004b.

David S. Tuch, Timothy G. Reese, M. R. Wiegell, N. G. Makris, John W. Belliveau, and Van Jay Wedeen. High angular resolution diffusion imaging reveals intravoxel white matter fiber heterogeneity. *Magn. Res. Med.*, 48(4):577–582, 2002.

Lihui Wang, Yuemin Zhu, Hongying Li, Wanyu Liu, and I.E. Magnin. Multiscale modeling and simulation of the cardiac fiber architecture for dmri. *Biomedical Engineering, IEEE Transactions on*, 59(1):16 –19, 2012.

Demian Wassermann. *Automated In Vivo Dissection of White Matter Structures from Diffusion Magnetic Resonance Imaging*. PhD thesis, Nice Sophia-Antipolis University, April 2010.

Demian Wassermann, Luke Bloy, Efstathios Kanterakis, Ragini Verma, and Rachid Deriche. Unsupervised white matter fiber clustering and tract probability map generation: Applications of a gaussian process framework for white matter fibers. *Neuroimage*, 51(1):228–241, May 2010.

V.J. Wedeen, P. Hagmann, W. Tseng, T.G. Reese, and R.M. Weisskoff. Mapping complex tissue architecture with diffusion spectrum magnetic resonance imaging. *Magnetic Resonance in Medicine*, 54(6):1377–1386, 2005.

Wally Welker, John Irwin Johnson, and Adrianne Noe. Comparative mammalian brain collection. `http://www.brainmuseum.org/`. Michigan State University.

C F Westin, S E Maier, H Mamata, A Nabavi, F A Jolesz, and R Kikinis. Processing and visualization for diffusion tensor MRI. *Medical Image Analysis*, 6:93–108, 2002.

A. Willsky and H. Jones. A generalized likelihood ratio approach to the detection and estimation of jumps in linear systems. *Automatic Control, IEEE Transactions on*, 21(1):108 – 112, feb 1976.

Y.C. Wu and A.L. Alexander. Hybrid diffusion imaging. *NeuroImage*, 36(3): 617–629, 2007.

Nathan Yanasak, Jerry D. Allison, Qun Zhao, Tom C. Hu, and Krishnan Dhandapani. Non-uniform gradient prescription for precise angular measurements using dti. In *Medical Image Computing and Computer-Assisted Intervention*, MICCAI '08, page 866–873, Berlin, Heidelberg, 2008. Springer-Verlag.

Wenxing Ye, Sharon Portnoy, Alireza Entezari, Stephen J. Blackband, and Baba C. Vemuri. Efficient interlaced multi-shell sampling scheme for reconstruction of diffusion propagators. *IEEE Transactions on Medical Imaging*, 2012. In press.

Chun Hung Yeh. *Diffusion Microscopist Simulator - The Development and Application of a Monte Carlo Simulation System for Diffusion MRI*. PhD thesis, Université Paris Sud (Paris XI) / National Yang Ming University, 2011.

Yu-Li You and Mostafa Kaveh. Fourth-order partial differential equations for noise removal. *IEEE Transactions on Image Processing*, 9(10):1723–1730, 2000.